Phase-Matched Emission from Rydberg Atoms Confined in a State-Insensitive Trap: Long-Lived Coherence, Hyperfine Level Measurements, and Hanbury Brown-Twiss Interference

by

Jacob Andrew Lampen

A dissertation submitted in partial fulfillment
of the requirements for the degree of
Doctor of Philosophy
(Physics)
in the University of Michigan
2020

Doctoral Committee:
Professor Alex Kuzmich, Chair
Professor Emeritus Paul Berman
Professor Steven Cundiff
Professor Vanessa Sih
Assistant Professor Liuyan Zhao

Jacob Lampen

jlampen@umich.edu

ORCID iD: 0000-0002-4951-5326

To my wife and family

Acknowledgments

First, I would like to thank my advisor, Professor Alex Kuzmich. He always strives to get the best work possible out of his students. As a result, I have gained in my academic knowledge of physics and my practical ability to work efficiently in a laboratory. Alex is also extremely focused on and committed to research. If I wasn't sure what the next steps I should take for the experiment were, he was always there to consult and had a great intuition about what was needed to solve a problem. His deep knowledge and sharp intellect were useful when confronting any technical problems in the lab.

I would like to thank Huy Nguyen and Alisher Duspayev for their advice on and help in the laboratory. I enjoyed working with them as a team and I look forward to seeing the research they continue to pursue in the future. Also, I thank them for advising me on my future career choices and for revising my thesis. They have been wonderful friends whom I value very much.

Thank you to Hikaru Tamura, Yin Li, Jacob Curtis, and Andrea Londono. It has been a pleasure to work with all of them. I wish them success in their future endeavors.

I am grateful to the past members of the lab who taught me how to work in an AMO lab: Corey Campbell, Alexandr Arakelyan, Lin Li, and Kan Ding. Without all of them, I would not have learned the basics of research. I am indebted to them for taking time out of their schedule to teach me.

Thank you to Professor Paul Berman for his theoretical work, which helped me understand the fundamentals of my experiments. I would also like to thank the rest of my committee: Professor Steven Cundiff, Professor Vanessa Sih, and Professor Liuyan Zhao.

And to my family: for being there for me when I needed them and for raising me to believe in myself. I thank my wife, Kathyrn, who supported me through my graduate school career. She helped me keep things in perspective so I could put my best foot forward. I could not have made it through graduate school without her. To our six-month-old son, Sam, you bring me joy and a reason to keep trying my best in anything and everything that I do.

Table of Contents

List of Figures

Abstract

Rydberg ensembles have many diverse and important applications for quantum information and quantum optics. For example, Rydberg ensembles can generate non-classical states of light which would be useful in a quantum network, and they could be used as qubits in a future quantum computer. For this reason, this thesis will present investigations of light-matter interactions in Rydberg ensembles.

Non-classical states of light, such as single-photon states, are important for many quantum communication protocols. We have performed an experiment that demonstrates the generation of single-photon states from a Rydberg ensemble. We then studied the second-order correlations between this single-photon state of light and an incident coherent field. Under these conditions, we observed Hanbury Brown-Twiss interference between the emission from a driven super-atom and a coherent field in the absence of stimulated emission.

For a universal quantum computing architecture, coherence times must be much longer than gate operations. We observe ground-Rydberg coherence times in excess of $20\ \mu$s by using a "magic-wavelength" optical lattice to confine the atoms. Using this coherence time, we measured the differential nuclear-spin-dependent light shifts for principal quantum numbers, n, between $n = 30$ and $n = 65$, which is relevant for future high-fidelity Rydberg qubits in optical potentials. Also, we measured the hyperfine constant for atomic Rb to be $\bar{A}_{ns} = 35.71 \pm 0.18$ GHz.

Chapter 1

Introduction

In 1901, Max Planck discovered that the quantization of the electromagnetic radiation emitted from a black body solved the so-called "ultraviolet catastrophe" [1]. This catastrophe was a problem in classical physics where the prevailing theory, the Rayleigh-Jeans law, predicted a divergence in the amount of electromagnetic radiation from a black body at shorter wavelengths. A new field of physics, quantum optics, began in the process of resolving this problem. Since that time, quantum optics has grown to a field of physics that affects everyday life because of the development of technologies such as solar cells, lasers, and fiber optics. Within the scientific community, advances in protocols for the generation of entangled and squeezed states of light have paved the way for quantum-enhanced metrology, atomic clocks [2], and precision measurements such as measuring vibrations in spacetime [3]. Quantum optics has enabled researchers to study the fundamental nature of light-matter interaction: long-range entanglement [4], optical tweezers [5], and cooling atoms to a Bose-Einstein condensate [6]. Moreover, quantum optics has combined with computer science to form the field of quantum information.

In the keynote talk at the First Conference on Quantum Computation in 1981, Richard Feynman spoke on the differences between a classical computer and a hypothetical quantum computer when simulating a quantum system. He concluded that classical computation was

impractical for simulations of quantum mechanics because the necessary computational power scales exponentially with the number of particles and degrees of freedom in the simulation [7]. A quantum computer could hypothetically simulate quantum mechanical systems without exponential scaling in the size of the computer. Since that conference, there have been many advances in the field of quantum information, including the first quantum logic gates[8], multi-qubit quantum processors [9], primitive calculations [10], and the first claims of quantum supremacy [11]. Today there is such excitement about quantum information that, within the private sector, several companies are developing quantum computers for future commercial purposes. These advancements have been implemented in a variety of architectures, such as superconducting circuits, trapped ions, quantum dots, and neutral atoms. Quantum information and quantum optics based on neutral atoms has seen great advancement in recent years and will be the focus of this thesis.

1.1 Overview

Neutral atoms excited to states with a high principal quantum number (n), so-called Rydberg states, can have state-dependent interactions that are necessary for quantum logic, for example, two-bit gates. Furthermore, the interaction can be tuned by the proper choice of principal quantum number n. For example, at $n = 100$ it has been shown that the interaction between two atoms is twelve orders of magnitude larger than for ground-state atoms [12]. Rydberg ensembles exhibit interesting many-body physics phenomena, such as Rydberg blockade [13]. In contrast to single atoms, Rydberg ensembles in the blockade regime utilize many-body effects to achieve strong atom-photon coupling [14]. Also, the efficient generation of single-photons can be realized in ensembles of atoms [13], which is important for many quantum communication protocols.

This thesis will present investigations of light-matter interactions in Rydberg ensembles and their applications for quantum information and quantum optics. In these investigations,

I was involved in experimental design, fabrication, and data acquisition. Additionally, I aided in the analysis and modeling of each experiment. These studies can be separated into two general topics: (1) interference effects between a coherent state and non-classical states of light from a Rydberg ensemble, and (2) investigations on long-lived coherence between ground and Rydberg levels.

(1) Non-classical states of light, such as single-photon states, play an important role in many quantum communication protocols, such as entanglement swapping [15, 16] and quantum key distribution [17]. We have performed an experiment that demonstrates the ability to create single-photon states from a neutral atom ensemble, and we studied the second-order correlations with an incident coherent field. With these correlations, we show the presence of Hanbury Brown-Twiss (HBT) interference between a coherent field and emission from a driven super-atom in the absence of stimulated emission. This is in contrast to previous experiments that have inferred a connection between the two phenomena.

(2) The third of five criteria that DiVincenzo identified for a universal quantum computing architecture is that coherence times must be much longer than gate operations [18]. In the past, coherence time was severely limited in experiments with Rydberg ensembles due to motional dephasing. By using a "magic-wavelength" optical lattice to confine the atoms, we demonstrate ground-Rydberg coherence times in excess of $20\ \mu s$, which is an order of magnitude improvement over previous experiments performed with unconfined ensembles. Using this improvement, we were able to measure the differential nuclear-spin-dependent light shifts for principal quantum numbers n between $n = 30$ and $n = 65$.

This thesis is comprised of six chapters:

- Chapter 1. This chapter provides the background necessary for the rest of the thesis, including neutral alkali atoms, Rydberg states, state-insensitive trapping, and second-order correlations of photons. The potential benefits and detriments of using neutral Rydberg atoms for quantum information are also discussed throughout the chapter.

- Chapter 2. This chapter goes over the experimental setups that were used in the following three chapters. In particular, I examine the magneto-optical trap setup, several of the laser systems that were used, the normalization of the coincidences for Hanbury Brown-Twiss interference, the optical lattice geometry, and the procedure to measure the magic detuning.

- Chapter 3. Hanbury Brown and Twiss (HBT) interference and stimulated emission, two fundamental processes in atomic physics, have been studied in a wide range of applications in science and technology. We study interference effects that occur when a weak probe is sent through a gas of two-level atoms that are prepared in a singly-excited collective (Dicke or “superatom") state and for atoms prepared in a factorized state. We measure the time-integrated second-order correlation function $g^{(2)}$ of the output field as a function of the delay between input probe field and radiation emitted by the atoms τ and find that, for the Dicke state, $g^{(2)}$ is twice as large for $\tau = 0$ as it is for $\gamma_e \tau \gg 1$ (γ_e is an excited state decay rate), while for the product state, this ratio is equal to 3/2. The results agree with those of a theoretical model in which any effects related to stimulated emission are totally neglected - the coincidence counts measured in our experiment arise from Hanbury Brown and Twiss interference between the input field and the field radiated by the atoms.

- Chapter 4. This chapter discusses our findings on enhanced ground-Rydberg coherence. By confining atoms in a state-insensitive optical lattice, the lifetime of the ground-Rydberg coherence is increased to ≥ 20 μs, an order of magnitude improvement over previous experiments using freely diffusing atoms. Using these enhanced lifetimes, we measure the so-called "magic" lattice wavelengths for Rb and use them to extract the $\left|6p_{3/2}\right\rangle \Leftrightarrow \left|ns_{1/2}\right\rangle$ reduced electric dipole matrix elements. Good agreement is found with values obtained using an effective one-electron potential for principal quantum numbers n between $n = 30$ and $n = 70$. We develop a theoretical model

based on quantized motion to map out the ground-Rydberg coherence as a function of time that is in good agreement with the experimental results. The availability of long coherence times presents new opportunities for high-resolution spectroscopy and quantum information science.

- Chapter 5. This chapter presents a detailed analysis of the nuclear-spin manifolds associated with the ns Rydberg levels of ^{87}Rb atoms that interact with both magnetic and optical lattice fields. Eigenvalues and eigenkets for the Rydberg manifold are obtained and used to study the dynamics of phase-matched emission following illumination of an ensemble of cold atoms with excitation and readout laser pulses. By comparing the measured emission signal to predictions of a model that accounts for the quantized motion of atoms in a one-dimensional optical lattice potential, we are able to extract the Rydberg hyperfine and light shift contributions to the observed modulation frequencies. In this way, the hyperfine splitting of Rydberg ns levels is measured for n in the range of 30 to 65. Our results should be relevant for realizations of high-fidelity Rydberg qubits confined in optical potentials.

- Chapter 6. I state the conclusions from the previous chapters and look at the future of the field.

1.2 Neutral alkali atoms

Alkali atoms (lithium, sodium, potassium, rubidium, cesium, and francium) have a single valence electron. Such atoms generally possess a simple energy level structure. For rubidium and cesium in particular, the atomic energy levels have a narrow natural linewidth in comparison to the energy separation between the different states. This is significant because when the atoms are driven with a narrow linewidth excitation field, the energy level structure can be approximated as a two-level system as is necessary for a qubit. Rubidium and cesium are

commonly used in neutral atom quantum computation experiments because diode lasers that produce light for the transitions of these atoms can be easily produced. There are also many established techniques to cool and trap these atoms in a vacuum system. A cold cloud of atoms isolated from collisions with background gases has a longer trap lifetime than atoms not in a vacuum. These longer lifetimes can be helpful because there is more time in between experimental loadings for measurements. For all of these reasons, ensembles of ^{87}Rb atoms are used for all of the experiments in this thesis.

Neutral alkali atoms have been used to demonstrate several important quantum information protocols including generation of single-photons [13], long-lived quantum memories [19], photon conversion to a telecommunication wavelength (to use in the existing telecommunications infrastructure) [20], and large defect-free arrays of neutral atoms in an optical lattice (for scaling the number of qubits) [21, 22]. These demonstrations show the potential of neutral atoms as an architecture for a scalable quantum computer or network. However, there are still open questions in the field as to whether neutral atom quantum gates with high fidelity will be achieved as has been done for superconducting circuits and trapped ions. Currently the highest-fidelity two-qubit gates for neutral atoms is $f \approx 0.9$ in a two-dimensional array [23] and $f \geq 0.974$ in a one-dimensional array [24]. This will have to be improved for a future quantum computer. If a calculation needs 100 gate operations and the fidelity is 0.97, the probability of having a correct calculation is $\approx 5\%$. Another potential problem for using neutral atoms in quantum information is that they have much shorter trap lifetimes than trapped ions, therefore, periodic reloading of the atomic sample is required. This is in contrast to ions, which can be trapped and used for long periods of time.

1.3 Rydberg atoms

1.3.1 Basic properties

State-dependent interactions are necessary for two-qubit quantum gates [12]. Creating these gates is an important step towards quantum computation. These state-dependent interactions can be achieved in neutral atoms by changing the principal quantum number. Interactions between two neutral atoms are generally weak if they are in the ground state. However, when the atoms are excited to high principal quantum numbers, the interaction strength grows by several orders of magnitude. These highly excited states, referred to as Rydberg states, are similar to the states in a hydrogen atom with energy level scaling as $\sim n^{-2}$ and the electron orbital radius scaling as $\sim n^2$.

Rydberg level property	Scaling with principal quantum number
Radius	n^2
Dipole-dipole interaction	n^4
van der Waals interaction	n^{11}
Nuclear sub-level splitting	n^{-3}
Magic wavelength detuning	n^{-3}

Table 1.1: Rydberg level properties and the theoretical scaling principals with the principal quantum number.

For Rydberg atoms, the electronic wavefunctions are distributed so far from the nucleus that the effective electron dipole moment of the atom is very large in comparison to a ground-state atom. If two Rydberg atoms are in close proximity, they will interact either through the dipole-dipole interaction, which scales as $\sim n^4$, or through the van der Waals interaction, which scales as $\sim n^{11}$, as can be seen in Table 1.1. The force that is dominant depends on the distance between the two atoms. The van der Waals force is dominant at long distances, and the dipole-dipole force is dominant at short distances. These large scaling factors allow

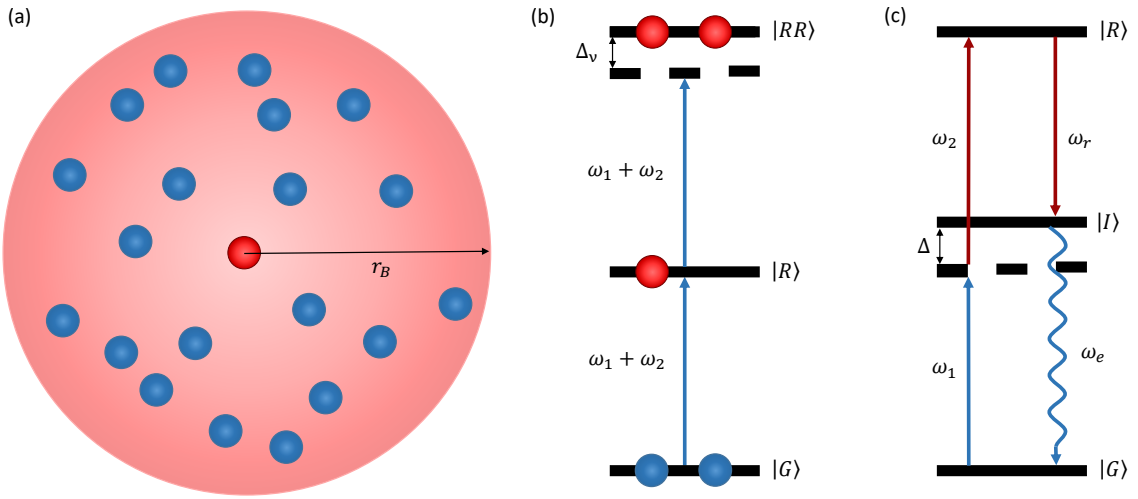

Figure 1.1: (a) An ensemble of atoms with a single Rydberg excitation. The Rydberg blockade radius, r_b, for the Rydberg atom grows with the principal quantum number such that at large enough principal quantum numbers the Rydberg blockade can be on the order of the size of the ensemble. (b) The interaction shifts the doubly excited state, $|RR\rangle$, by Δ_ν, which is out of resonance with the two-photon excitation. (c) Diagram of a two-photon excitation scheme with frequencies ω_1 and ω_2 detuned by Δ from the intermediate state $|I\rangle$. A retrieval pulse, ω_r, results in an emitted photon ω_e.

atoms separated by ~ 10 microns to interact with each other, shifting the dipole transitions on the order of ~ 10 MHz at a principal quantum number of $n \approx 100$ [12]. In the experiments presented in this thesis, the ^{87}Rb atoms are excited to principal quantum numbers between $n = 30$ and $n = 87$.

1.3.2 Rydberg blockade

When an atom is excited to a sufficiently high principal quantum number, the dipole-dipole/van der Waals interaction between the excited atom and any nearby atoms will shift the Rydberg levels of the nearby atoms out of resonance with a narrow linewidth excitation field. It can be derived that the probability of exciting a second atom to the same Rydberg

state is [12]:

$$P = \frac{N-1}{N}\frac{\Omega_N^2}{\Delta_\nu}, \tag{1.1}$$

where N is the number of atoms, Ω_N is the collective Rabi frequency which is $\sqrt{N}$ times a single atom's rabi frequency Ω, and Δ_ν is the energy shift due to the interactions with the Rydberg atom. At a sufficiently high principal quantum number, where Δ_ν is large, and at a low collective Rabi frequency there will be one Rydberg atom in the ensemble. This means that the one excitation can "block" every other atom within an ensemble from being excited as depicted in Fig. 1.1 (a) and (b). This is the phenomenon known as Rydberg blockade, and the radius, within which no further atoms can be excited, is known as the blockade radius [25, 26, 27].

If the ensemble is smaller than the blockade radius, the entire cloud of atoms can only have one excitation in it, creating a collective Dicke state, which is described by:

$$|R\rangle = \frac{1}{\sqrt{N}}\sum_{i=1}^{N}|g_1\rangle...|r_i\rangle...|g_N\rangle, \tag{1.2}$$

where N is the number of atoms, $|g\rangle$ is the ground state for an atom, and $|r_i\rangle$ is the Rydberg state for the ith atom.

This single collective excitation can be useful for single-photon generation. This is shown in Figure 1.1 (c), for the case when the ensemble is excited to a collective Rydberg state via a two-photon transition (ω_1, ω_2). Once the state is excited, a photon can be generated by using a retrieval pulse (ω_r) that drives the Rydberg atom down to an intermediate state $|I\rangle$. The resulting photon emission, from the ensemble, will have a frequency (ω_e) that is the difference between the sum of the two excitation photons and the retrieval photon ($\omega_e = \omega_1 + \omega_2 - \omega_r$), due to conservation of energy. If the ensemble is optically thick, the emitted photon will have a defined spatial mode resulting from the two excitation fields and the retrieval field, such that $\vec{k}_e = \vec{k}_1 + \vec{k}_2 - \vec{k}_r$. This is because the field emission from each of the atoms is phase-matched [28]. This defined emission mode allows for a more efficient collection of

single-photons.

There is also an enhancement in coupling strength between a collective Dicke state and an optical field. The collective Rabi frequency of the effective two-state system has an enhancement $\propto \sqrt{N}$ where N is the number of atoms [14]. So, the more atoms you have, the faster you can drive the collective Rabi oscillation between the ground and Rydberg state. This is important because the ground and Rydberg states form a basis for a qubit in Rydberg ensembles.

1.3.3 Ground-Rydberg coherence

The third of five criteria that DiVincenzo identified for a universal quantum computing architecture is that coherence times must be much longer than gate operations [18]. If the coherence time is less than the duration of a qubit gate operation, the fidelity will be decreased because of the information that is lost from the decoherence. One possible source of a decrease in coherence time in Rydberg ensembles is dephasing. Dephasing is caused by a phase shift of individual atoms within the ensemble relative to other atoms. This leads to destructive interference between the emission fields from the atoms. An example of dephasing, for the case of the two-photon excitation scheme discussed earlier, is motional dephasing. The two-photon excitation will result in a spin-wave where the state can be expressed as:

$$|R\rangle = \frac{1}{\sqrt{N}} \sum_i e^{i\vec{k_s}\cdot\vec{r_i}} |g\rangle ... |r_i\rangle ... |g\rangle, \tag{1.3}$$

where N is the number of atoms, $\vec{k_s}$ is the spin-wave vector ($\vec{k_s} = \vec{k_1} + \vec{k_2}$), and $\vec{r_i}$ is the position of the atoms. If the atoms in the ensemble have a non-zero temperature, they will move in the ensemble and acquire relative phase differences. This motional dephasing limits the coherence lifetime and can be described by the equation:

$$S_{cl} \sim \sum_i \langle e^{i\vec{k_s}\cdot[\vec{v}_{x,i}t - \vec{r}_{o,i}]} \rangle, \tag{1.4}$$

where S_{cl} is the number of photons collected from an ensemble after a retrieval pulse is applied, $\vec{v}_{x,i}$ is the velocity of an atom in the ensemble, t is the time in between the excitation and retrieval pulses, and $\vec{r}_{o,i}$ is the initial position of an atom. Upon averaging over the ensemble it can be shown that the retrieved signal can be modeled as a Gaussian:

$$S_{cl} \sim e^{-\frac{t^2}{\tau^2}}, \tag{1.5}$$

where τ is the dephasing time given by:

$$\tau = \frac{1}{k_s}\sqrt{\frac{m}{k_B T}}, \tag{1.6}$$

where m is the mass of the atom (^{87}Rb), k_B is the Boltzmann constant, and T is the temperature of the ensemble. τ is the limiting factor of coherence time in most unconfined ensembles.

Thus, once the atoms in the ensemble have moved a distance comparable to the spin-wave spatial period ($\lambda_s = \frac{2\pi}{k_s}$), the Rydberg ensemble excitation has completely dephased, and a photon can no longer be retrieved. The dephasing is typically on the order of microseconds for an ensemble at a temperature of $\sim 10\ \mu K$. If the atoms are tightly confined to less than a spin-wave spatial period, then motional dephasing can be reduced, as will be shown in the next section.

1.4 State-insensitive trapping

One way to confine the atomic motion along the direction of the spin-wave is to use a one-dimensional optical lattice along the direction of the excitation beams. The effective two-photon excitation wavelength λ_s will be longer than the distance an atom can move in a lattice site. If we take an excitation scheme that will be used later in this thesis, for example, 420 nm and 1012 nm can be used to excite to Rydberg levels. If the excitation beams are counter-propagating, the resulting spin-wave spatial period is $\lambda_{2ph} = 0.72\ \mu$m. The length

of a single lattice site is $L \approx 0.5$ μm if the wavelength of the lattice field is $\lambda_l \sim 1000$ nm, ($L = \frac{\lambda_l}{2}$). Therefore, the atom cannot move far enough to completely dephase and will oscillate in the lattice. This will be examined in more detail in Chapter 4.

The principle behind an optical lattice is the AC Stark effect: the electric field of an optical lattice shifts the energy levels of the atoms and can be described as $\Delta_{ls} \propto \alpha_g I$, where α_g is the polarizability of the ground state, I is the optical intensity, and Δ_{ls} is the resulting shift for the energy level. In a far detuned lattice, the polarizability of the Rydberg state α_r is generally not equal to the polarizability of the ground level α_g. This leads to spatial variations in the transition frequency between the ground and Rydberg levels. This is significant because, as the atoms move in the trap, the transition frequency for the atom will change depending on their position. Upon retrieval, the fields emitted from the atoms will destructively interfere, decreasing the coherence time. The spatial variations can lead to dephasing of the atoms in < 1 μs. A diagram of the spatial variation can be seen in Fig 1.2(a).

In order to spatially confine the atoms without adding dephasing from the spatial variance of the ground-Rydberg transition, a state-insensitive trap can be utilized. In our state-insensitive trap the frequency of the trapping light is near resonance with the transition between the Rydberg state and an intermediate state as seen in Fig 1.2(b). At a specific detuning (Δ_m) from the transition frequency, the polarizability of the Rydberg state will be matched to that of the ground state ($\alpha_g = \alpha_r$). This detuning is called the "magic" detuning because energy shifts due to the trap are the same for both the ground and Rydberg levels [29, 30]. This allows for spatial confinement of the atoms without adding, to first order, dephasing due to the trapping light. In Chapter 4 some remaining sources of dephasing will be examined.

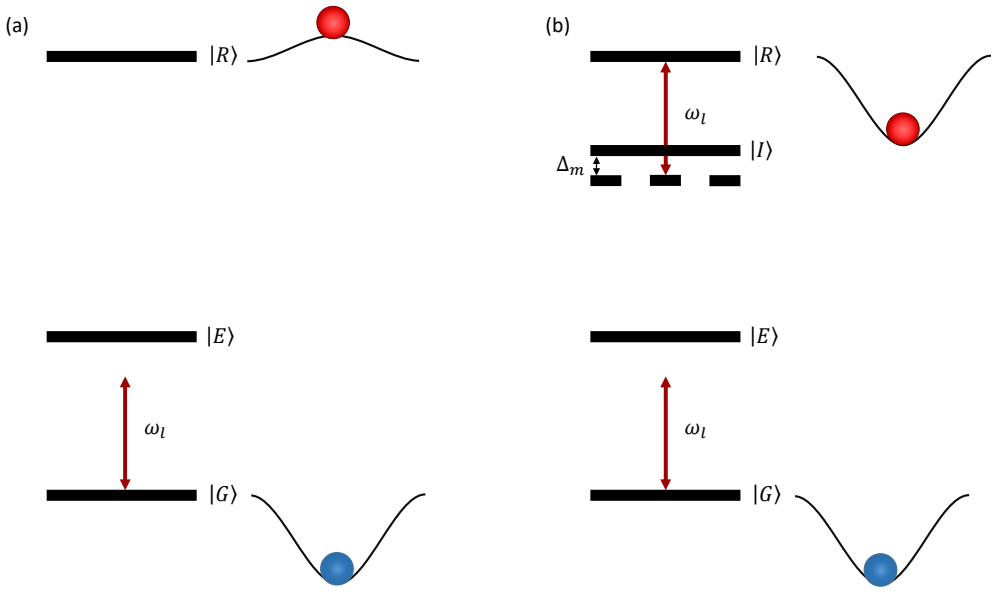

Figure 1.2: (a) An energy level diagram and the spatial dependence of the energy level shift for the ground and Rydberg level in a far detuned dipole trap made from a Gaussian beam. (b) The same energy level shifts for a dipole trap that is near resonance with an intermediate state. At a particular frequency, the two spatial modes can be matched. This frequency is referred to as the "magic" frequency.

1.5 Photon correlations

The generation and characterization of non-classical states of light are important for a broad range of physics experiments even outside of the field of quantum optics. For example, at the Laser Interferometer Gravitational-wave Observatory (LIGO), a squeezed-state of light is being used in the interferometer to measure the vibrations of spacetime due to gravitational waves [3]. This non-classical state of light is used because it has a better signal-to-noise ratio when measuring the relative phase than classical light. This thesis focuses on the study of single-photon states, multi-photon states, and coherent states. Our main tool to study these states is the second-order correlation function, $g^{(2)}$.

To measure $g^{(2)}$ the Hanbury Brown-Twiss (HBT) method is typically used [31]. A simplified scheme of the HBT setup is shown in Figure 1.3, where a beam splitter splits

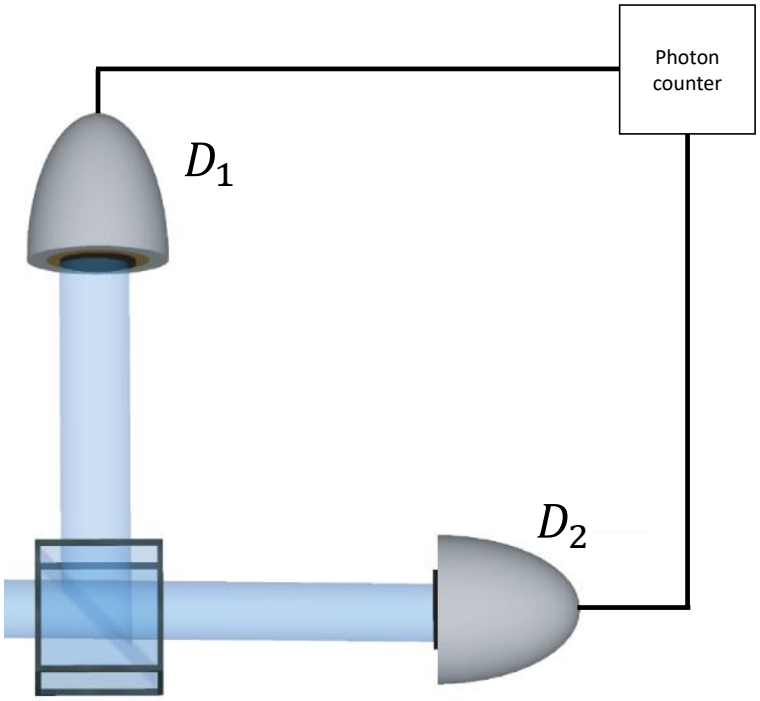

Figure 1.3: Diagram of a setup for the Hanbury Brown-Twiss method where a beam is divided between two detectors and the photons are counted in D_1 and D_2, as well as the coincidences between the two detectors.

an incoming light field between two detectors, D_1 and D_2. The number of photoelectric detection events in each detector, C_1 and C_2, and the number of coincidence counts between the two, C_{12}, are recorded. A coincidence count is defined as detection events in D_1 and D_2 with some separation τ. It is useful to change these raw numbers of counts and coincidences into a probability of detection or coincidence (P_1, P_2, P_{12}) for a given time period.

Let us assume we have some electric field ($E^+(t)$) that is incident on an HBT setup and we want to see what temporal correlations there are in that electric field (the "+" denotes positive frequencies, and, while nonphysical, negative frequencies, $E^-(t)$, can be formally allowed). Then, what we are interested in is the electric field at time t, $E^+(t)$, and at time $t+\tau$, $E^+(t+\tau)$. If we take the expectation value of these and normalize by the intensity of the field, one can derive a measure of second-order correlations $g^{(2)}(\tau)$ to be [32]:

$$g^{(2)}(\tau) = \frac{\langle E^-(t)E^-(t+\tau)E^+(t+\tau)E^+(t)\rangle}{\langle E^-(t)E^+(t)\rangle^2}. \tag{1.7}$$

For pulsed fields the expression is

$$g^{(2)}(\tau) = \frac{\langle E^-(t)E^-(t+\tau)E^+(t+\tau)E^+(t)\rangle}{\langle E^-(t)E^+(t)\rangle\langle E^-(t+\tau)E^+(t+\tau)\rangle}. \tag{1.8}$$

Experimentally $g^{(2)}(\tau)$ is time integrated such that,

$$g^{(2)}(\tau) = \frac{\int dt_1 \int dt_2 \langle E^-(t_1)E^-(t_2)E^+(t_2)E^+(t_1)\rangle}{\left[\int dt \langle E^-(t)E^+(t)\rangle\right]^2}, \tag{1.9}$$

The numerator, $\int dt_1 \int dt_2 \langle E^-(t_1)E^-(t_2)E^+(t_2)E^+(t_1)\rangle$, is proportional the number of coincidences over the integration time. Experimentally we measure this as P_{12}. Then there is the matter of normalizing the second-order correlations. Through this thesis there are several normalization used for coincidences, for example, when we measure photons from the ensemble to check if the output is a single-photon state we use:

$$g^{(2)}(\tau) = \frac{P_{12}(\tau)}{P_1 P_2}, \tag{1.10}$$

where $P_{12}(\tau)$ is the probability of having a count in detector 1 and detector 2 separated by time, τ. While τ can be any period of time, $\tau = 0$ describes the nature of the photon statistics for the field. If $g^{(2)}(0) > 1$, the statistics of the field are super-Poissonian. Light fields, in this case, have more correlations than would be produced by independent photons, so the photons are "bunching" together. If $g^{(2)}(0) = 1$, the statistics of the field are Poissonian. This is the case for photons that are completely independent of each other because for any independent probabilities $P_1 P_2 = P_{12}$. Also, $g^{(2)}(0) = 1$ for a coherent state. Finally, if $g^{(2)}(0) < 1$, the state is sub-Poissonian. These states are referred to as "antibunching". The lowest possible $g^{(2)}(0)$ is zero. This is when there are no coincidence counts from a light field. This case corresponds to a perfect single-photon state. In fact, it can be shown that for Fock states, such as the single-photon state, the second-order correlation function is [32]:

$$g^{(2)}(0) = 1 - \frac{1}{n}, \tag{1.11}$$

where n is the number of photons in the Fock state. Using this formula we can tell how well our system produces single-photons and whether there is a negligible number of photons in the two-photon state.

Chapter 2

Experimental methods

2.1 Magneto-optical trap (MOT)

In this thesis, a dual-MOT system was used to collect ^{87}Rb atoms in a high vacuum system. The dual-MOT system consists of two sections: a chamber with low vacuum and a chamber with high vacuum. On the low vacuum side, an ampule of Rb serves as the source of atoms for the system. A line of ^{87}Rb atoms is gathered in a glass cell using a two-dimensional (2D) MOT. A pushing beam is used to transport the atoms from the low vacuum side through a differential vacuum tube to a high vacuum chamber where a three-dimensional (3D) MOT is used to collect the atoms. Both the 2D and 3D MOT beams have a wavelength of 780 nm and are detuned from the $|5S_{1/2}, F = 2\rangle \leftrightarrow |5P_{3/2}, F = 3\rangle$ transition by -13 MHz. Two tapered amplifiers supply the 2D and 3D MOTs with 300 mW and 100 mW, respectively. A repumping field resonant with the $|5S_{1/2}, F = 1\rangle \leftrightarrow |5P_{3/2}, F = 2\rangle$ transition is used in both the 2D and 3D MOTs to prevent the atoms from accumulating in $|5S_{1/2}, F = 1\rangle$. The 3D MOT is in high vacuum to reduce the collision rate of Rb atoms with background atoms resulting in MOT and dipole trap lifetimes of ≈ 10 s. The 2D MOT creates a large flux of atoms such that the 3D MOT can collect $\sim 10^{10}$ atoms in a 1 s loading time. The pressure in the high vacuum side is $< 10^{-10}$ Torr as measured by a NEXTorr pressure gauge [33]. Once

the atoms are loaded into the 3D MOT, the pushing beam is turned off in order to isolate the 3D MOT from the low vacuum section. To cool the atoms in the MOT the 780 nm fields are detuned by an additional ≈ 55 MHz for a period of 40 ms. The repumper is reduced to one-tenth of its original power allowing a fraction of the atoms into the $|5S_{1/2}, F = 1\rangle$ state to suppress light assisted collisions, that can eject atoms from the trap.

2.2 Experimental setup

Several excitation schemes and trap geometries are used throughout this thesis. The arrangement of each of the optical fields in relation to the glass cell for the 3D MOT is shown in Figure 2.1. To prepare the atoms for the experimental sequences, the atoms are transferred from the 3D MOT to either an optical lattice or a cross-dipole trap over the course of 50 ms. The optical lattice is used for experiments where long-lived coherence between the ground and the Rydberg state is required (see Chapters 4 and 5). The lattice is formed by a retro-reflected 1012 nm beam. The 1012 nm beam is overlapped with the excitation beams using four Semrock dichroic mirrors [34]. To generate the linear polarization of the 1012 nm incident lattice beam at the position of the atoms, we use a polarizing beam splitter, a half-wave plate, and a quarter-wave plate before the dichroic mirrors. A quarter-wave plate, a half-wave plate, and a Glan-Thompson polarizer are used to ensure the retroreflection has the same polarization as the incident field. An axis system was chosen with the lattice along the x-axis. The length of the ensemble in the lattice, along the x-axis, was ≈ 0.4 mm. The length is determined by the size of the MOT at the time of loading.

A cross-dipole trap is used to gather a dense sample of atoms at the intersection of two beams from a 1064 nm Nd:YAG laser for experiments with non-classical states in Chapter 3. The polarizations of the two beams are orthogonal so a lattice is not formed. The beams were focused such that the waist was $w_x \approx 30$ μm along the x-axis. The ensemble fills a portion of the trap and has a total length of $L_d \approx 35$ μm, in the x-direction, less than the

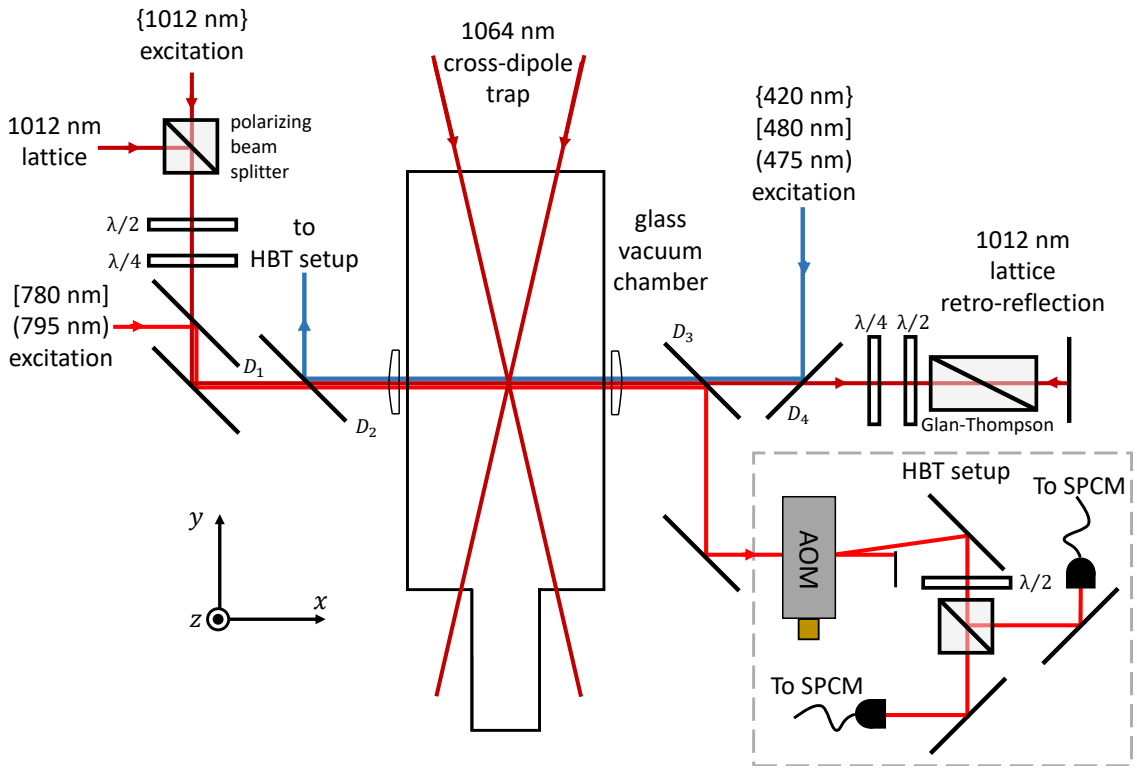

Figure 2.1: The geometry of the excitation and trapping fields. For each experiment, a pair of fields are used for the two-photon excitation to Rydberg; these pairs are 420/1012 nm, 795/475 nm, and 780/480 nm. These fields are overlapped with the lattice using four dichroic mirrors D_1, D_2, D_3, and D_4. A 5 cm achromatic lens is used on either side of the cell for focusing the beams. A Hanbury Brown-Twiss (HBT) setup is used to detect ensemble emission (795 nm and 780 nm). A half-wave plate before a polarizing beam splitter is used to divert power to one or both of the single-photon counting modules. A similar HBT setup (not shown in the diagram) was used to collect and analyze 420 nm photons. The 1012 nm lattice beam is retro-reflected to create the optical lattice used for experiments that required long ground-Rydberg coherence times. A 1064 nm cross-dipole trap is used to create a trap with a length along the x-direction that is smaller than a Rydberg blockade radius at $n > 75$. The polarization, magnetic fields, and optical pumping beams vary between experiments depending on what magnetic sublevel of $|5S_{1/2}\rangle$ the atoms are initialized in.

Rydberg blockade radius at a principal quantum number of $n > 75$. In the z-direction, the waist of the cross-dipole trap beams is $w_z \approx 60$ μm. The cloud of atoms is much larger than the waist of the excitation beams, therefore, the cloud is approximately uniform with respect to the excitation beams radially. Both the optical lattice and the cross-dipole trap are aligned such that atoms could be loaded into the cross-dipole trap and then transferred into the lattice by adiabatically lowering the cross-dipole trap while raising the optical lattice. The ensemble of atoms that is produced from the transfer is $L \approx L_d$ in length, as opposed to $L \approx 0.4$ mm long when the ensemble is loaded directly from the MOT. The transferred ensemble is occasionally used for diagnostics such as checking the alignment of the lattice or the cross dipole trap.

The two-photon excitation schemes we use are 420/1012 nm, 795/475 nm, and 780/480 nm with the intermediate states $|6P_{3/2}\rangle$, $|5P_{1/2}\rangle$, and $|5P_{3/2}\rangle$, respectively. The excitation beams and the lattice beams are collinear along x. The pairs of $420/1012$ nm and $795/475$ nm are used for experiments in the optical lattice. $780/480$ nm is used in Chapter 3 for experiments with non-classical states. For all excitation schemes, there is a general protocol where the two excitation fields are pulsed on at the same time to excite the ensemble into the Rydberg state. The excitation is stored in the atoms for a time T_s . Finally, a retrieval pulse of 1012 nm, 475 nm, or 480 nm light is used to drive the ensemble from the Rydberg state to an intermediate state. A light field is then emitted from the ensemble. The emitted 420 nm, 795 nm, and 780 nm light is detected using a Hanbury Brown-Twiss setup [31]. To protect the single-photon counting modules (SPCMs) and decrease noise on the detectors an AOM is used for gating the retrieved photons. The gating allows light to reach the Perkins-Elmer SPCM [35] only at the time when atomic emission is present. This process is repeated several thousand times over the course of ~ 100 ms. Then the trap is dropped and a next MOT cloud of atoms is loaded. Several of the laser systems used to create the excitation and retrieval pulses are discussed in more detail later in this Chapter.

2.3 780 nm setup for Hanbury Brown-Twiss correlations for a driven superatom

This section explains the 780 nm excitation and probe pulse laser system for Chapter 3.

The laser setup for the 780 nm produces two pulses, one for excitation, and one for a probe pulse. The excitation pulse is detuned from the $|5S_{1/2}\rangle \leftrightarrow |5P_{3/2}\rangle$ transition by -90 MHz to suppress excited state populations in the $|5P_{3/2}\rangle$ level. In conjunction with the 480 nm excitation pulse, the 780 nm excitation pulse will excite the ensemble to $|nS_{1/2}\rangle$. The probe pulse detuning from the $|5S_{1/2}\rangle \leftrightarrow |5P_{3/2}\rangle$ transition can range from -90 MHz to

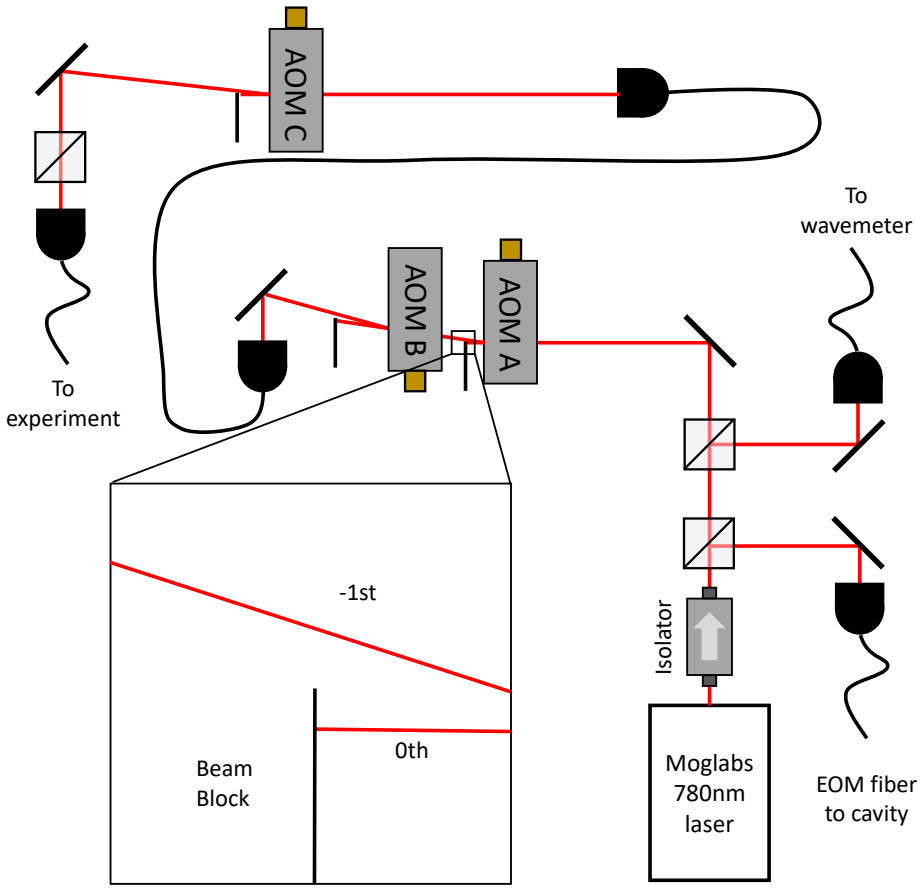

Figure 2.2: Setup of the 780 nm excitation and probe laser. The AOMs A, B, and C correspond to the AOMs in Figure 2.3.

$+30$ MHz. The temporal modes of the probe pulse and the ensemble emission are matched as closely as possible. The timing of the probe pulse is adjustable from 150 ns before the atomic emission to 150 ns after the atomic emission. Lastly, the spatial modes of both pulses are the same at the position of the atoms because both are coupled to the same fiber. These pulses of light are achieved with the laser system in Figure 2.2.

The 780 nm light is produced using a cat-eye reflector ECDL (MOGlabs CEL002) [36]. After an optical isolator, a fraction of the light is coupled to an EOSPACE fiber Electro-optic phase modulator (EOM) [37]. The output of the EOM is aligned to a Stable Laser Systems cavity [38] that has a free spectral range of 1.5 GHz and a finesse of $F \approx 10,000$. The laser is frequency locked to the cavity using the Pound-Drever-Hall technique [39]. The EOM was used for modulating the light and providing a frequency sideband. This sideband allowed us to lock at frequencies other than the zeroth order mode of the cavity. A Toptica PDD 110 [40] was used to produce an error signal and a Toptica FALC 110 [40] provided feedback to the laser. The laser linewidth when locked is ≈ 50 kHz. A High-Finesse wavemeter [41] was used to monitor the frequency of the laser and has an accuracy of < 10 MHz when calibrated using the $|5S_{1/2}\rangle \leftrightarrow |5P_{3/2}\rangle$ transition.

Three acousto-optic modulators (AOMs) are used to produce the correct frequencies and temporal shapes for the excitation and probe pulses. The first two AOMs, A and B, are used to control the frequency of the 780 excitation and probe pulses. These AOMs are used in the configuration depicted in Figure 2.2 to have a large frequency tuning range and provide better suppression of unwanted light leakage than a double-pass AOM system. The fiber in between AOM B and AOM C is to ensure the spatial mode to the third AOM does not change. Without the fiber, different frequencies in AOM A and AOM B would slightly change the beam position on AOM C. The different position on the crystal of AOM C would result in different travel times of the acoustic wave, thereby changing the optical pulse timing. With the fiber, only the coupling efficiency changes with different frequencies in AOMs A and B. More radio frequency (RF) power directed to the AOMs can compensate for the

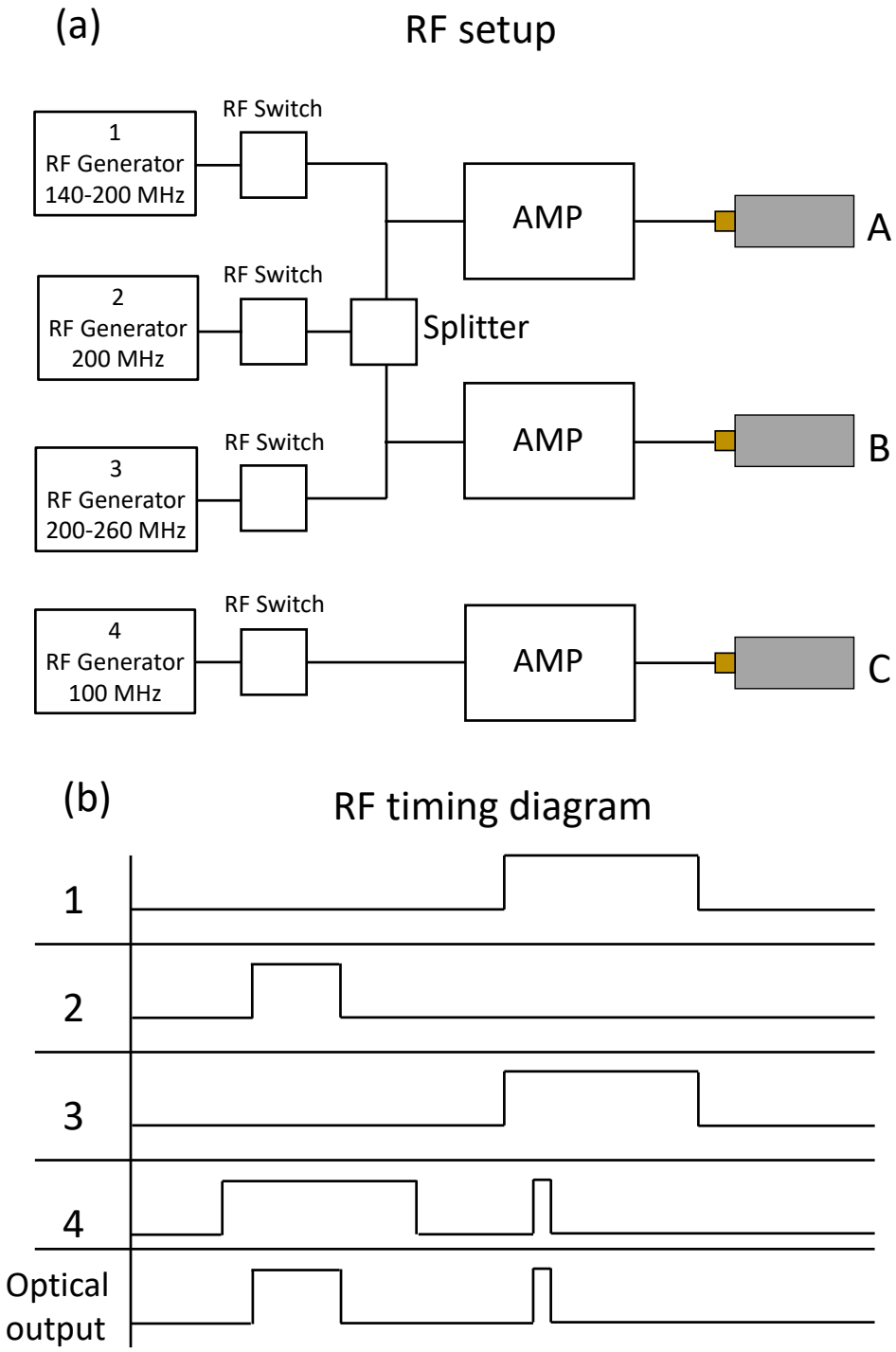

Figure 2.3: (a) The RF setup for 780 nm AOMs A, B, and C. Frequency generators $1-4$ are used to drive the three AOMs. The RF switches determine when the frequency from each of the 4 RF generators is allowed to the AOMs. The splitter is placed such that generator 2 can drive both AOMs A and B while generator 1 can only drive AOM A and generator 3 can only drive AOM B. Generator 4 can only drive AOM C. (b) The timing diagrams for the RF switches connected to generators $1-4$. The final timing diagram shows the optical output to the experimental setup where the first pulse is for excitation and the second pulse is the probe.

coupling efficiency. While the overall efficiency of coupling to the fiber is low for the probe pulse ($\sim 1\%$), only a few photons are needed to interfere with the ensemble emission. The excitation pulse is nearly aligned to the fiber and only needs a maximum power of ~ 10 nW. AOM C is used to shape the probe pulse and make the timing consistent for all detunings. Neutral density filters are used to attenuate the background light coupled into the fiber that is connected to the experimental table.

The RF frequencies and pulse timing are shown in Figure 2.3. The frequency of the laser is chosen by the following method: using the same driving frequency for AOMs A and B (generally 200 MHz), the 780 nm absorption spectrum of the Rb ensemble is measured. The laser is frequency locked such that the light to the experimental table has a frequency 90 MHz less than the $|5S_{1/2}\rangle \leftrightarrow |5P_{3/2}\rangle$ transition frequency. This frequency of light is used for the 780 nm portion of the two-photon excitation scheme as is shown in the timing diagram Figure 2.3 (b). For the probe pulse, an RF frequency between 140 and 200 MHz is sent to AOM A and an RF frequency between 200 and 260 MHz is sent to AOM B. Because AOM A uses the minus first order and AOM B uses the plus first order, the resulting probe detuning is between -90 MHz and $+30$ MHz with respect to the $|5S_{1/2}\rangle \leftrightarrow |5P_{3/2}\rangle$ transition. The third AOM has a constant frequency and is pulsed on for the excitation. (The length of the excitation pulse is controlled by AOMs A and B.) Then, AOM C is pulsed on for a short amount of time to control the duration and timing of the probe pulse. All RF generators $(1-4)$ used for the 780 nm excitation and retrieval were WindFreak Technologies SynthNV RF generators [42].

2.4 480/475 nm setup for Hanbury Brown-Twiss correlations for a driven superatom

This section explains one of the laser systems for Chapter 3.

To provide light for the $|5P_{3/2}\rangle \leftrightarrow |nS_{1/2}\rangle$ transition, a cat-eye reflector ECDL (MOGlabs

CEL002) is used. The laser has a wavelength range from 940 nm to 970 nm. When the beam is frequency doubled, light can be produced from 470 nm to 485 nm. This wavelength range can drive the transition from either $|5P_{1/2}\rangle$ (475 nm) or $|5P_{3/2}\rangle$ (480 nm) to principal quantum numbers $n > 30$. Generally for our setup 480 nm is used. The laser setup is shown in Figure 2.4 (a). First, a small fraction of the light is sent through a fiber EOM to a Stable Laser Systems cavity for locking the laser, in a similar fashion to the 780 nm frequency locking setup described in the previous section. After the pick-off for the cavity, some light is diverted to a wavelength meter to monitor the frequency of the light.

The laser light not used for locking or monitoring is aligned to a tapered amplifier that produces an output power of $\approx$ 1 W of 960 nm light. The output light is then directed through an isolator to a Toptica SHG Pro [40] for the second-harmonic generation. The SHG uses a non-linear crystal in a bow-tie cavity to double the frequency of the 960 nm light and produces ≈ 300 mW of 480 nm light. The 480 nm beam is used to produce two pulses of light; one pulse for the two-photon excitation scheme and the other (retrieval) pulse to drive the ensemble from the Rydberg state to the intermediate state. The atoms will emit 780 nm light when they decay from the intermediate state to the ground state. The emitted photon is collected using SPCMs. The excitation light is detuned from the $|5P_{3/2}\rangle \leftrightarrow |nS_{1/2}\rangle$ transition by $+90$ MHz to match the 780 nm detuning. The retrieval pulse is resonant with the $|nS_{1/2}\rangle \leftrightarrow |5P_{3/2}\rangle$ transition. These two pulses of light are achieved by using two AOMs. AOM A is driven with a frequency of 200 MHz and produces a negative first-order beam that is used for the retrieval pulse. The excitation pulse is made by the negative first-order of AOM B. The driving frequency for AOM B is 110 MHz. To save optical power, the negative first order of AOM A is overlapped with the negative first order of AOM B through the crystal of AOM B. The two AOMs are never on at the same time, as shown in the timing diagram in Figure 2.4 (b). Therefore, this overlap on the AOM will not result in unwanted frequencies of light. Using this AOM arrangement we are able to send as much light as possible, up to 75 mW, for both the excitation and retrieval pulses. To find the correct frequencies of 480 nm

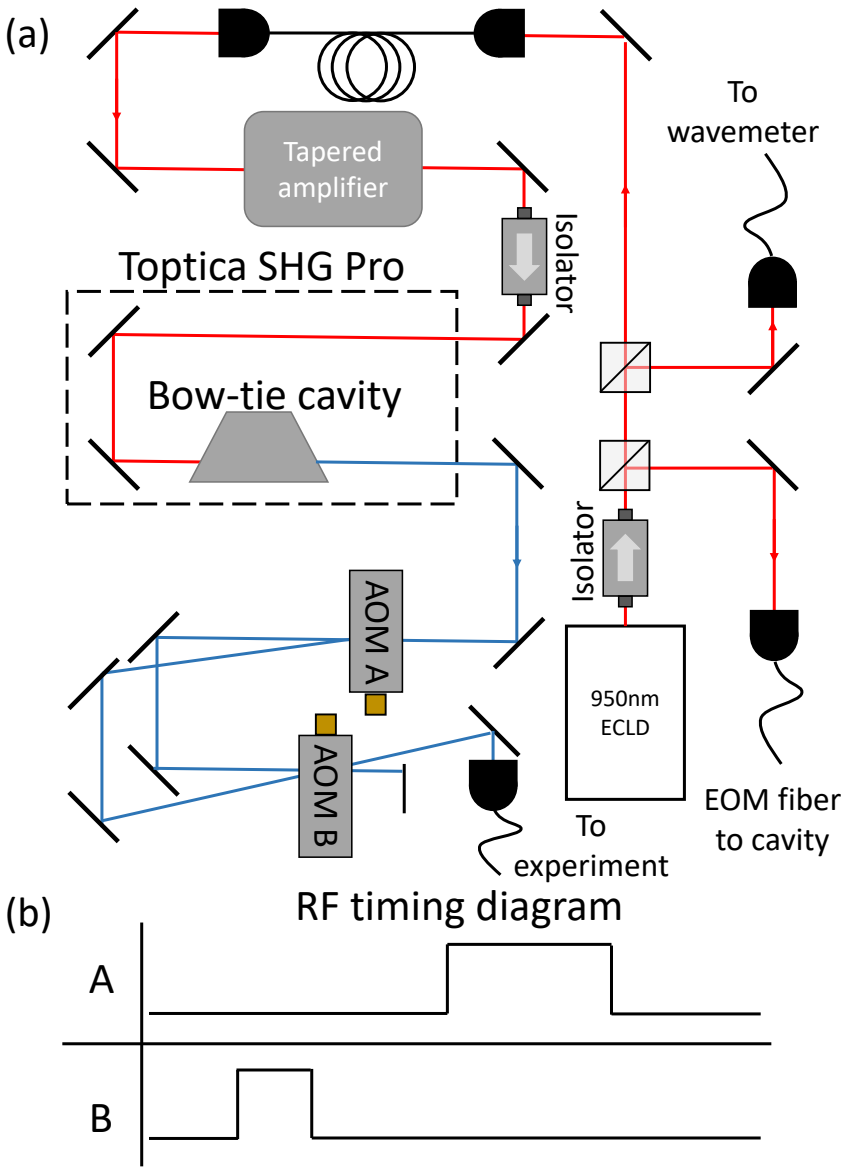

Figure 2.4: (a)Setup of the 480 nm excitation and retrieval laser system. (b) Timing diagram showing the timing for the excitation and retrieval pulses controlling AOMs A and B.

pulses, we use the following procedure:

1. The $|5S_{1/2}\rangle \leftrightarrow |5P_{3/2}\rangle$ transition is measured through the method of absorption spectroscopy using the 780 nm probe pulse.

2. The 780 nm laser is frequency-locked 90 MHz below the resonance measured in the previous step.

3. The 480 nm excitation frequency is set to be 90 MHz more than the frequency used for retrieval using the AOMs in Figure 2.4.

4. The pulse timing is made such that the 780 nm and 480 nm excitation pulses occur at the same time and the 480 nm retrieval pulse occurs after 1 μs of storage time.

5. The frequency of the 480 nm laser is scanned while measuring the ensemble emission using the SPCMs.

6. The frequency of the 480 nm laser with the maximum retrieved photons from the Rydberg state is where the 480 nm retrieval pulse is on resonance with the $|5P_{3/2}\rangle \leftrightarrow |nS_{1/2}\rangle$ transition and the two-photon excitation is resonant with the $|5S_{1/2}\rangle \leftrightarrow |nS_{1/2}\rangle$.

The frequency of the 480 nm retrieval field is double-checked by using electromagnetically induced transparency (EIT). This is done by putting the 780 nm probe pulse on resonance with the $|5S_{1/2}\rangle \leftrightarrow |5P_{3/2}\rangle$ transition. The power of the probe pulse can be measured with the SPCMs. When the ensemble is present the atoms will absorb some of the probe light. However, if the 480 nm frequency is scanned over the $|5P_{3/2}\rangle \leftrightarrow |nS_{1/2}\rangle$ transition the ensemble will be made transparent to the probe pulse. The frequency that makes the ensemble most transparent to 780 nm light is the 480 nm retrieval frequency. This frequency should be the same as in step 6.

2.5 Matching the temporal modes of the probe pulse and the atomic emission

To match the temporal mode of the probe pulse with the ensemble emission, we used two parameters, the probe pulse length and the 480 nm power. The probe pulse length was controlled by AOM C in Figure 2.2. By adjusting the pulse length we achieved an approximately Gaussian probe pulse with a duration between 40 ns and 100 ns. The power

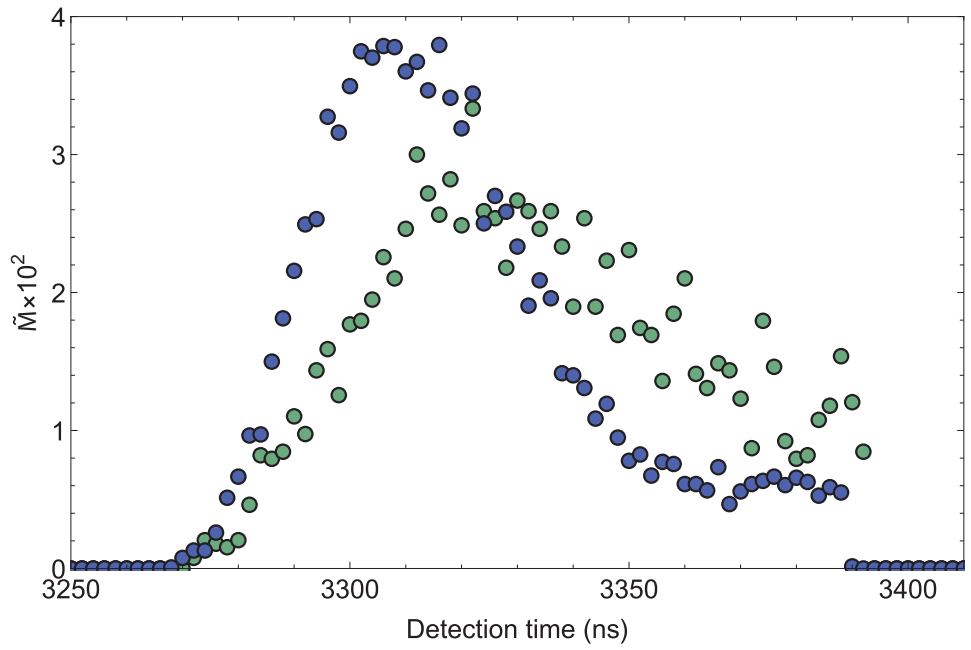

Figure 2.5: Normalized photocounts $\tilde{M}$ as a function of time for two different 480 retrieval powers. The x-axis is the detection time of the photons relative to an arbitrary trigger time. The temporal profiles of the atomic emission for two different 480 powers: blue ~ 10 mW and green ~ 1 mW. The y-axis shows the probability of receiving a photon at a given time with 2 ns binning. $\tilde{M}$ is normalized such that the sum of all data points is one.

of the 480 nm field determined the length of the photon emission from the atom for our experiment. Generally, we had low enough power that the limitation of the length of the temporal profile was the time needed to drive the ensemble from the Rydberg state to the intermediate state. The Rabi frequency of the transition scales as $\Omega \propto \sqrt{P}$, therefore, four times as much 480 nm optical power will produce a temporal profile that is approximately half as long. This approximation starts to break down when the Rabi frequency approaches the decay rate of the intermediate state. Figure 2.5 shows the temporal profiles of the retrieved photons from the ensemble at two different 480 nm powers. The laser system for producing 480 nm light is discussed in the previous section.

Using these two parameters, we were able to match the temporal profiles of the electric fields for the probe pulse and the atomic emission to 95%. The temporal overlap J is calculated using the formula:

$$J = \frac{\int \sqrt{I_e(t) I_p(t)} dt}{\sqrt{\int I_e(t) dt \int I_p(t) dt}} \tag{2.1}$$

where J is the overlap, $I_e(t)$ is the temporal intensity profile of the emitted field, and $I_p(t)$ is the temporal intensity profile of the probe field (this equation is expressed in terms of electric fields in Chapter 3.) $I_e(t)$ and $I_p(t)$ were measured using SPCMs connected to a FAST Com Tech P7888 4-input multiple-event time digitizer [43].

When the temporal modes are optimally matched, the two temporal profiles can be approximated as Gaussian pulses with $\frac{1}{e}$ waists of $\tau_{e,p} \approx 35$ ns. The number of coincidences is measured under two situations. Either the timing of the two pulses is the same and the frequency of the probe is scanned, or the frequency of the two pulses is the same and the probe timing was scanned. In the case of scanning the detuning, we can improve the temporal matching by using post-selection to discard the photons on the tails of each of the pulses where the mismatch between the temporal profiles is the greatest. The post-selection cannot be applied when varying the timing of the probe pulse relative to the atomic emission because the probe pulse needs to be shifted by up to ± 150 ns and tails cannot be easily disregarded.

2.6 Data normalization for Hanbury Brown-Twiss correlations for a driven superatom

This section explains how we normalized coincidences from an HBT setup in Chapter 3.

In Chapter 3 the goal is to measure the "enhancement factor" in the number of coincidences in an HBT setup. The coincidences are a result of the probe pulse and the ensemble emission interference. The enhancement factor is a measure of how many more coincidences occur when the probe pulse and the atomic emission are overlapped, as opposed to when they are widely separated in time. To calculate the enhancement factor of coincidences, the coincidences must be normalized for each time-integrated data point. The normaliza-

tion factor is calculated for each data point individually because with the current setup the power of the probe and the number of counts from the ensembles are not consistent. The inconsistency results from when the frequency of the probe is changed, using the AOMs, the power of the probe also changes, as explained in Section 2.3. These power variations are partially compensated for by adjusting RF power to the AOMs controlling the probe, however, more precise control is required to completely equalize the powers from measurement to measurement. Another source of probe pulse power variation is from changing the delay of the probe pulse. Changing the delay moves the pulse from times when the 480 nm retrieval light is on to times when the 480 nm retrieval light is off. The 480 nm retrieval light is resonant with the $|5P_{3/2}\rangle \leftrightarrow |nS_{1/2}\rangle$ transition which causes EIT for the probe light. Because the 480 nm light makes the ensemble transparent, more 780 photons are transmitted through the ensemble. Both the variation in fiber coupling and in EIT change the power of the probe pulse causing the number of coincidences in the HBT setup to change. Therefore, the number of coincidences has to be normalized for each data point.

As explained in the next Chapter, we expect approximately twice as many coincidences when the probe pulse and the ensemble emission are temporally and spectrally overlapped as when they have different timings or frequencies. We normalize so the number of coincidences of widely separated pulses is equal to 1. The enhancement factor will be approximately equal to the normalized coincidences when the two pulses are overlapped. When the pulses are widely separated in time, they are completely independent. We can measure the probability of detection, for a given trial, in both of the detectors in the HBT setup for the probe beam, P_{p1} and P_{p2}, and the atomic emission, P_{e1} and P_{e2} (1 and 2 denoting detectors $D1$ and $D2$.) For two independent fields, the probability of a coincidence P_{norm} for a given trial is calculated to be,

$$P_{norm} = P_{p1}P_{p2} + P_{p1}P_{e2} + P_{e1}P_{p2} + P_{e1}P_{e2}g^{(2)}(0), \tag{2.2}$$

where $g^{(2)}(0)$ is the second-order correlation function for the ensemble.

The procedure for normalization is P_{p1}, P_{p2}, P_{e1}, and P_{e2} are measured. Then the coincidence rate with both fields on is measured, P_{12}, over the course of $1-2$ hours for a given delay or detuning between the pulses. After P_{12} is measured, P_{p1}, P_{p2}, P_{e1}, and P_{e2} are measured again to check if there have been any drifts in the probability of detection since the beginning of the measurement. For each P_{12} measurement, we calculate the corresponding P_{norm} normalization factor by averaging the two measurements of P_{p1}, P_{p2}, P_{e1}, and P_{e2} and using Equation 2.2. We normalize each point individually using the formula,

$$N_c = \frac{P_{12}}{P_{norm}}. \tag{2.3}$$

The normalized coincidences N_c are measured for different detunings and delays between the pulses and then fit with a model discussed in the next Chapter.

2.7 Trap geometry for optical lattice

This section explains the geometry of the optical lattice in Chapters 4 and 5.

When measuring the ground-Rydberg coherence in a state-insensitive optical lattice, spatial averaging over differential shifts due to the non-lattice potentials is a limiting factor in the ground-state–Rydberg-state coherence time. One way to improve the coherence time is by making the ratio between the waists of the lattice (w_l) and the excitation (w_e) beams as large as possible ($\frac{w_l}{w_e} \gg 1$), as is further explained in Chapter 4. This could be accomplished by decreasing the excitation radius at the atoms. However, the lens used to focus the excitation beams has a focal length of 5 cm. The numerical aperture of this lens is too small for the excitation beam to have a spot size $\ll 10$ μm. Alternatively, the lattice waist could be increased. However, the lattice waist is also limited by the 5 cm lens. If we wanted a lattice waist of $w_L \approx 100$ μm, the Rayleigh length of the beams is $z_R = \frac{\pi w_L^2}{\lambda} \approx 3.1$cm. Since z_R

is on the order of the lens focal length we could not make the trap waist the size that was required.

Due to geometric constraints, we kept the 5 cm lens. To have a larger lattice radius at the atoms, the focus of the 1012nm lattice beams was shifted away from the atoms. The atoms are confined along the axial direction of the lattice beams so the atoms are held where they are loaded. To align this geometry, we used the following procedure:

1. A collimated 1012 nm beam is aligned to the 5 cm lens and is used to form a dipole trap.
2. The dipole trap is imaged on an Andor Solis iKon-M camera [44].
3. The incident 1012 nm beam is aligned onto the MOT.
4. Irises are used to define a spatial mode that is aligned to the MOT.
5. A 30 cm lens is added to the incident 1012 nm beam path to focus the lattice beam 35 cm before the 5 cm lens. As a result, the 1012 nm light is divergent at the lens.
6. The new spatial mode is aligned with the irises that were set up in step 4.
7. After the 1012 nm light passes through the MOT and exits the glass cell, the 1012 nm lattice beam is collimated.
8. The collimated 1012 nm light is retro-reflected to form the lattice.
9. Fluorescence from the atoms in the lattice is imaged on the camera and used as a proxy for the number of atoms.
10. The retro-reflection is adjusted to maximize the fluorescence signal.

Following this procedure, we were able to load an optical lattice from a MOT with the focus of the lattice beams far from the MOT.

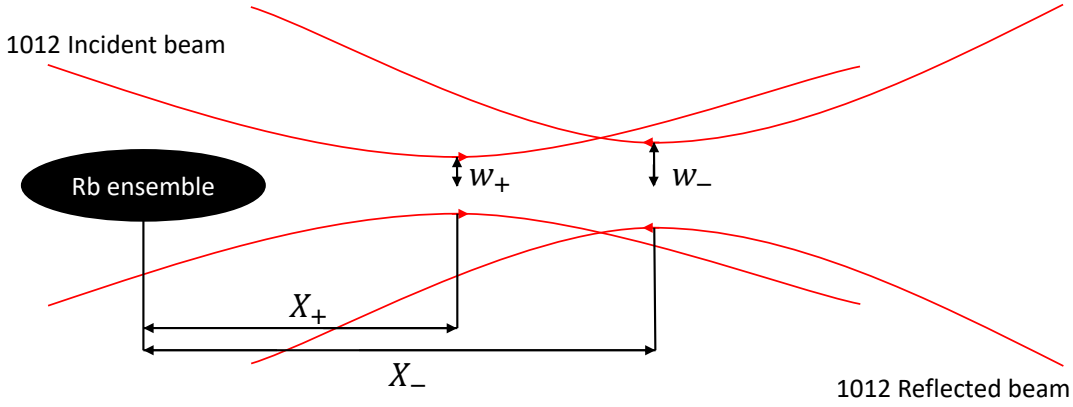

Figure 2.6: Diagram showing the position of the focus of the two lattice beams with respect to the ensemble of Rb atoms (not to scale). The displacement and waist of the incident (reflected) beam is labeled X_+ (X_-) and w_+ (w_-), respectively.

Figure 2.6 shows the position of the ensemble relative to the position of the incident and retro-reflected foci. The geometry for Chapters 4 and 5 is: an incident beam focused $X_+ = 7.9$ mm off the MOT center with a waist of $w_+ = 33$ μm. The retro-reflected beam is focused $X_- = 23.9$mm off the MOT center with a waist of $w_- = 68$ μm.

2.8 Measuring magic frequency

This section explains how the magic frequency of the optical lattice has been measured in Chapter 4.

To implement state-insensitive trapping, we measured the so-called "magic" detuning from the $|6P_{3/2}\rangle \leftrightarrow |nS_{1/2}\rangle$ transition for multiple principal quantum numbers. Depending on the principal quantum number the magic value occurred when blue detuned by between 0.1 and 6 GHz. The required wavelength of light to be slightly detuned from the $|6P_{3/2}\rangle \leftrightarrow |nS_{1/2}\rangle$ transition, λ_L, is between 1012 nm and 1035 nm depending on the principal quantum number. A separate 1012 nm field is used in conjunction with a 420 nm pulse to excite the ensemble to the Rydberg state.

Figure 2.7(a) shows the laser system for the 1012 nm excitation and retrieval pulses. The light is produced by a MOGlabs CEL002 laser that is locked to a cavity in a similar fashion to 780 nm and 480 nm. The wavelength of the excitation and retrieval laser is monitored using a Highfinesse WS-8 wavelength meter. The excitation is detuned from resonance by $+12$ MHz from the $|6P_{3/2}\rangle \leftrightarrow |nS_{1/2}\rangle$ transition and the retrieval pulse is on resonance. The timing diagram for these two pulses is shown in Figure 2.7(b). To achieve these two pulses, we use two AOMs A and B. We drive AOM A with 92 MHz for the excitation pulse, and AOM B at 80 MHz for the retrieval pulse. The first-order of each AOM is overlapped and coupled to an optical fiber connected to the experimental table. To find the correct frequency for the 1012 nm laser to be locked, first, the frequency of the $|5S_{1/2}\rangle \leftrightarrow |6P_{3/2}\rangle$ transition is found using the absorption spectra for 420 nm light. The 420 nm excitation is then detuned by -12 MHz from the transition. The frequency of the excitation and retrieval laser is scanned to maximize the number of photons retrieved from the ensemble at short storage time, < 1 μs. This procedure ensures that the retrieval pulse is resonant with the $|6P_{3/2}\rangle \leftrightarrow |nS_{1/2}\rangle$ transition and the two-photon transition is resonant with the $|5S_{1/2}\rangle \leftrightarrow |nS_{1/2}\rangle$ transition.

The lattice beam is generated by an M Squared SolsTiS Ti:Sapph laser [45], which has a wavelength range from 850 nm to 1050 nm. The laser system setup as shown in Figure 2.7(c). Several milliwatts of the light are sent to a High Finesse WS-8 wavelength meter. The frequency of the light is read by the wavemeter. Long timescale fluctuations in the laser frequency are stabilized using a PID feedback locking scheme provided by the HighFinesse wavemeter. The Ti:Sapph is stable over short timescales, so the feedback is sufficient to lock the laser to the accuracy of the wavelength meter, < 10 MHz which is sufficient to measure the magic frequency. All of the Ti:Sapph power not diverted to the wavemeter is aligned to an AOM that is driven at 80 MHz. The first-order of the AOM is coupled to a fiber connected to the experimental table. The power of the incident beam for the lattice is ≈ 0.8 W at the position of the atoms.

To find the magic frequency the following procedure was used:

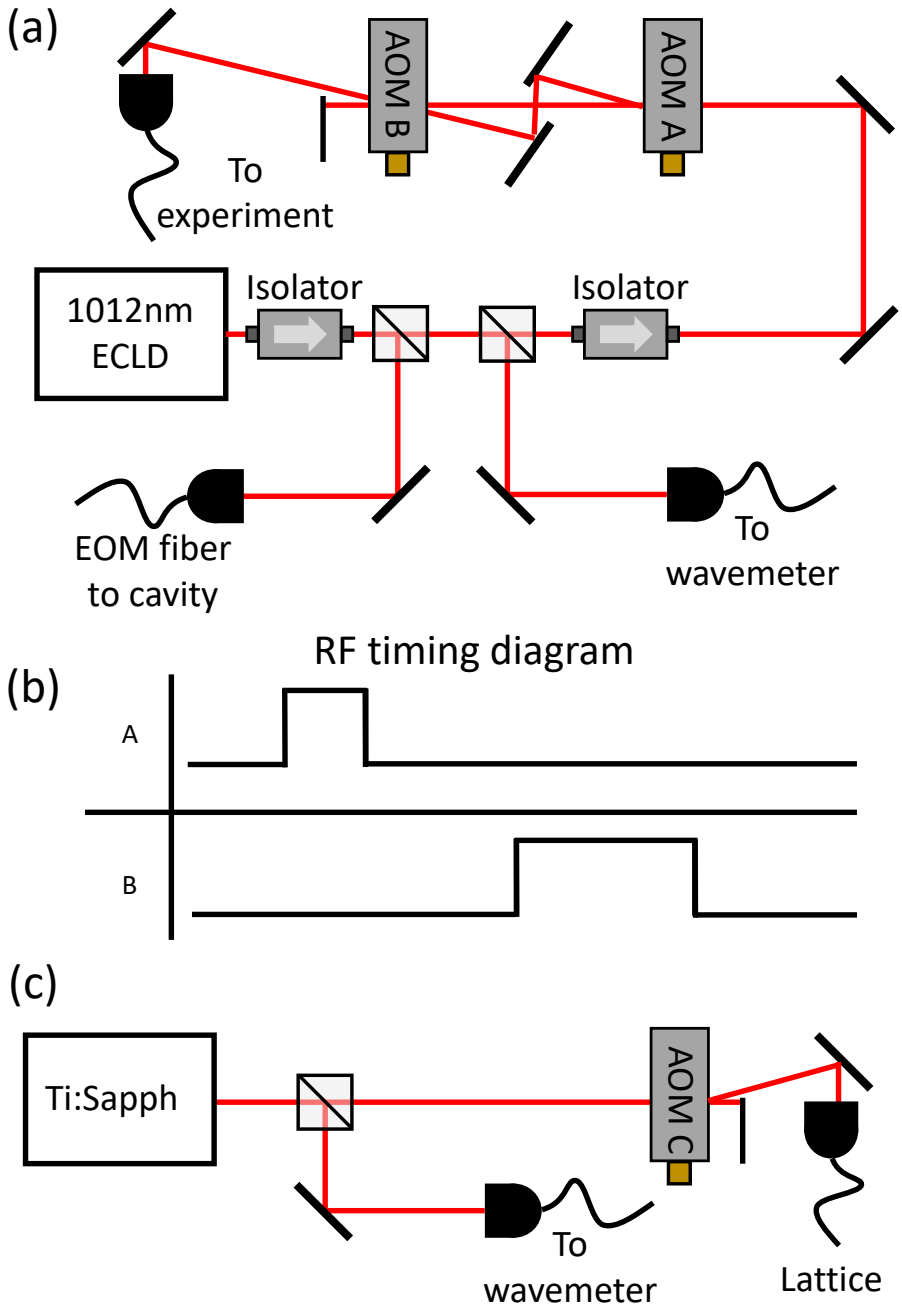

Figure 2.7: (a) The laser system for the 1012 nm excitation and retrieval pulses. (b) The timing diagram showing when AOMs A and B are on. (c) The laser system for the 1012 nm lattice.

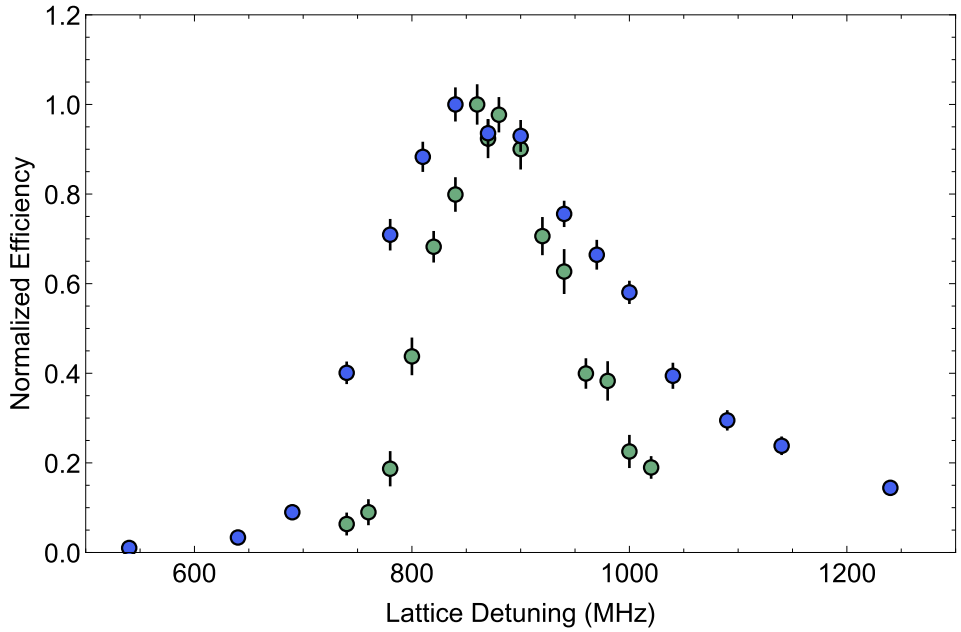

Figure 2.8: The normalized retrieval efficiency as a function of lattice detuning at $n = 59$. The blue points show the magic frequency peak after 12 μs of storage time. The green points show the magic frequency peak after 24 μs of storage time. The y-axis is normalized such that the maximum of each graph is equal to one.

1. The atomic sample is excited to the Rydberg state using a two-photon excitation scheme with 420 nm and 1012 nm light.

2. The excitation is stored in the ensemble for a duration of T_s.

3. A retrieval pulse of 1012 nm light is used to drive the Ryberg ensemble to the intermediate state resulting in the phase-matched emission of 420 nm photons.

4. The photons from the ensemble are collected with an SPCM.

5. The retrieval efficiency is calculated (the number of photons retrieved divided by the number of trials).

6. This process is repeated for different lattice wavelengths.

7. The retrieval efficiency as a function of lattice detuning is fit using the model explained in Chapter 4 to measure the magic wavelength.

Due to the finite temperature of the ensemble, the atoms oscillate along the axial direction of the lattice. For the magic frequency measurement procedure, T_s has to be after one atomic oscillation is completed. For our trap depth, the oscillation period is ≈ 12 μs. At this storage time, the magic detuning coincides with the maximum retrieved efficiency when scanning the magic wavelength.

The detuning of the lattice to the $|6P_{3/2}\rangle \leftrightarrow |nS_{1/2}\rangle$ transition is calculated by the difference between the 1012 nm retrieval pulse frequency and the lattice frequency on the wavemeter. The AOM frequency and order of deflection are the same for the lattice and the retrieval pulse, therefore, the AOM frequencies are ignored leaving only the difference in frequencies on the wavemeter. While the absolute frequency of the wavemeter is accurate to < 10 MHz the relative frequency difference between the 1012 nm retrieval light and the 1012 nm lattice is ≈ 1 MHz.

To extend coherence time as long as possible, we optimized the wavelength at longer storage times. Figure 2.8 shows the retrieved signal as a function of lattice detuning for two different storage times at $n = 59$. The blue points are taken after 12 μs of storage time (one complete atomic oscillation in the lattice). The green points are taken after 24 μs of storage time (two complete atomic oscillations in the lattice). The magic frequency peaks are narrower at longer storage times which makes the measurement more precise. These measurements were always taken after a complete atomic oscillation in the lattice.

Chapter 3

Hanbury Brown-Twiss correlations for a driven superatom

This chapter is based on Ref. [46]

3.1 Introduction

In his 1917 paper [47], Einstein introduced his famous A and B coefficients, with the A coefficient associated with spontaneous emission and the B coefficient to either absorption or stimulated emission (both referred to as "changes of state due to irradiation" by Einstein). While there may not be a universal definition as to what constitutes stimulated emission, any definition describes processes in which atom-field interactions lead to an increase in the intensity of an input field. There have been a number of both theoretical analyses and experimental implementations involving parametric down-conversion (e.g., Refs. [52, 48, 49, 50, 51, 53]) which have been interpreted in terms of stimulated emission and/or amplification. In all of these cases, coincidence counts involving both signal and idler modes are measured when a single-photon or a weak coherent probe pulse is sent into a crystal, so that it propagates collinearly with the signal mode. A two-fold increase in the time-integrated coincidence counts occurs for overlapping probe and signal field pulses, compared to the

case of non-overlapping pulses. The increase in coincidence counts was interpreted in terms of probe-induced stimulated emission in the crystal. The analyses supporting this assertion are based on a perturbative calculation of the evolution of the state vector associated with an effective Hamiltonian involving third-order nonlinear susceptibilities.

3.2 Theory

We have carried out an experiment that, in some ways, is analogous to the down-conversion experiments. Instead of a nonlinear crystal, our active medium consists of a gas of cold rubidium atoms, Figure 3.1(a). Following their release from an optical trap, the atoms are subjected to an excitation-deexcitation pulse sequence, leading to phase-matched emission in the x direction having central frequency ω_A. A weak probe pulse having central frequency ω_P is also sent into the sample in the x direction and can be delayed relative to the phase-matched emission pulse. The output field, containing contributions from both the input field and the field radiated by the atoms, is sent to a beam splitter and coincidence counts are recorded as a function of the delay time. As in the down-conversion experiments, we can observe an increase in coincidence counts by a factor of 2 when the probe field overlaps with the field radiated by the atoms.

What is the origin of this increase in coincidence counts? Can it be traced to stimulated emission as is claimed in down-conversion experiments, or are there other mechanisms at play here? To help answer these questions, we prepare our atomic ensemble in two distinct fashions, one involving a single excitation (superatom or Dicke [28] state) and the other a factorized initial state. We are able to do this by choosing different Rydberg states in the excitation schemes. The results are analyzed using source-field theory [54]. In the case of the Dicke state preparation, there is a single excitation shared by N atoms and the incoming probe pulse can drive a stimulated transition between the Dicke state and the ground state. The coupling strength between the two collective states is enhanced by a factor $\sqrt{N}$. As a

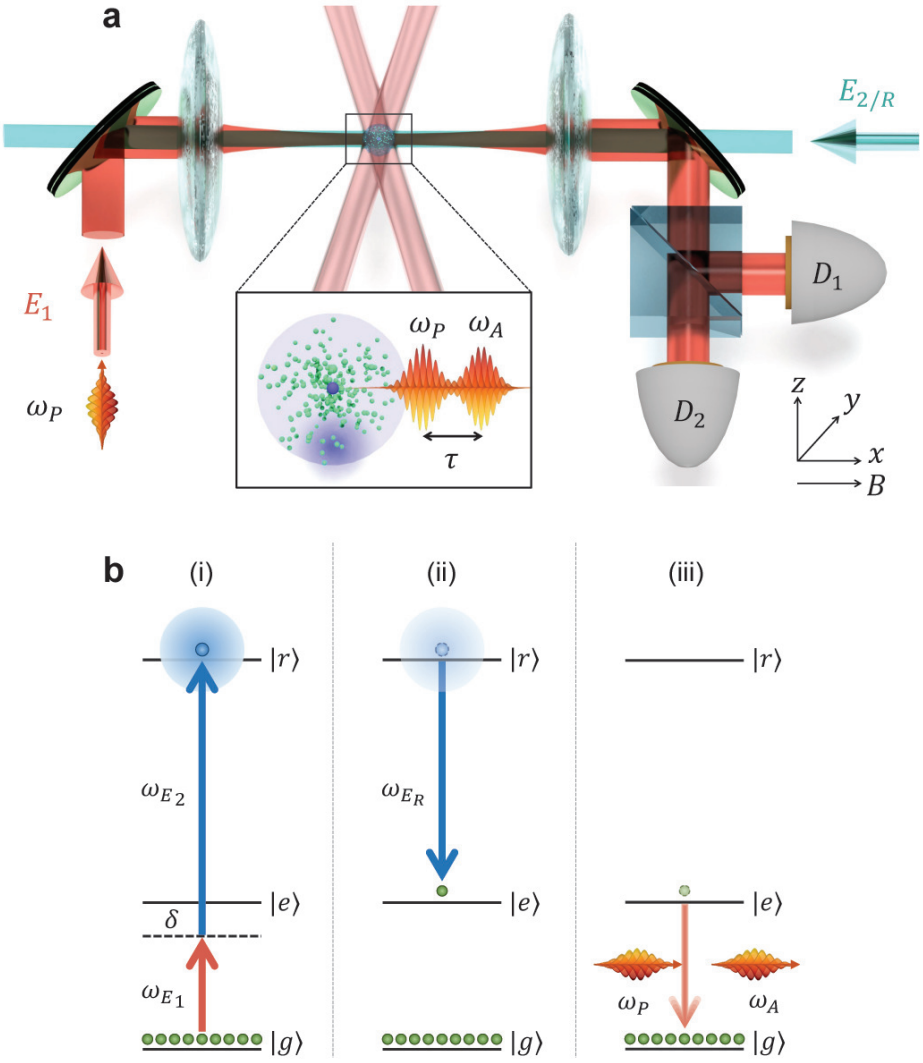

Figure 3.1: Outline of the experiment. a, Experimental setup: ultracold atomic gas is prepared in a crossed pair of focused YAG laser beams. A pair of lenses focuses E_1 and E_2 laser fields to drive a two-photon transition from the ground state $|g\rangle$ to the Rydberg state $|r\rangle$. A retrieval laser pulse E_R leads to emission of atomic field which is split on a beam-splitter and directed onto photodetectors D_1 and D_2. A probe laser field with controllable frequency and delay is aligned into the spatial mode of the atomic emission. **b,** Three main steps of the protocol: (i) an atomic ensemble is excited into a Rydberg atomic state $|r\rangle$; (ii) after a short delay, the atoms are driven into intermediate state $|e\rangle$, leading to emission on the $|e\rangle \leftrightarrow |g\rangle$ transition, with propagation direction determined by the phase-matching condition; (iii) an incoming probe field and atomic emission fields, with controllable delay between the two fields, are directed towards HBT measurement.

consequence, one might associate the increased coincidence counts with stimulated emission. On the other hand, for a factorized initial atomic state, such an interpretation is no longer tenable since the incident probe field is actually absorbed by the medium. In both cases however an increase in coincidence counts is observed. We present experimental results and a theoretical analysis that leads us to conclude that stimulated emission is *not* responsible for the increase in coincidence counts. Instead, the increase in coincidence counts can be attributed to Hanbury Brown and Twiss (HBT) interference [31], which we claim is also responsible for the increase in coincidence counts measured in the down-conversion experiments.

To illustrate the underlying physics, we consider first a single-photon probe pulse incident on a two-level atom (lower level g and excited level e) that is prepared in its excited state at time $t = 0$. The wave front of the probe pulse, which has cross-sectional area A greater than the pulse's central wavelength λ, arrives at the atom at time $\tau \geq 0$. In source-field theory [32], the positive frequency component of the field operator for this system can be written as $E_+(\mathbf{R}, t) = E_+^{(0)}(\mathbf{R}, t) + E_+^{(S)}(\mathbf{R}, t)$, where $E_+^{(0)}(\mathbf{R}, t)$ is the free-field operator and $E_+^{(S)}(\mathbf{R}, t)$ is the source field operator associated with the field radiated by the atoms in the sample. Two types of measurements can be envisioned. Either (1) the integrated field intensity is measured or (2) the time-integrated number of coincidence counts is recorded as a function of τ after the field is sent through a beam splitter. The detection volume is restricted to a small angle in the forward direction.

For $A \gg \lambda^2$, a "weak coupling" approximation can be made—the interaction between the atoms and the input pulse can be neglected to lowest order, owing to the fact that $\max\left[\Omega_p/\gamma_e \ll 1, \Omega_p T_p \ll 1\right]$, where Ω_p is the probe Rabi frequency, T_p is the probe pulse duration, and γ_e is the excited state decay rate. It is then rather easy to analyze the two measurement scenarios, which are sensitive to different physical processes. The total field can be viewed as a sum of the collimated input field, the spherical wave spontaneously emitted field from the atom, and the field scattered by the atom.

The integrated field intensity is sensitive to the *amplitudes* of the three contributions to the total field. Stimulated emission or absorption is associated with the interference of the scattered field with the (unperturbed) input field [55]. Whether stimulated emission or absorption occurs depends on both the spectral width of the input pulse and the time delay τ. In contrast, the time-integrated number of coincidence counts N_c is insensitive to the relative phase of the input and source fields—it depends only on field intensities. Moreover, in the weak coupling approximation, the scattered field has a negligible effect on the value of N_c. When measured as a function of τ, N_c exhibits a "bump" for $\tau = 0$ that can then be interpreted as HBT interference between the input field and the field spontaneously emitted from the atoms, in exact analogy with the HBT increase in the second order correlation function for two independent light sources. In other words, although both stimulated emission and HBT interference can both be described in terms of interference, they correspond to fundamentally different physical processes. The HBT coincidence count bump is *not* linked to stimulated emission—it occurs even if the input field is attenuated. Moreover, in the weak coupling approximation, any absorption or stimulated emission of the input pulse is negligibly small—the output field intensity is approximately equal to the sum of the input and atomic field intensities, considered as independent sources.

3.3 Superatom

The same formalism can be used to model our experiment involving phase-matched emission from an ensemble of atoms, Figure 3.1(b). The three-level atoms (ground state $|g\rangle = |5S_{1/2}, F = 2, m_F = 2\rangle$, intermediate state $|e\rangle = |5P_{3/2}, F = 3, m_F = 3\rangle$, and Rydberg state $|r\rangle = |nS_{1/2}, m_J = 1/2\rangle$) are prepared in a phase-matched superposition of ground and Rydberg states using an excitation pulse of duration $T_E = 1$ μs, consisting of two counter-propagating laser pulses E_1 and E_2 having central wavelengths 780 nm and 480 nm, respectively. Field E_1 drives the $|g\rangle \leftrightarrow |e\rangle$ transition with Rabi frequency Ω_1 and field E_2

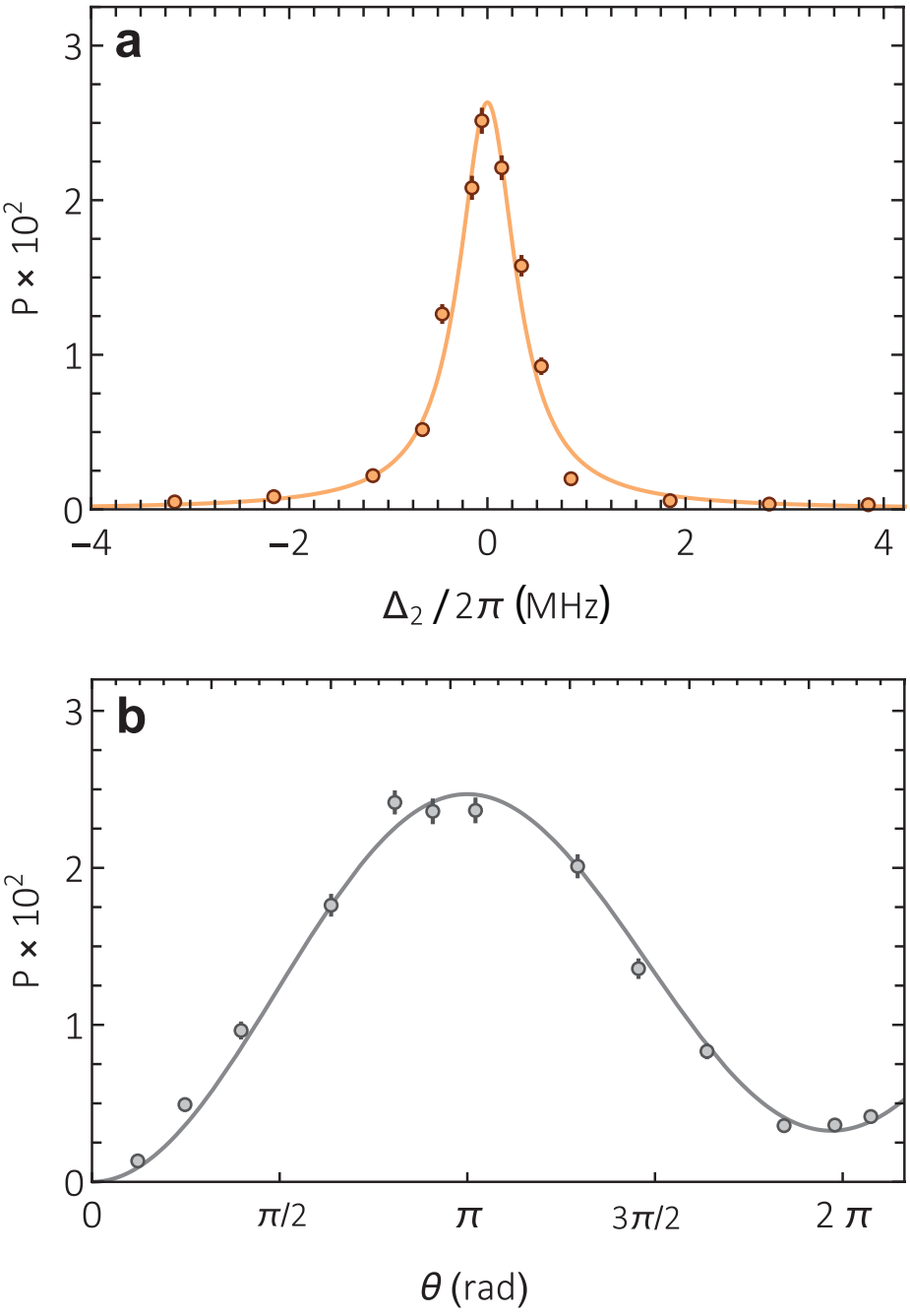

Figure 3.2: Probing a collective (super-atom) state. **a**, Probability of photoelectric detection event per trial P as a function of two-photon detuning $\Delta_2 = \omega_{rg} - (\omega_{E_1} + \omega_{E_2})$ for the Rydberg state $|r\rangle = |87S_{1/2}\rangle$. The solid curve is a Lorentzian fit. The 0.8 MHz (FWHM) width of the peak is determined by the 1 μs excitation pulse duration; **b**, P as a function of the collective Rabi angle θ displaying a period of a many-body (super-atom) Rabi oscillation. Solid curve is a theory curve for a collective Rabi oscillation with $\Omega_2/2\pi = 1.5$ MHz and $\Omega_1/2\pi$ varied between 2 and 20 MHz. The best fit between theory and the data occurs for the number of atoms $N = 234$.

drives the $|e\rangle \leftrightarrow |r\rangle$ transition with Rabi frequency Ω_2. Field E_1 is detuned by an amount $\delta = -2\pi \times 90$ MHz from ω_{eg}. For a high-n Rydberg state [56], excitation of more than one atom into the Rydberg state can be suppressed, with the atomic ensemble being coherently driven between the collective ground state $|G\rangle$ and a singly-excited (so-called superatom) collective state $|R\rangle$ at a frequency $\Omega_N = \sqrt{N}\Omega_1\Omega_2/(2\delta)$ [57, 58, 14, 59, 61, 60]. After a delay $T_s \approx 0.5$ μs following the excitation pulse, a readout pulse E_R, centered at 480 nm is applied that is resonant with the $|r\rangle \leftrightarrow |e\rangle$ transition frequency and leads to phase-matched emission with $\omega_A = \omega_{eg}$.

Figure 3.2(a) displays the probability of photoelectric detection P as a function of two-photon detuning Δ_2 between $(\omega_{E_1} + \omega_{E_2})$ and ω_{rg}. The maximum probability of a photoelectric detection per trial is $P_{max} \approx 2.5 \times 10^{-2}$ for a chosen value of $\theta \equiv \Omega_N T_E \simeq \pi$. Figure 3.2(b) shows P as a function of θ. Accounting for a factor of $\zeta = 0.27$ transmission and detection efficiency, there is a maximum probability $p_f \approx 0.09$ for a single photon to be emitted into the spatial mode defined by the single-mode fiber used for collection. A probe pulse whose temporal profile matches that of the phase-matched emission and whose spatial mode corresponds to the detector acceptance mode, is also sent into the medium. In the absence of any Rydberg excitation, the transmission coefficient for the probe pulse is 0.45 ± 0.01. Figure 3.3 shows measured intensity profiles (normalized photo-counts $\widetilde{M}$ vs time t) for the probe pulse and the phase-matched atomic emission. The profiles are matched by adjusting both the readout and probe pulses, with their overlap integral being 0.94 for a 0.5 μs integration window and greater than 0.98 for a 0.1 μs integration window centered on their peak values. The value of the time-integrated second-order correlation function for atomic emission in the absence of the probe pulse is $g_A^{(2)} = 0.04$. The probe pulse can be delayed by a time τ relative to the phase-matched emission and the probe frequency ω_P can be detuned by an amount Δ from ω_A.

The total output field is sent into a beam splitter and detectors in the output mode of the beam splitter record coincidence counts. In the weak coupling approximation, any

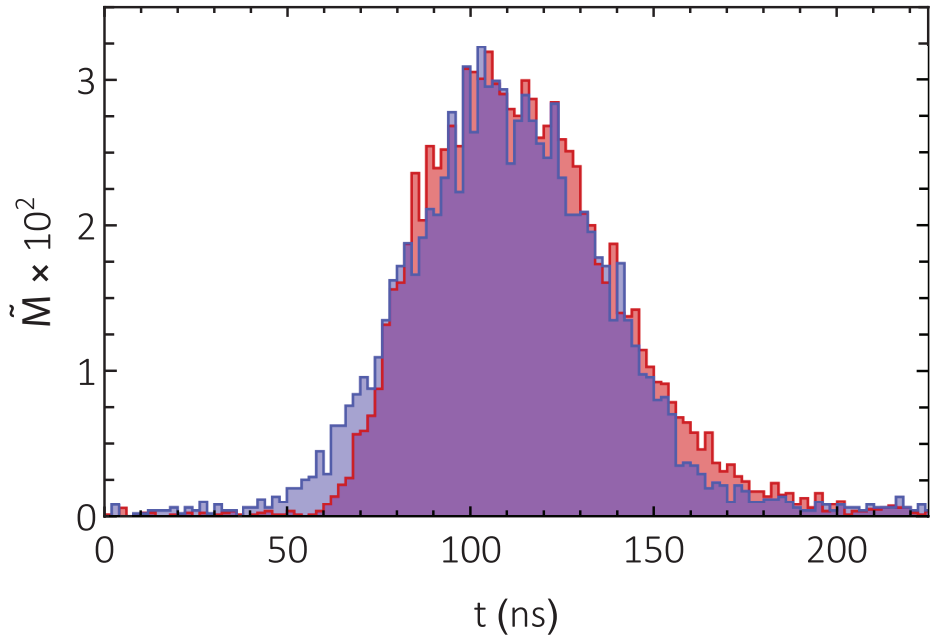

Figure 3.3: Temporal intensity profiles for the probe pulse (red) and the atomic emission (blue).

contribution to coincidence counts due to stimulated emission constitutes a small effect, of order $1/\left(Nk_0^2A\right) \simeq 10^{-6}$, where $k_0 = \omega_{21}/c$ and A is the cross-sectional area of the probe pulse. In fact, instead of being amplified by the medium, the output field intensity in the presence of Rydberg excitation is actually decreased by $\simeq 10^{-2}$.

3.4 Experimental setup

Our experimental system consists of two connected glass cells. In the first cell, a background-loaded, two-dimensional magneto-optical trap (MOT) of ^{87}Rb atoms directs a cold atomic beam into a high vacuum glass cell, feeding a three-dimensional MOT for a period of 1.2 s. This MOT loads an optical dipole trap formed by two orthogonally polarized YAG laser beams intersecting at an angle of $27°$. The dipole trap beams have a total power of 5 W and transverse waists of 16 μm and 34 μm for a maximum trap depth of $\simeq 0.5$ mK. The atomic cloud of $\simeq 9$ μm radius has temperature $T \sim 60$ μK and density $\rho \simeq 4 \times 10^{11}$

cm^{-3}. The level scheme is described in the main text. The ground state is denoted by $|g\rangle = |5S_{1/2}, F = 2, m_F = 2\rangle$, the intermediate state by $|e\rangle = |5P_{3/2}, F = 3, m_F = 3\rangle$, and the Rydberg state by $|r\rangle = |nS_{1/2}, m_J = 1/2\rangle$.

A bias magnetic field of 5.5 G is switched on and atoms are optically pumped to the $|g\rangle$ state. The excitation pulse consists of a pair of counter-propagating fields denoted by E_1 and E_2, respectively. Field E_1 has central wavelength 780 nm and is σ^+ polarized while field E_2 has central wavelength 480 nm and is σ^- polarized. In Fig. 3.4, the timing sequence for the 480 nm and 780 nm fields is shown. The excitation fields create a spin wave between the $|g\rangle$ and $|r\rangle$ states. Field E_2 is detuned from ω_{eg} by $\delta_1/2\pi = 90$ MHz. The 780 nm light is derived from an extended cavity diode laser (ECDL). Light at 480 nm is produced by frequency-doubling of an amplified output of a 960 nm ECDL. Both of the ECDLs are frequency-locked to a thermally stabilized ultra-low expansion glass cavity. The sum of the frequencies of the E_1 and E_2 fields are tuned to be in resonance with the $|g\rangle \leftrightarrow |r\rangle$ ground to Rydberg state transition. The spin wave is stored for a period $T_s \simeq 0.5$ μs.

After storage time T_s the atoms are coherently driven on the $|r\rangle \leftrightarrow |e\rangle$ transition by a (σ^+-polarized) retrieval field E_R, creating an array of atomic dipoles which give rise to a phase-matched emission on the $|e\rangle \leftrightarrow |g\rangle$ transition. The E_1, E_2, and E_R fields are focused onto the atoms with beam waists $w_1 \approx 6$ μm and $w_2 = w_R \approx 15$ μm and Rabi frequencies $\Omega_1/2\pi \simeq 5$ MHz, $\Omega_2/2\pi \simeq 1.5$ MHz, and $\Omega_R/2\pi \simeq 6$ MHz, respectively. The ~ 36 μm length of the atomic cloud in the longitudinal dimension and the ~ 6 μm waist of the 780 nm excitation field mode determines the ($z-$) and the radial dimensions of the ensemble, respectively. The emitted light is collected into a single-mode optical fiber coupled to a single-photon detector. The retrieved field is split by a beam-splitter, with the two outputs coupled into single mode fibers followed by single-photon detectors $D_{1,2}$. To avoid damaging the detectors by the Ω_1 field, a gating acousto-optical modulator is used. The 6 μs long experimental sequence is repeated 10,000 times for each sample preparation, with a 3 μs optical pumping period inserted every five cycles. One trap loading and experimental

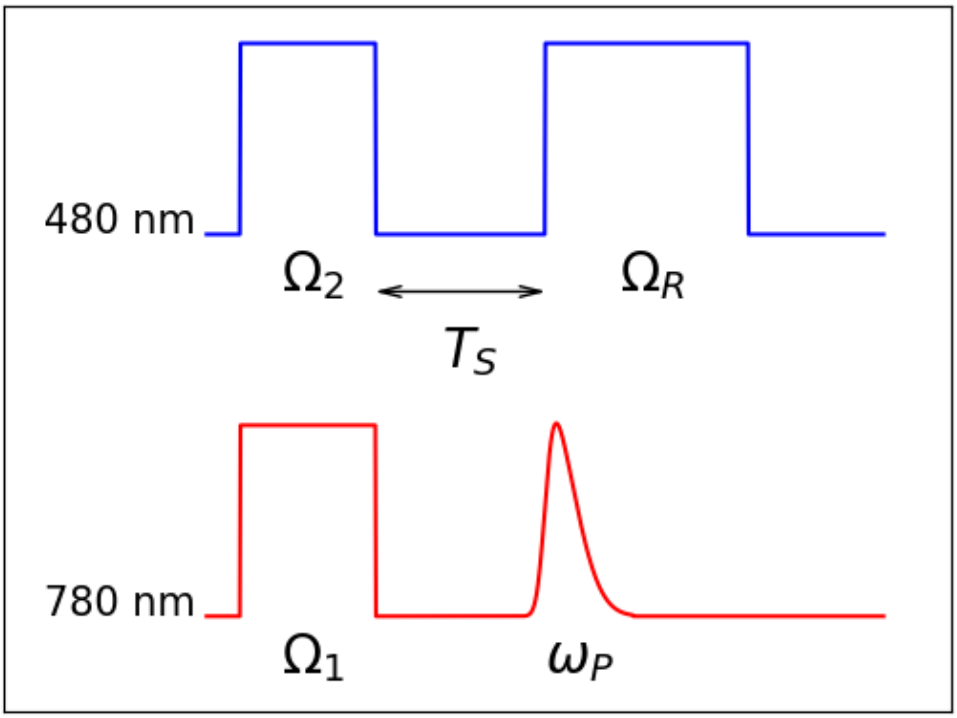

Figure 3.4: Timing sequence of laser fields in the experimental protocol.

sequence cycle takes 1.9 s. To avoid dephasing the Rydberg-ground coherence by the differential optical trapping potential, the dipole trap is turned off for a 1.5 μs period within which the atomic excitation sequence is performed.

Every experimental trial data acquisition is triggered and photoelectric events on detectors D_1 and D_2 are recorded within gated time intervals. In each experimental trial, photoelectric events from detectors D_1 and D_2 are recorded within a time interval varying between 100 ns and 300 ns. The photoelectric detection probability for both detectors is given by $P = P_1 + P_2 = N_1/N_0 + N_2/N_0$, where $N_{1,2}$ are the events recorded by D_1 and D_2 and N_0 is the number of experimental trials. The probability for detecting coincidences is given by $P_{12}(\tau) = N_{12}(\tau)/N_0$, where $N_{12}(\tau)$ is the number of coincidences from the two detectors with time delay τ. When no probe light is used, the probability of photoelectric detection P is proportional to the single excitation preparation efficiency ξ: $P = \eta_r \zeta \xi$. η_r is the efficiency of converting excitation in $|b\rangle$ into mode-matched photon field. The photon transmission

and detection efficiency ζ is given by $\zeta = \eta_a\eta_f\eta_d = 0.27$, where $\eta_a = 0.68$, $\eta_f = 0.72$ and $\eta_d = 0.55$ are AOM diffraction efficiency, fiber coupling efficiency and single photon detection efficiency, respectively.

3.5 Dicke state

The probe pulse is a weak, coherent state pulse having energy less than or of order $\hbar\omega_{eg}$. The atoms are prepared either into (1) a state consisting of a single phase-matched excitation by choosing an upper atomic state $|r\rangle = |87S_{1/2}\rangle$ with strong interactions [13, 62, 63], or (2) an upper atomic state $|r\rangle = |50S_{1/2}\rangle$, which leads to a factorized atomic state having on average $N_r \approx 1.5$ Rydberg excitations in the sample. In case (1), assuming that the spatial profiles of the probe and phase-matched emission pulses are identical, the number of photo-counts separated in time by t_{21} is given by

$$N_c(t_{21}) = \int_{-\infty}^{\infty} dt\, \widetilde{I}(t)\widetilde{I}(t+t_{21})\left[1 + V_1(K)\cos\left(\Delta t_{21}\right)\right], \tag{3.1}$$

where $\widetilde{I}(t)$ is proportional to the intensity profile of the probe field, K is the ratio of integrated intensities for the input probe pulse and phase-matched emission, and $V_1(K) = 2K/(K^2 + 2K + g_A^{(2)})$ is the fringe visibility, allowing for a nonzero value of $g_A^{(2)}$. As was the case for a two-level atom, Eq. (3.1) is derived assuming that atom-field interactions are negligibly small, that is, no effects related to stimulated emission are included. In Figure 3.5(a), we plot measured values of $N_c(t_{21})$ for $K = 0.21$. The theory curve is obtained assuming a Gaussian profile for $\widetilde{I}(t)$ and an expected value of $V_1(0.21) = 0.83$.

The normalized time-integrated coincidence counts are given by

$$N_c = 1 + 2K|J|^2/[K^2 + 2K + g_A^{(2)}], \tag{3.2}$$

where $J \equiv \int_{-\infty}^{\infty} e^{-i\Delta t} S(t-\tau)f(t)dt$ is the overlap integral of the two fields, $S(t)$ and $f(t)$ are the (real) scaled amplitudes of the phase-matched field and the probe pulse, respectively, normalized such that $\int_{-\infty}^{\infty} dt\, S^2(t) = 1$, $\int_{-\infty}^{\infty} dt\, f^2(t) = 1$. In this case we allow for a slight

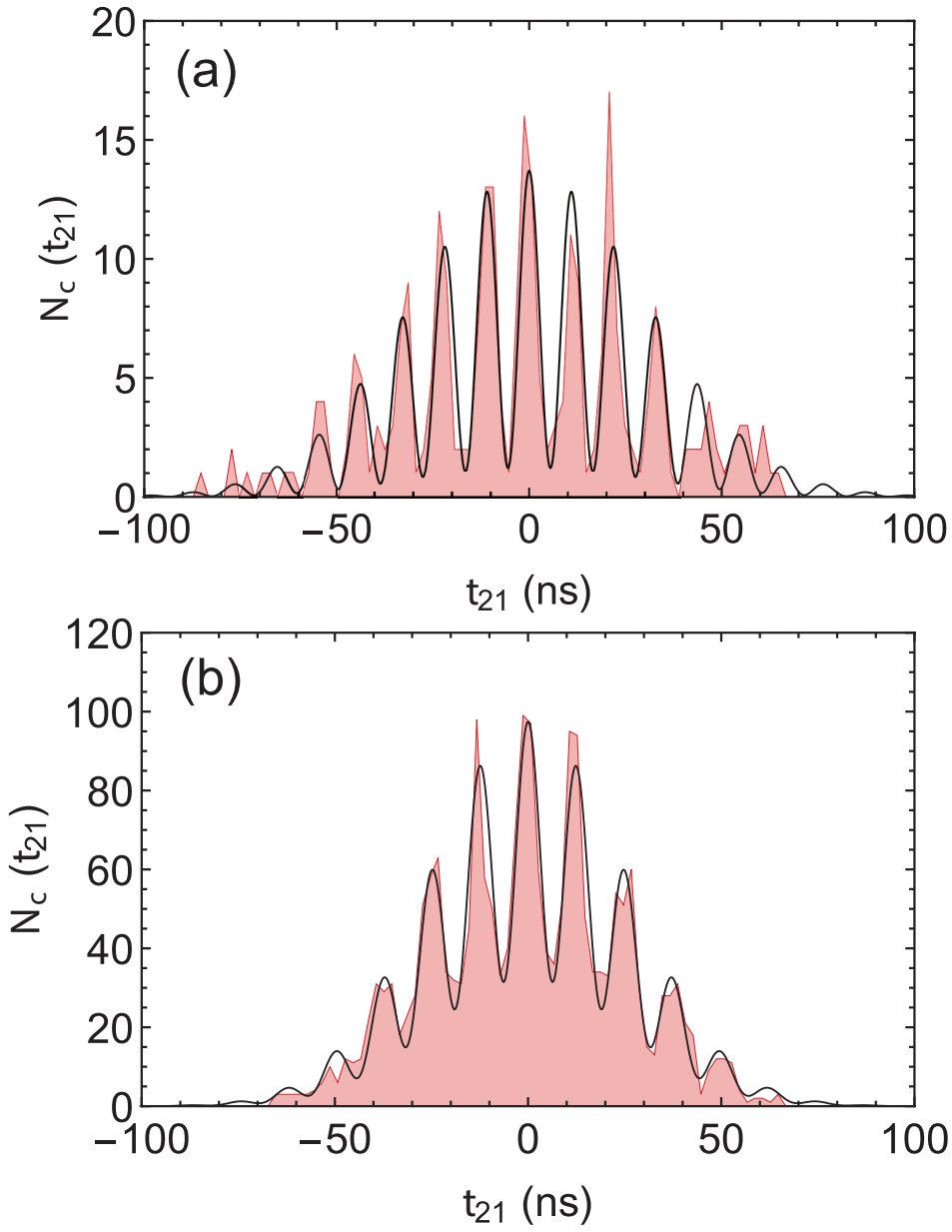

Figure 3.5: Two-photon statistics for the upper atomic state a, $|r\rangle = |87S_{1/2}\rangle$ and b, $|r\rangle = |50S_{1/2}\rangle$. Coincidences in 2 ns as a function of detection-time delay t_{21} for detuning $\Delta/2\pi = -80$ MHz between the probe field and the field emitted by the atoms. Solid curves in **a** and **b** are obtained from theory described in the text and the supplemental material of reference [46].

difference between the intensity profiles of the probe field and atomic emission. If the intensity envelopes are identical and if $K \ll 1$ and $g_A^{(2)} \ll 1$, the time-integrated coincidence counts are doubled provided $\Delta = 0$ and $\tau = 0$, from the case where $|\Delta| / \gamma_e \gg 1$ or $\gamma_e \tau \gg 1$.

In Fig. 3.6(a), N_c is plotted as a function of Δ for $\tau = 0$ and N_c is plotted as a function of τ for $\Delta = 0$ in Fig. 3.7(a). The Equation (3.2) is strictly valid only under an assumption of an optically thin medium in which the fraction of energy radiated by the atoms in the phase-matched direction $p_f \ll 1$. Including corrections of order $p_f \approx 0.06$ we estimate the value of $N_c \simeq 1 + 2(1 - p_f)K|J|^2/(K^2 + 2K + g_A^{(2)})$. In Figs. 3.6(a) and 3.7(a), the theoretical curves are drawn using $\{K = 0.46, |J(\Delta = 0)|^2 = 0.98\}$ [$N_c(\Delta = 0) = 1.72$] and $\{K = 0.35, |J(\tau = 0)|^2 = 0.94\}$ [$N_c(\tau = 0) = 1.72$], respectively.

When a Rydberg blockade is operative, the problem can be reduced to an effective two-level problem involving transitions between the Dicke state and the ground state. As such, it is possible to envision a situation in which there is total inversion of the system. Although the probe field can produce stimulated emission on the inverted system, the observed factor of two increase in coincidence counts is *not* a consequence of stimulated emission. Rather, it is an indication of both the nonclassical nature of the atomic Dicke state and HBT interference.

3.6 Factorized state

As further evidence of the fact that the increase in coincidence counts results from HBT interference and not stimulated emission, we next consider a factorized initial atomic state for which $g^{(2)} = 1$ and there is no inversion. Assuming that there is no temporal coherence between the input pulse and the phase-matched emission and that $f(t) = S(t)$, $N_c(t_{21})$ is given by

$$N_c(t_{21}) = \int_{-\infty}^{\infty} dt\, \widetilde{I}(t)\widetilde{I}(t + t_{21})\left[1 + V_2(K)\cos\left(\Delta t_{21}\right)\right],$$

where $V_2(K) = 2K/(1 + K)^2$ is the fringe visibility. In Figure 3.5(b), we plot values of $N_c(t_{21})$ for the Rydberg state $|r\rangle = |50S_{1/2}\rangle$ and with $K = 0.98$. The solid curve is theory,

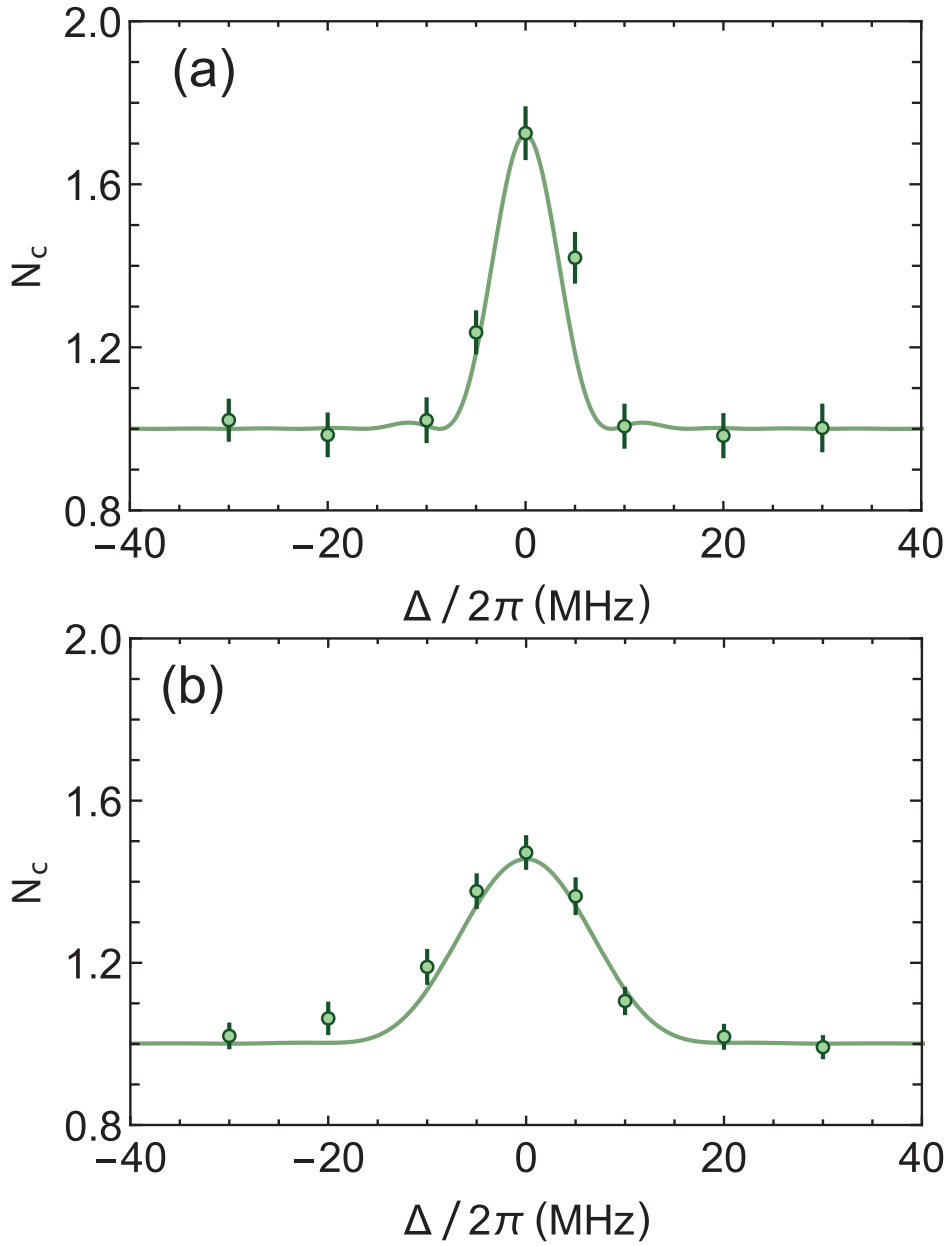

Figure 3.6: Two-photon statistics for the upper atomic state a, $|r\rangle = |87S_{1/2}\rangle$ and b, $|r\rangle = |50S_{1/2}\rangle$. Normalized coincidences as a function of the detuning Δ between the probe pulse and the pulse from the ensemble. Solid curves in **a** and **b** are obtained from theory described in the text and the supplemental material of reference [46].

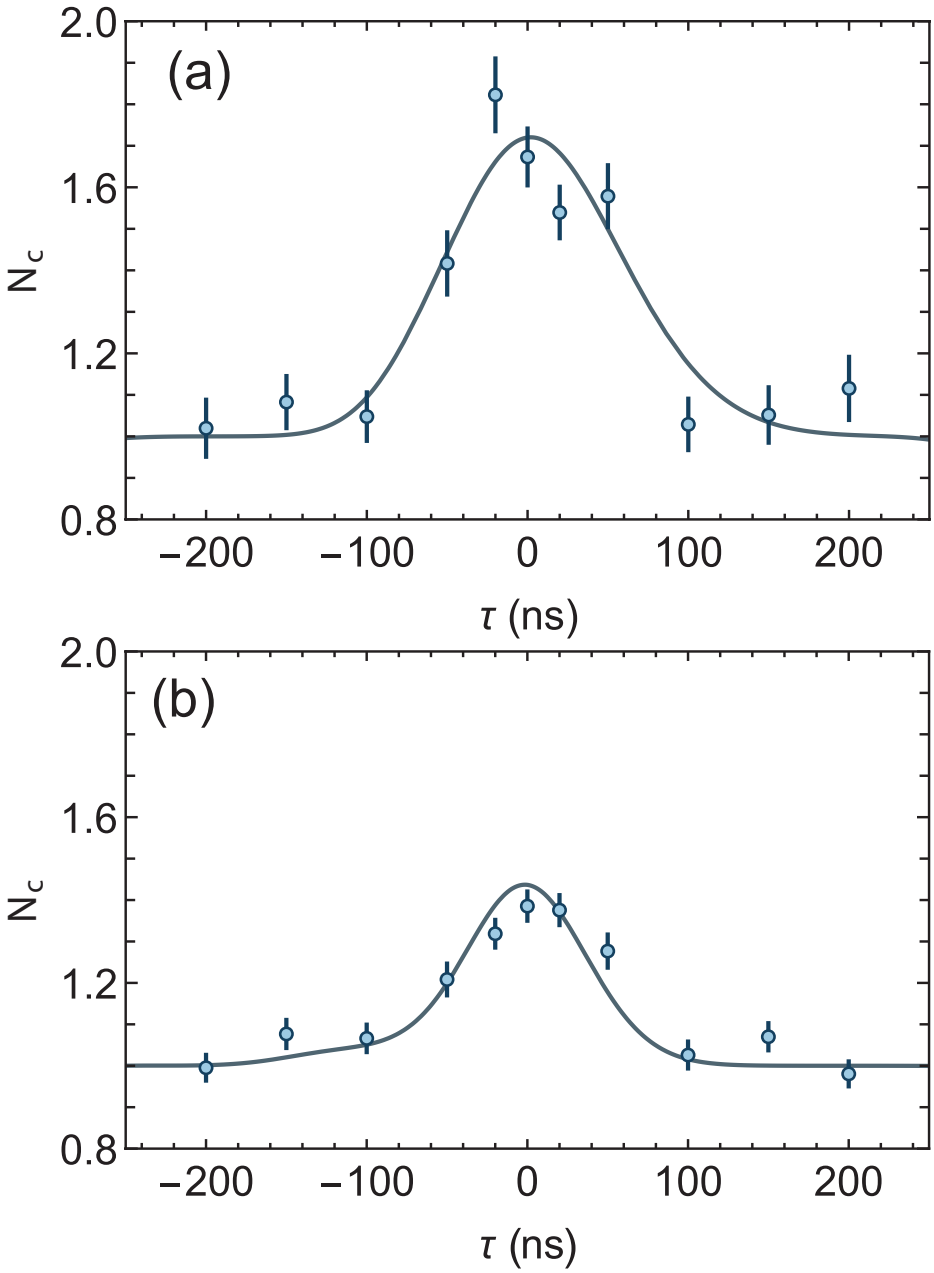

Figure 3.7: Two-photon statistics for the upper atomic state a, $|r\rangle = |87S_{1/2}\rangle$ and b, $|r\rangle = |50S_{1/2}\rangle$. Normalized coincidences as a function of the delay τ between the probe pulse and the pulse from the ensemble. Solid curves in **a** and **b** are obtained from theory described in the text and the supplemental material of reference [46].

with fringe visibility $V_2(0.98) \approx 0.50$. The fringe visibility of 1/2 is consistent with HBT interference between two coherent-state pulses, a situation that is mirrored by our choice of a factorized atomic state and a coherent-state probe pulse. For $K = 1$, the normalized time-integrated coincidence counts are given by $N_c = 1 + \frac{1}{2}|J|^2$. It is seen that in this case, for $f(t) = S(t)$, the time-integrated coincidence rates are increased by a factor of $3/2$ provided $\Delta = 0$ and $\tau = 0$, from the case where $|\Delta|/\gamma_e \gg 1$ or $\gamma_e \tau \gg 1$. Figures 3.6(b) and 3.7(b) show N_c as a function of pulse detuning and delay respectively, together with theory curves for which the enhancement factor $N_c \simeq 1 + 2(1 - p_f)|J|^2 K/(1 + K)^2$. In Figs. 3.6(b) and 3.7(b), the theoretical curves are drawn using $\{K = 0.90, |J(\Delta = 0)|^2 = 0.97\}$ $[N_c(\Delta = 0) = 1.46]$ and $\{K = 1.00, |J(\tau = 0)|^2 = 0.93\}$ $[N_c(\tau = 0) = 1.44]$, respectively. Again, although stimulated emission is absent, there is an enhancement in coincidence counts when the probe pulse overlaps with the phase-matched atomic emission.

3.7 Conclusion

In conclusion, the interaction between the incident probe field with the atoms in experiments such as ours and in Refs. [52, 48, 49, 50, 51, 53] can be treated in a weak coupling approximation. In that limit the increase in coincidence counts can be fully described by HBT-type interference between the incident field and the field radiated by the medium. There is no direct connection with stimulated emission.

Chapter 4

Long-lived coherence between ground and Rydberg levels in a magic-wavelength lattice

This chapter is based on Ref. [64]

4.1 Introduction

Ground-state–Rydberg-state coherence in ensembles of ultra-cold atoms plays a critical role in many quantum information, quantum communication, and precision metrology protocols [56, 12, 65, 66, 67, 68, 69, 70]. Single-photon generation [13], photon anti-bunching [62], many-body Rabi oscillations [14], creation of entanglement of light and atomic excitations [63], single-photon optical switches and interaction-induced phase shifts [71, 72, 73, 74, 75] have been demonstrated based on coupling of ensembles of neutral atoms with propagating quantum light fields. Significant progress has also been made in employing Rydberg interactions for entanglement [59, 60, 76], many-body interferometry [77], and quantum simulation in arrays of neutral atoms [78]. All these experiments have relied on quantum coherence between the ground and Rydberg states. Prolonging this coherence lifetime is therefore

crucial to further advances in increasing the size and complexity of quantum algorithms and the precision of atomic measurements.

Several physical processes contribute to ground-state–Rydberg decoherence, including spontaneous decay, black-body radiation, and coupling to stray electric fields [56]. In the majority of experiments to date, however, the loss of coherence can be attributed mainly to motional dephasing, limiting the coherence lifetime to a few microseconds [13, 14, 59, 60, 76, 78]. Motional dephasing can be reduced by tightly confining the atoms in an optical dipole trap. Unfortunately, while typical off-resonant dipole traps are attractive for ground state atoms, they are repulsive for atoms in Rydberg levels. This results in fast decoherence owing to position-dependent differential energy shifts, making it necessary to turn off the trapping fields for the duration of the Rydberg excitation period. To overcome this problem, the trapping fields can be tuned to a so-called “magic" wavelength [29, 30] that results in identical energy shifts for the ground and Rydberg state [63, 79]. The magic wavelength is close to that of the Rydberg level $|ns_{1/2}\rangle$ - intermediate level $|6p\rangle$ transition.

In this work we exploit the use of the magic wavelength to obtain a significant enhancement of ground-state–Rydberg atomic coherence lifetimes over a range of principal quantum numbers $n = 30 \ldots 70$. This is achieved by confining the atomic sample in a one-dimensional, state-insensitive optical lattice along the axis of propagation of the excitation light fields. We observe damped oscillations of the collective ground-state–Rydberg atomic coherence in the lattice potential. The anharmonicity of the potential leads to a damping of the visibility of the oscillations, whereas the radiative decay and black-body radiation-driven depopulation of the Rydberg state lead to a damping of the overall signal.

A second component of this paper is the formulation of a theory that can be used to explain the overall features of the experimental data. A first principles calculation of the signal presents considerable challenges, even when interactions between Rydberg atoms can be neglected. The reason for this is that standard methods [32] involving the use of the Maxwell-Bloch equations or a source-field approach are no longer applicable when the

atoms undergo quantized motion in the trap potentials. Moreover, if the trap potentials differ for the Rydberg and ground state potentials, any approach assuming classical motion in the potentials fails if the signal depends on the coherence between these levels. There *have* been theories of phased-matched emission from trapped atoms that have been developed in the context of atom interferometry [82], but the formalisms used in those approaches differ somewhat from what is needed in our problem involving excitation of Rydberg levels. More closely related to our calculations are those of Zhao *et al.* [83] and Jenkins *et al.* [84] who considered phase-matched emission from trapped atoms using Raman transitions. Jenkins *et al.* [84] used a model in which the atoms undergo classical motion in a lattice potential. In contrast to these authors, we present a theory that treats the atomic motion in the lattice quantum-mechanically and allows for different Rydberg and ground state potentials. We first present a theoretical formalism that can be used to model our system and then describe its experimental implementation.

4.2 Theory

A full theoretical description of retrieved signal from an ensemble in a state-insensitive optical lattice can be found in the reference [64]. It explains the three parts of the retrieved signal: the optical potentials of the ground and Rydberg states, the contribution to the signal from a single atom, and the weighted sums over the distribution of atoms. In this section, I will briefly overview the optical potentials for the ground and Rydberg states to qualitatively explain why the so-called non-lattice contribution is important for coherence time. Then I will state the final equations used to model the signal from the atoms and examine how experimental parameters such as trap depth and atomic sample length affect the coherence time of the ensemble.

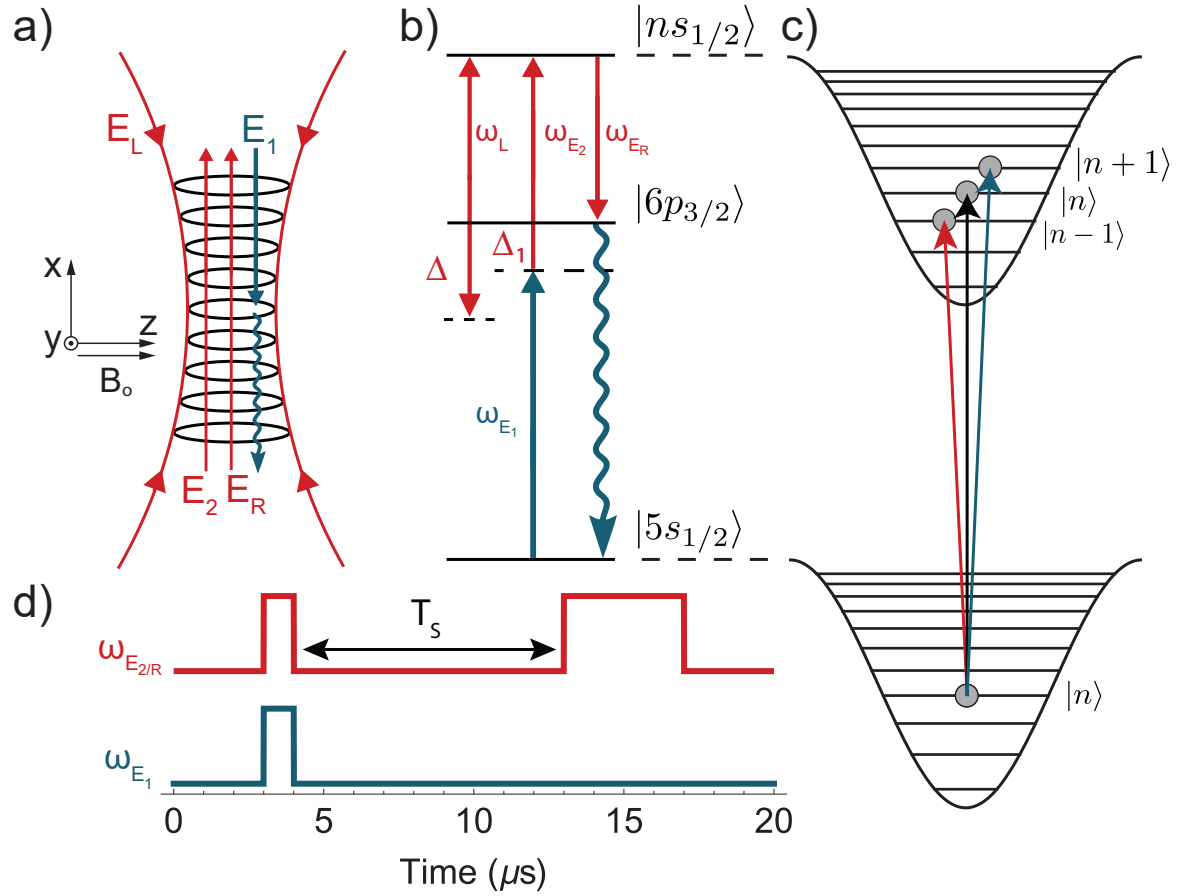

Figure 4.1: (a) A cold sample of ^{87}Rb gas is trapped in a 0.5-μm-period one-dimensional optical lattice formed by a retro-reflected beam E_L. Two nearly counter-propagating beams, E_1 and E_2 excite a spin wave between the $|5s_{1/2}, F = 2\rangle$ and $|ns_{1/2}\rangle$ levels. After a storage time, T_s, a retrieval pulse, E_R, is applied, creating an array of atomic dipoles which give rise to a phase-matched emission from the sample. The actual geometry used in the experiment differs somewhat from that shown schematically in the figure. b) Relevant ^{87}Rb energy levels and corresponding fields, with $\Delta = \omega_L - \omega_{ns,6p_{3/2}}$ and $\Delta_1 = \omega_{E_2} - \omega_{ns,6p_{3/2}}$. c) Schematic diagram indicating transitions between the ground and excited state motional levels. d) Timing diagram showing the excitation and retrieval pulse sequence.

4.2.1 Optical potentials

As depicted in Figure 4.1(a) the ensemble is held in an optical lattice. The levels we are concerned with, $|5s_{1/2}\rangle$ and $|ns_{1/2}\rangle$, are shown in Figure 4.1(b) with the excitation and retrieval frequencies (ω_{E_1}, ω_{E_2}, and ω_{E_R}), and the lattice frequency ω_L. ω_L is near-resonant with the intermediate state $|6p_{3/2}\rangle$ such that it shifts both the ground state and the Rydberg state nearly equally as depicted in Figure 4.1(c). The general electric field amplitude for the y-polarized trap can be described as,

$$\begin{aligned} E(\mathbf{R},t) &= \frac{1}{4}\left[A_+(\rho,X)e^{ik_LX} + A_-(\rho,X)e^{-ik_LX}\right]e^{-i\omega_Lt} \\ &\quad +\text{c.c.}, \end{aligned} \tag{4.1}$$

where

$$A_\pm(\rho,X) = E_{\pm,0}\frac{w_{\pm,0}}{w_\pm(X)}e^{-\rho^2/w_\pm^2(X)}, \tag{4.2}$$

ρ is the radial coordinate (the axial coordinate being X), $E_{\pm,0}$ are the field amplitudes for the incident ($+$) and retro-reflected ($-$) fields, k_L is the wave number of the lattice $k_L = 2\pi/\lambda_L$, $w_{\pm,0}$ are the waist radii of these fields, and

$$w_\pm(X) = w_{\pm,0}\sqrt{1+\frac{(X-X_{\pm,0})^2}{X_{\pm,r}^2}}, \tag{4.3}$$

where $X_{\pm,0}$ are the foci positions for the incident and retro-reflected beams, and $X_{\pm,r}$ is the Rayleigh lengths for the incident and retro-reflected beams. An explanation of the lattice geometry is in Chapter 2.

By calculating the time-averaged intensity and multiplying by the ground state polarizability α_g the ground state potential can be calculated using the dipole approximation,

$$U_g = -\frac{1}{16}\alpha_g\left[4A_+A_-\cos^2(k_LX) + (A_+ - A_-)^2\right], \tag{4.4}$$

In this equation, the term $4A_+A_-\cos^2(k_LX)$ is referred to as the lattice potential because it depends on the position of the atom X in the lattice. The term $(A_+ - A_-)^2$ is the non-lattice potential and is independent of X. This calculation can be performed for the Rydberg state as well, however, it is more complicated due to the break down of the dipole approximation. For a full explanation see reference [64]. It is sufficient to say the result will have a lattice potential and a non-lattice potential as well. However, for the Rydberg level the polarizability depends on the detuning of the lattice from the $|6p_{3/2}\rangle \leftrightarrow |ns_{1/2}\rangle$ transition. By careful choice of lattice detuning the lattice potentials for the ground and Rydberg states can be matched. The two states have the same spatial variation under the condition

$$\frac{D_n^2}{6\hbar\Delta_{m,n}} = \alpha_g + |\alpha_f|\,\theta_n, \tag{4.5}$$

where

$$\theta_n = \langle\cos(2k_Lx)\rangle_{ns} \tag{4.6}$$

this is from the Rydberg atom averaging over the lattice when the dipole approximation breaks down. $\Delta_{m,n}$ is the magic detuning for the ns Rydberg level, $\alpha_f = -e^2/m\omega_L^2$ is the free electron polarizability, and D_n is the reduced dipole matrix elements

$$D_n = \left|\langle ns||\hat{d}||6p_{3/2}\rangle\right|. \tag{4.7}$$

Equation 4.5 is used to calculate the dipole matrix elements after measuring $\Delta_{m,n}$.

However, while the lattice potential is matched for the ground and Rydberg states, the non-lattice potential cannot be fully compensated at every point in the trap. The differential shift resulting from the non-lattice potential is found in Ref. [64] to be

$$U_d^{(nl)}(\rho,X) = \hbar\omega_d(\rho,X) = \frac{|\alpha_f|\,U_0}{2\alpha_g}(1-\theta_n)\,\mathcal{I}(\rho,X), \tag{4.8}$$

where

$$\mathcal{I}(\rho, X) = \frac{w_+(0)w_-(0)}{2} \times \left[\sqrt{\frac{1}{\xi}}\frac{e^{-2\rho^2/w_+^2(X)}}{w_+^2(X)} + \sqrt{\xi}\frac{e^{-2\rho^2/w_-^2(X)}}{w_-^2(X)}\right] \tag{4.9}$$

ξ is the ratio between the incident and reflected power and

$$U_0 = \frac{1}{4}\alpha_g \frac{16c\mu_0 P}{\pi}\frac{1}{w_+(0)w_-(0)}. \tag{4.10}$$

$X = 0$ denotes the position of the atomic cloud center and P is the optical power of the lattice.

As will be seen later in this chapter, decoherence due to this mismatch will be the limiting factor at high principal quantum numbers. The spatial variation in the non-lattice potential is described by $\mathcal{I}(\rho, X)$ which leads to the mismatch decreasing the coherence time. Therefore, to maximize coherence time, the geometry of the trap must be carefully chosen to make $\mathcal{I}(\rho, X)$ have as little variation over the ensemble as possible.

4.2.2 Lattice contribution

The final expression can be separated into three parts: the lattice contribution, the non-lattice contribution, and three dissipative mechanisms as shown in reference [64].

The lattice contribution to the signal can be written as

$$G_l(T_s) = \left| \begin{array}{c} \sum_{q,q',q''}^{q_{\max}} \rho_{1q'',1q'}(0) M_{1q';3q}\left(-k\mathbf{u}_x\right) \\ \times M_{3q;1q''}\left(k\mathbf{u}_x\right) e^{i\left(\omega_{q'}^{(1)} - \omega_q^{(3)}\right)T_s} \end{array} \right|^2, \tag{4.11}$$

where,

$$\begin{aligned} M_{3q;1q'}^{(j)}(\mathbf{k}) &= \int dX_j \left[\psi_{3q}\left(X_j\right)\right]^* e^{i\mathbf{k}\cdot\mathbf{R}_j}\psi_{1q'}\left(X_j\right) \\ &= \left[M_{1q';3q}(-\mathbf{k})\right]^*, \end{aligned} \tag{4.12}$$

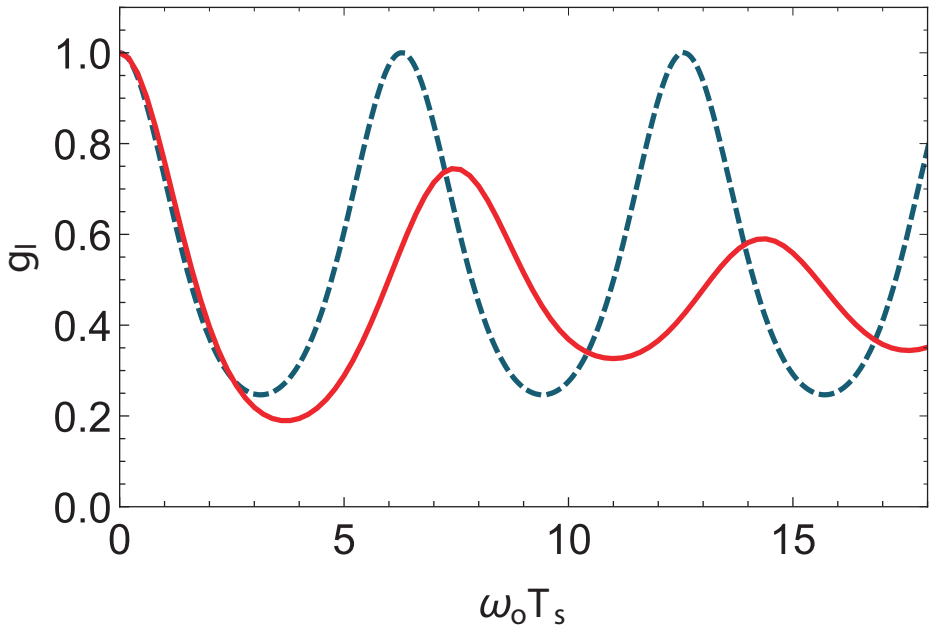

Figure 4.2: Graphs of $g_l(T_s)$ as a function of $\omega_0 T_s$: red, solid curve - $\cos^2(k_L X)$ potential; blue, dashed curve - harmonic potential.

$$\rho_{1q,1q'}(0) = \frac{\exp\left[-\frac{\hbar\omega_q^{(1)}}{k_B T}\right]\delta_{q,q'}}{\sum_{q=0}^{q_{\max}} \exp\left[-\frac{\hbar\omega_q^{(1)}}{k_B T}\right]}, \tag{4.13}$$

where $\delta_{q,q'}$ is a Kronecker delta. The $\omega_q^{(1)}$ are obtained by solving the appropriate Mathieu's equations in reference [64], $M^{(j)}_{3q;1q'}(\mathbf{k})$ the matrix elements for transitions between motional levels, T is the temperature of the ensemble, and $\psi_{\alpha q}(\mathbf{R}_j)$ is an eigenfunction for the atom j moving in the ground or lattice potential.

The lattice contribution is responsible for the motional dephasing of the ensemble. The atoms are trapped oscillating in a lattice leading to oscillations in the retrieved signal. In Fig. 4.2 we plot these oscillations,for two trapping potentials, without any other decoherence mechanisms as a function of $\omega_0 T_s$ for $U_0/k_B = 32$ μK and $U_0/k_B T = 2.75$ using the following equation,

$$g_l(T_s) = G_l(T_s)/G_l(0). \tag{4.14}$$

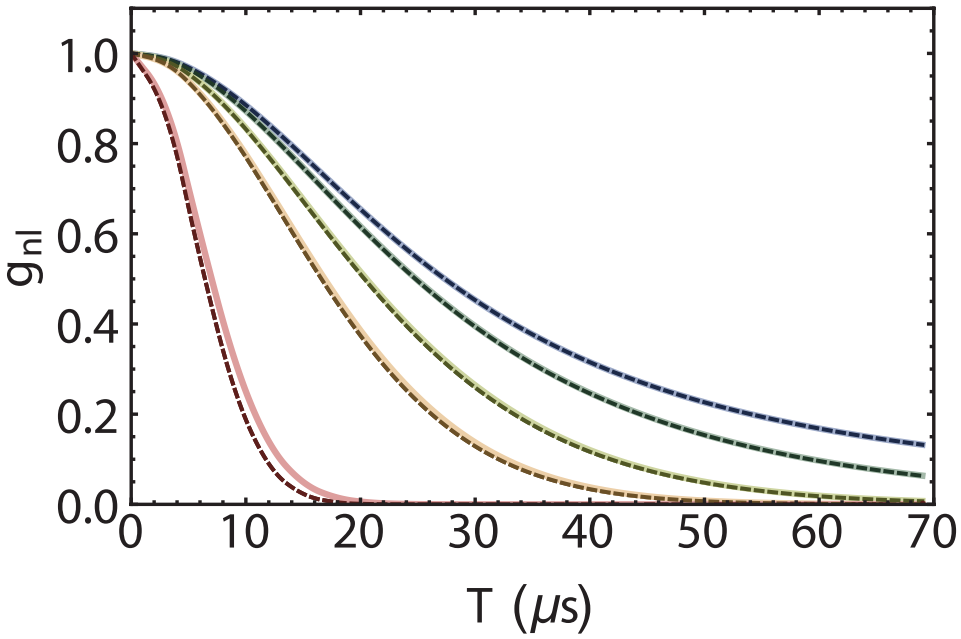

Figure 4.3: Graphs of the analytic approximation and exact expressions of g_{nl} (dashed and solid respectively), from reference [64], as a function of storage time T_s for $U_0/k_B = 40$ μK and different sample lengths: blue - $L = 1$ μm, dark green - $L = 50$ μm, light green - $L = 100$ μm, orange - $L = 150$ μm, red - $L = 500$ μm.

The frequency ω_0 is defined by

$$U_0 = \frac{1}{2}\frac{M\omega_0^2}{k_L^2}, \tag{4.15}$$

4.2.3 Non-lattice contribution

The non-lattice contribution to the signal given in Eq. (4.16).

$$G_{nl}(T_s) = \left| \int_{-\infty}^{\infty} dX \int_0^{\infty} \rho d\rho f(\rho, X) \mathcal{N}(\rho, X) e^{-i\omega_d(\rho,X)T_s} \right|^2, \tag{4.16}$$

where ω_d is the frequency shift of the non-lattice potential and $f(\rho, X)$ describes the excitation spatial modes

$$f\,(\rho, X) = \left(\frac{w_{E_1,0}}{w_{E_1}(X)}\right) \exp\left[-\frac{\rho^2}{w_{E_1}^2(X)}\right] \times \left\{\left(\frac{w_{E_2,0}}{w_{E_2}(X)}\right) \exp\left[-\frac{\rho^2}{w_{E_2}^2(X)}\right]\right\}^2, \tag{4.17}$$

$w_{i,0}$ are the transverse waists of the beams at the foci, $w_i(X) = w_{i,0}\sqrt{1 + \left(\frac{X}{X_{ri}}\right)^2}$, and X_{ri} is the Rayleigh length for the excitation beams 420 nm and 1012 nm. In our experiment,

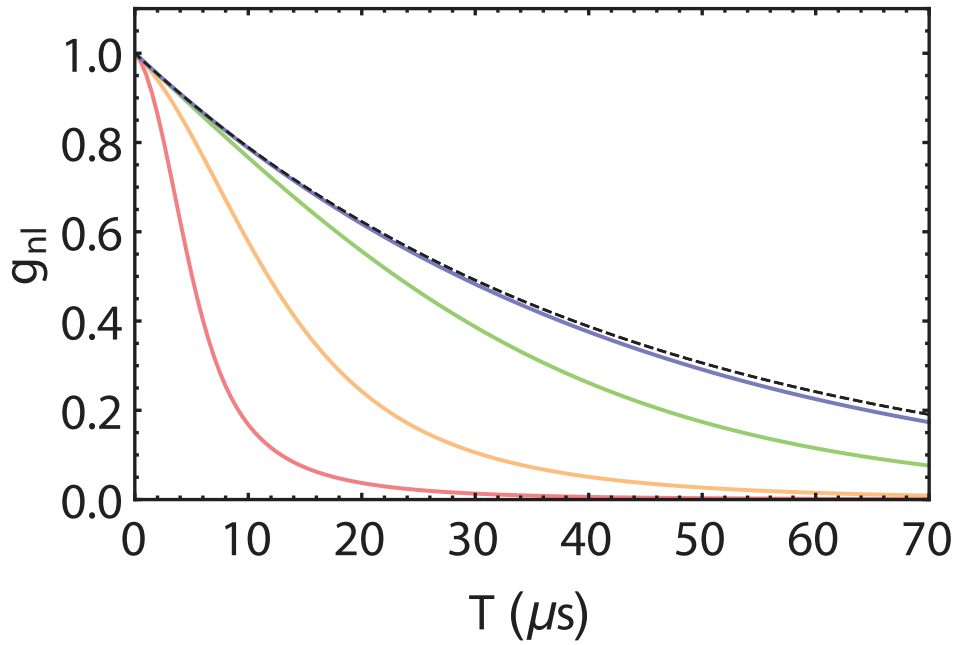

Figure 4.4: Graphs of g_{nl}, multiplied by the decay due to the dissipative mechanisms, as a function of storage time T_s for $U_0/k_B = 40$ μK, $n = 51$, and different lattice widths: blue - $w_l = 200$ μm, green - $w_l = 100$ μm, orange - $w_l = 50$ μm, red - $w_l = 25$ μm. The black dashed line shows the population decay from the dissipative mechanisms.

$w_{E_1,0} = 17$ μm, $w_{E_2,0} = 15$ μm, and the atomic density profile is given by

$$\mathcal{N}(\rho, X) = \exp\left[\frac{U_0}{2k_B T}\mathcal{I}(\rho, X)\right] \exp\left[-\frac{X^2}{L^2}\right]. \tag{4.18}$$

where L is the length of the ensemble. The non-lattice contribution can be modeled using the equation,

$$g_{nl}(T_s) = G_{nl}(T_s)/G_{nl}(0).$$

The lifetime from the non-lattice contribution is dependent on the geometry of the optical trap, excitation beams, and shape of the atomic cloud. Figure 4.3 shows that as the length of the sample is increased, the lifetime decreases. The non-lattice potential results in dephasing which reduces the coherence time because of the variation in trap depth over the length of the ensemble. Since there is more spatial variation over longer ensembles the coherence time is shorter. Figure 4.4 shows that the lifetime increases as the lattice radius gets larger. If the

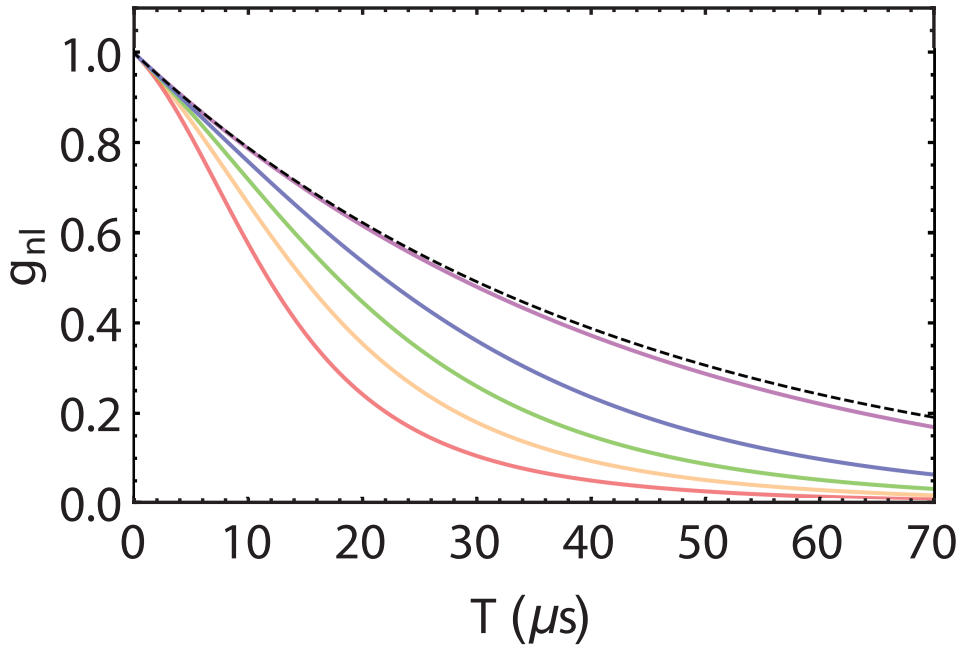

Figure 4.5: Graphs of g_{nl}, multiplied by the decay due to the dissipative mechanisms, as a function of storage time T_s for $U_0/k_B = 40$ μK, $n = 51$, and lattice width $w_l = 50$ μm and ensemble temperature : purple - $T = 0.1$ μK, blue - $T = 0.5$ μK, green - $T = 1$ μK, orange - $T = 2$ μK, red - $T = 10$ μK. The black dashed line shows the population decay from the dissipative mechanisms.

radius of the lattice beam is much greater than the radius of the excitation beam, there is little variation in the non-lattice potential over the excitation volume. Therefore, ground-Rydberg coherence times are longer.

The temperature of the sample can also have an effect on the coherence time. At very low temperatures the atoms settle in the lowest motional energy level of the optical lattice. The atoms will be motionless at the very bottom of the potential resulting in a small ensemble radius. This results in less variation of the non-lattice potential over the sample leading to longer coherence times for colder samples as seen in Figure 4.5. Lastly, the trap depth affects the coherence time as seen in Figure 4.6. As the trap depth increases the coherence time decreases as a result of the non-lattice potential becoming more significant in deeper traps.

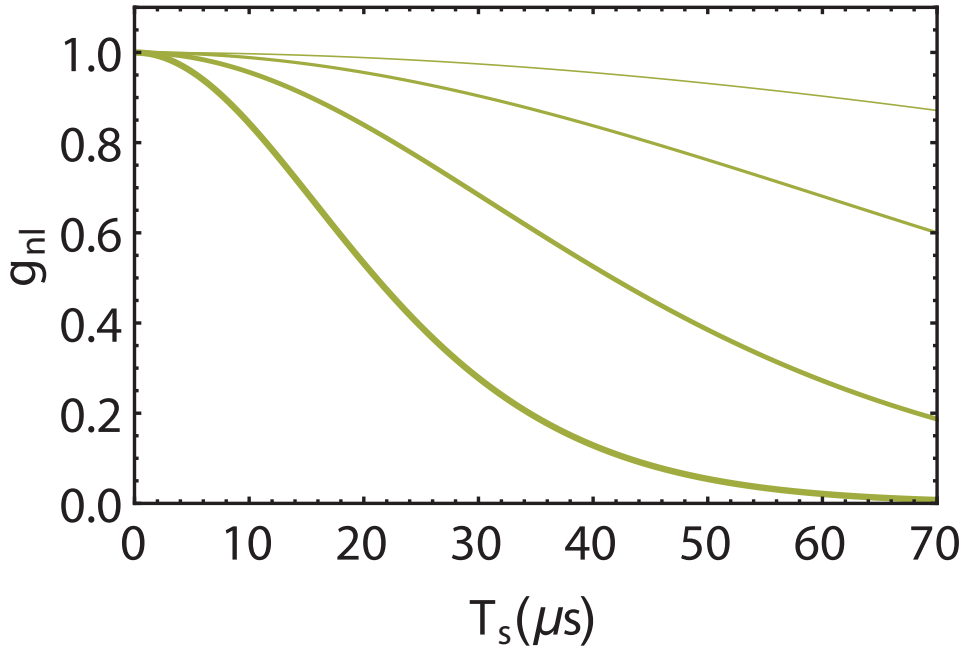

Figure 4.6: Graphs of g_{nl} for sample length $L = 100$ μm and trap depths $U_0/k_B = 5, 10, 20,$ and 40 μK, represented by increasing line thickness.

4.2.4 Dissipative mechanisms

Three dissipative mechanisms are included in the model. These three mechanisms are spontaneous decay $\tau_n^{(0)}$, transitions due to blackbody radiation $\tau_n^{(bb)}$, and transitions induced by the lattice $\tau_{6p,n}$. These decay mechanisms are modeled as,

$$\frac{1}{\tau_{eff}} = \frac{1}{\tau_{6p,n}} + \frac{1}{\tau_n^{(0)}} + \frac{1}{\tau_n^{(bb)}}. \tag{4.19}$$

The three mechanisms can be written individually as,

$$\begin{aligned} \tau_{6p,n} &= \frac{h\Delta_{m,n}}{U_0}\tau_{6p,0}; \\ \tau_n^{(0)} &= \tau^{(0)}(n^*)^{2.94}; \\ \tau_n^{(bb)} &= \frac{3\hbar(n^*)^2}{4\alpha_{FS}^3 k_B T}, \end{aligned}$$

where $\tau_{6p,0} = 125$ ns, $\tau^{(0)} = 1.43$ ns [64], $T = 293$ K, $n^* = n - 3.13$, and α_{FS} is the fine structure constant.

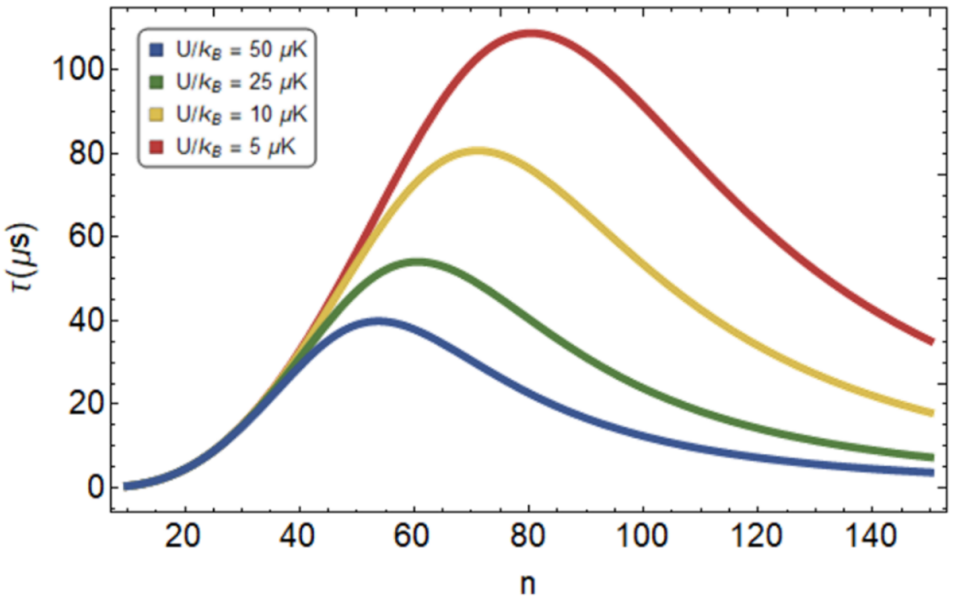

Figure 4.7: Total lifetime of the Rydberg state at different principal quantum numbers when considering lattice-induced population decay from the $6p_{3/2}$ level, spontaneous decay from the Rydberg level, and blackbody induced transitions. Together these make a theoretical maximum coherence time for trapped Rydberg atoms.

Figure 4.7 shows Eq. 4.19 for several trap depths. At low principal quantum number the lifetimes are limited by $\tau_n^{(0)}$ and $\tau_n^{(bb)}$. At higher principal quantum numbers $\tau_{6p,n}$ becomes the dominant factor. Also, we see for all principal quantum numbers that lower the trap depths leads to longer lifetimes.

4.2.5 Final model

As shown in reference [64], the lattice contribution, the non-lattice contribution, and the dissipative factors can be combined to model the complete retrieved signal as

$$G(T_s) = G_{nl}(T_s)G_l(T_s)e^{-T_s/\tau_{eff}}. \tag{4.20}$$

Our data is normalized to the signal retrieved after 1 μs storage time, therefore, we fit the data in this chapter using:

$$\eta(T_s) = G(T_s)/G(1). \tag{4.21}$$

4.3 Experimental results

The experimental geometry and measurement sequence are shown in Fig. 4.1(a). An optical lattice is formed by a y-polarized, retro-reflected laser field propagating along the x-axis having power $P_+ \approx 0.8$ W. The trap field is generated by a Titanium-Sapphire laser tunable in the 850 nm to 1050 nm range, frequency-locked to an optical cavity. The laser wavelength is measured with a wavemeter calibrated to 10 MHz accuracy using a diode laser locked to Rb 780 nm line. The trap field is detuned from $\omega_{ns,6p_{3/2}}$ by Δ.

Atoms are loaded into the lattice using a magneto-optical trap. The maximum depth of the optical dipole potential at the atoms is $U_0/k_B \approx 40$ μK, with the corresponding axial and radial oscillation frequencies $\{\nu_\rho, \nu_x\} = \{0.3, 80\}$ kHz. The resulting cloud, which has temperature of $T \approx 10$ μK, consists of $\sim 10^5$ ^{87}Rb atoms having radial and axial waists of $\sigma_\rho \approx 50$ μm and $\sigma_X \approx 0.2$ mm respectively. The atoms are optically pumped to the $|5S_{1/2}, F = 2, m_F = 0\rangle$ state in a magnetic bias field $B_0 = 0.5$ mT.

Two nearly counter-propagating, z-polarized fields, E_1 and E_2 excite a spin wave between the $|5s_{1/2}, F = 2\rangle$ and $|ns_{1/2}\rangle$ levels. The fields imprint a spatial phase coherence between the ground and Rydberg states varying as $\propto e^{i(\vec{k}_1+\vec{k}_2)\cdot\vec{R}}$, where $\vec{k}_1$ and $\vec{k}_2$ are the wave-vectors for the fields E_1 and E_2 respectively. Field E_1 has wavelength 420 nm, while field E_2, produced by a laser diode, is tunable in the 1012 nm to the 1026 nm wavelength range to excite Rydberg states with principal quantum numbers $n \geq 30$. Field E_2 is detuned from $\omega_{ns,6p_{3/2}}$ by $\Delta_1 \approx 12$ MHz. The E_1 and E_2 fields are focused onto the atoms with beam waists $w_{E_1,0} \approx 17$ μm and $w_{E_2,0} \approx 15$ μm and Rabi frequencies $\Omega_{E_1}/2\pi \simeq 0.2$ MHz and $\Omega_{E_2}/2\pi \simeq 5$ MHz, respectively. The spin wave is stored for a period T_s varied between 1 and 70 μs. At time T_s the atoms are coherently driven on the $|ns_{1/2}\rangle \leftrightarrow |6p_{3/2}\rangle$ transition by a (z-polarized) retrieval field E_R of Rabi frequency $\Omega_R \approx \Omega_{E_2}$, creating an array of atomic dipoles which give rise to a phase-matched emission from the sample. The emitted light is collected into a single-mode optical fiber coupled to a single-photon detector. To avoid

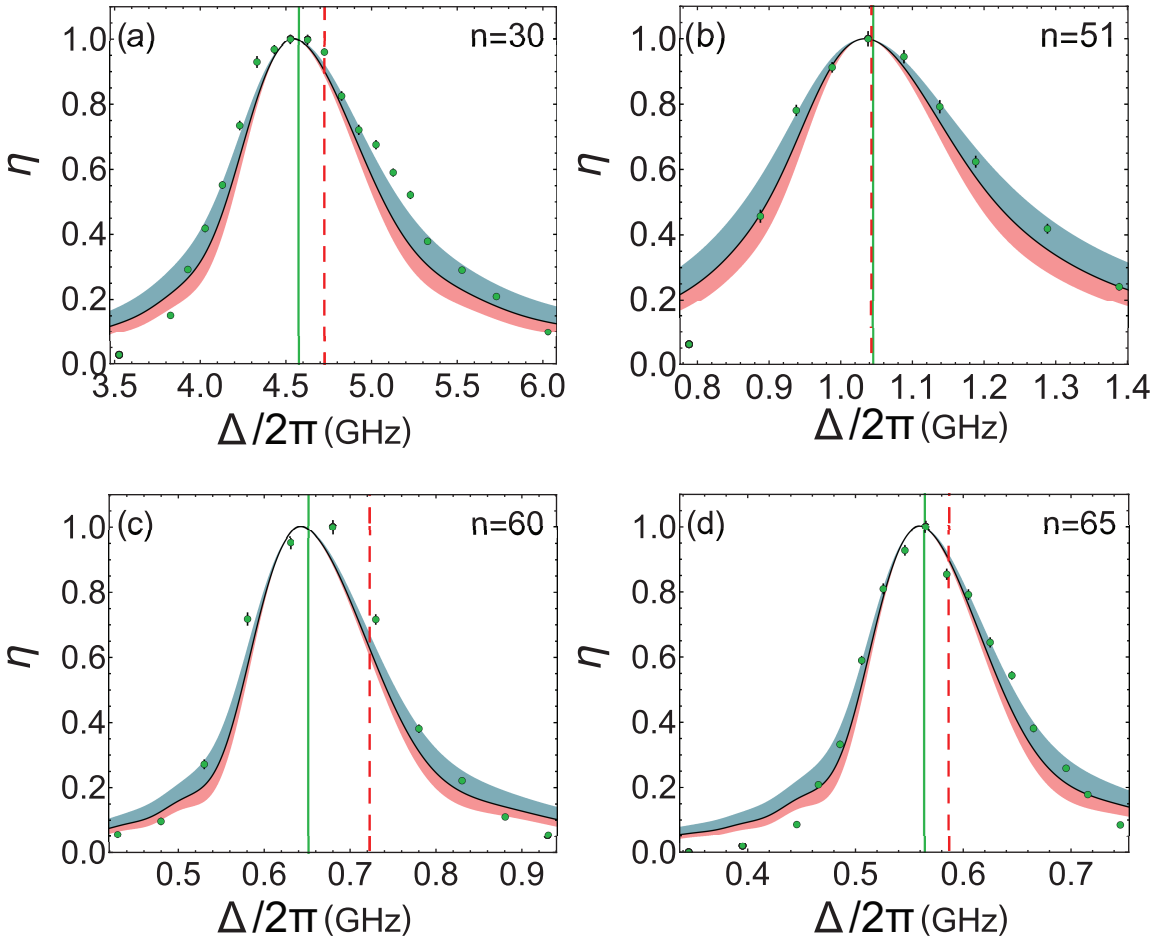

Figure 4.8: (a)-(d) Normalized signal $\eta(T_s)$ at storage time T_s around the first revival ($10 - 12$ μs) as a function of lattice detuning Δ for principal quantum numbers 30, 51, 60, and 65. The solid curves, based on the model described in the text, are used to extract the values of $\Delta_{m,n}$. The dashed red and solid green vertical lines represent the theoretically expected and the extracted values of the magic detuning, respectively. Blue and red bands represent fits using temperatures 20% lower and higher than the best fit value, respectively.

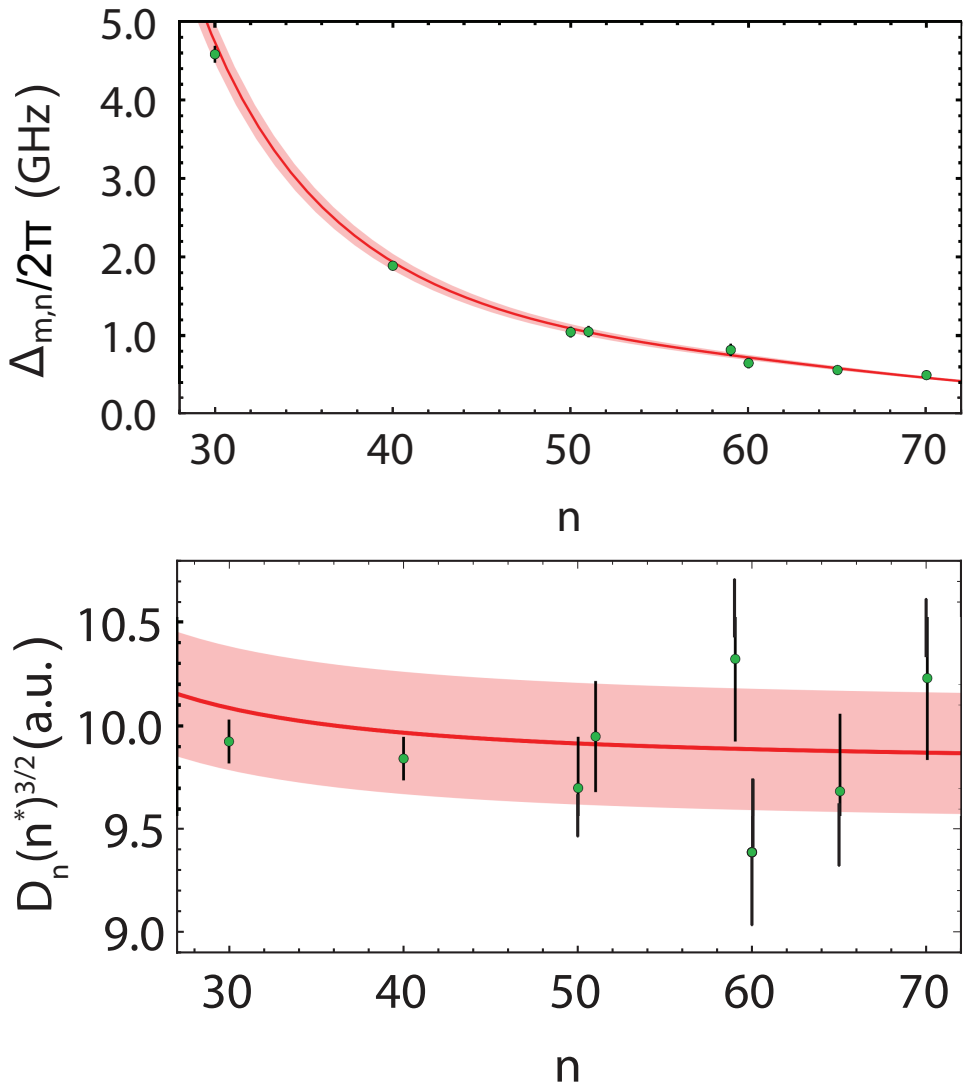

Figure 4.9: (a) $\Delta_{m,n}$ as a function of the principal quantum number n, with the solid curve based on our theoretical model. (b) Extracted values of the scaled reduced matrix elements as a function of n.

damaging the detectors by the Ω_{E_1} field, a gating acousto-optical modulator is used. The photon transmission and detection efficiency η_{td} is given by $\eta_{td} = \eta_c\eta_o\eta_f\eta_d = 0.13$, where $\eta_c = 0.89$, $\eta_o = 0.39$, $\eta_f = 0.66$ and $\eta_d = 0.55$ are vacuum cell transmission efficiency, optics transmission efficiency (including the gating AOM), fiber coupling efficiency and single photon detection efficiency, respectively. The arrival times of detected photons are recorded, and the number of detected photons per excitation and retrieval cycle is used as our signal.

4.3.1 Magic wavelengths for the $5s - ns$ transition

The normalized retrieval signal $\eta(T_s)$, given by Eq. (4.21), is plotted in Fig. 4.8(a-d) as a function of Δ, along with the experimental data points. The solid green vertical lines represent the values of the magic detunings $\Delta_{m,n}$ extracted from the fit of the theoretical curves to the data while the dashed red vertical lines represent the values of $\Delta_{m,n}$ obtained using Eq. (4.5) and the ARC values of the dipole matrix elements. The extracted values of $\Delta_{m,n}$ are plotted in Fig. 4.9(a). Consistent with the scaling of dipole matrix elements, $\Delta_{m,n}$ varies approximately as $(n^*)^{-3}$. The values of $D_n(n^*)^{3/2}$ obtained from Eq. (4.5) using the extracted values of $\Delta_{m,n}$ are shown in Fig. 4.9(b), superimposed on the expected values of the matrix elements computed using the ARC values [81]. The 3% standard deviation band is based on comparing our computed values of $|\langle 15s_{1/2}||\hat{d}||np\rangle|$ reduced matrix elements with the values for these matrix elements given in Ref. [29].

4.3.2 Dynamics of the Ground-state–Rydberg coherence

The signal as a function of T_s serves as a measure of the dynamics of the stored spin wave. With $\Delta = \Delta_{m,n}$, the signal as a function of storage time T_s, normalized to its value at $T_s = 1\mu$s, is plotted in Fig. 4.10, along with the theoretical curves. The oscillations result from the nearly periodic motion of the atoms along the optical lattice. The oscillation

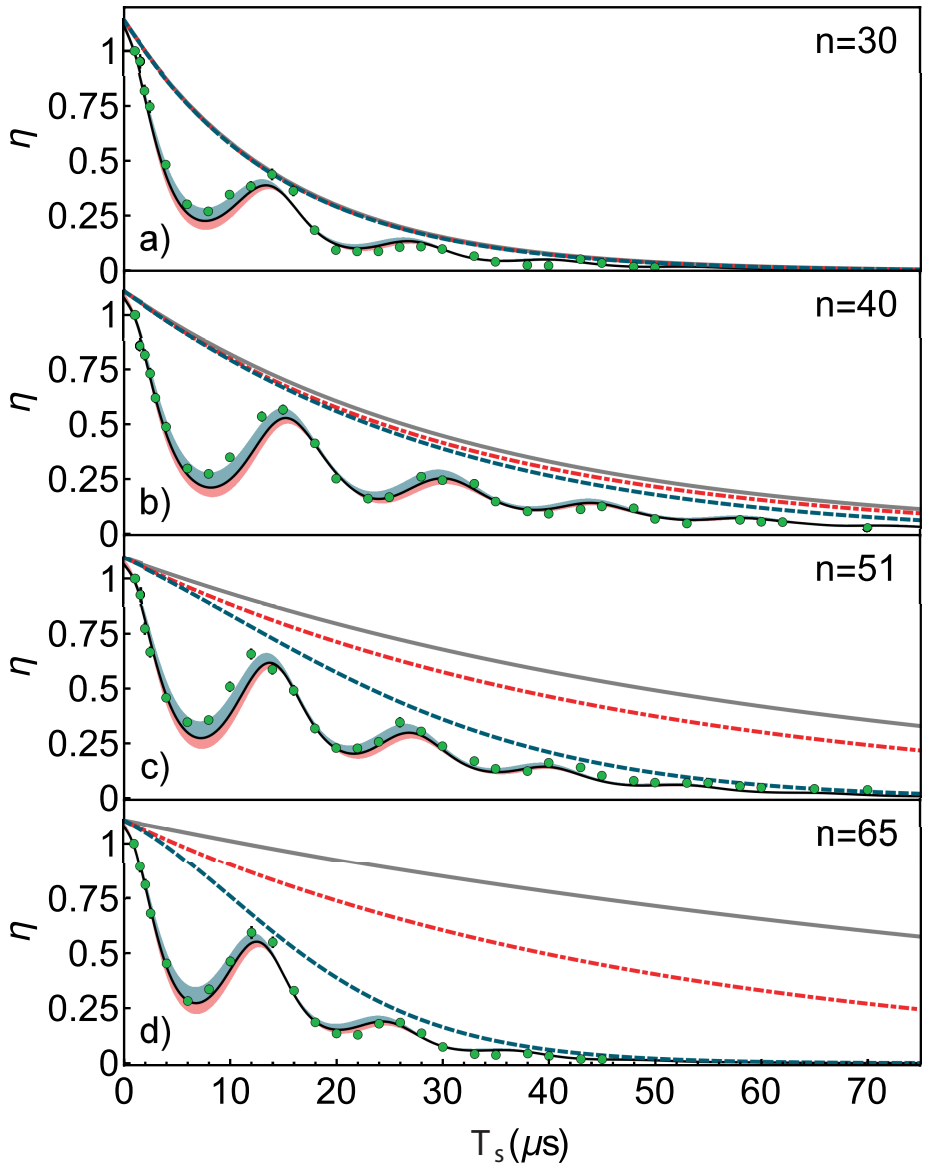

Figure 4.10: Normalized signal η as a function of storage time for several principal quantum numbers. The solid black curve is based on our theoretical model. Blue and red bands represent temperatures 20% lower and higher than the best fit value, respectively. The gray curve shows loss attributable to black-body and spontaneous decay from the Rydberg state. The dashed red curve adds in the contribution of spontaneous decay from the $6P$ level. The dashed blue curve additionally includes the dephasing attributable to the non-lattice potential. Most experimental error bars are smaller than the shown markers.

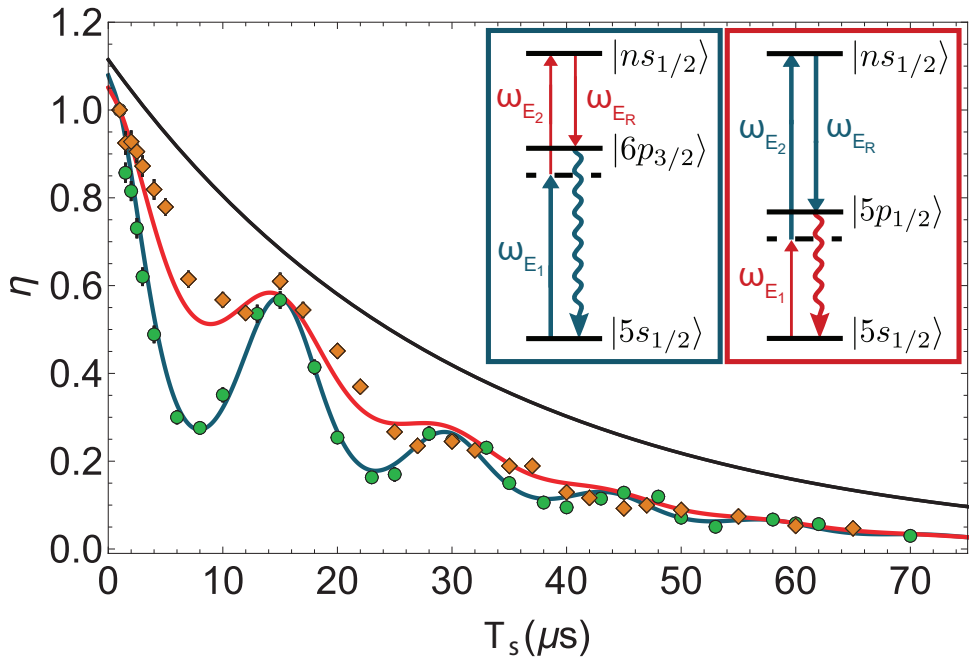

Figure 4.11: Normalized signal η as a function of storage time for $n = 40$ for 420 nm - 1018 nm (green circles) and 795 nm-475 nm (orange diamonds) excitation, with the corresponding atomic transitions shown in the inset. The solid curves are the result of a numerical simulation of atomic motion using the model described in the text. The black curve is the same as in Fig. 4.10. Most experimental error bars are smaller than the shown markers.

visibility decreases with time owing to the anharmonic nature of the potential. Moreover the anharmonicity adds a small damping component to the signal and its contribution becoming more pronounced with increasing temperature.

In Fig. 4.11 we compare the $n = 40$ signal with its counterpart obtained by exciting the atoms with 795 nm and 475 nm fields via the $|5p_{1/2}, F = 1\rangle$ intermediate level. The effective two-photon excitation wavelength for the latter $\lambda_{2ph} = 1.2$ μm, longer than $\lambda_{2ph} = 0.72$ μm for the 420 nm-1018 nm excitation. As one would expect, the 795 nm-475 nm excitation exhibits lower visibility of oscillations as a result of decreased motional dephasing for the longer-wavelength spin-wave. The role of trap anharmonicity also decreases with longer spin-wave period, whereas the non-lattice contribution to the dephasing contribution is unaffected by it.

4.4 Conclusion

We have demonstrated ground-state–Rydberg atomic coherence lifetimes in excess of 20 μs using a state insensitive optical lattice. A theory has been developed to account for the quantized motion of atoms in the trap potentials. The theoretical line shapes that are derived are in good agreement with the experimental results and can be used to extract values for the ns - $6p_{3/2}$ reduced electric dipole matrix elements. Our approach should be of use for precision measurements and quantum information studies involving atomic Rydberg states.

Chapter 5

Differential nuclear-spin-dependent light shifts and state mixing of Rydberg atoms

This chapter is based on Ref. [86]

5.1 Introduction

A promising platform for quantum information processing is based on the excitation of ultracold atoms to Rydberg states [12]. Achieving long-lived ground-Rydberg atomic coherence is one of the cornerstones of this approach. To suppress the effects of motional dephasing on this coherence, the atoms can be confined in optical potentials that are identical for the ground and Rydberg states [29, 30, 87, 88, 63, 79, 64]. However, in addition to confining the atoms, the optical trap fields also mix and shift the Rydberg energy levels. As a consequence, the energy level spacing within a given Rydberg manifold results from a complicated combination of optical field potentials, hyperfine interactions, and interactions of the atoms with any external magnetic bias fields. A complete understanding of this level structure is needed to maximize the fidelities for quantum information protocols using trapped Rydberg atoms.

In this paper we present a theoretical and experimental study of ^{87}Rb Rydberg atoms confined in an optical lattice potential and subjected to an external magnetic field. For a given

n, the frequency of the lattice fields is chosen so as to match the light shift potentials for the ground and ns Rydberg levels [63, 64]. Actually, it is not possible to match the ground state lattice potential to that of *all* the hyperfine sublevels in a given ns level. For example, an ns level of ^{87}Rb contains eight sublevels. In general, the trapping potential differs for each of these levels and must be accounted for in a complete analysis. Moreover, since the atoms are trapped in these potentials, it becomes necessary to use a fully quantum theory for the atomic motion.

The trapped atoms are subjected to a two-photon pulse that excites the atoms to a targeted Rydberg level, followed by a time-delayed readout pulse that leads to phase-matched emission from the sample. By a proper choice of excitation field polarization, the output signal, measured as a function of the time delay, contains components that oscillate at the frequency separations of the ns Rydberg sublevels.

These frequency separations contain contributions arising from the magnetic field interaction, hyperfine interaction and light shift potentials. To isolate these effects, we calculate the eigenkets and eigenenergies of the Rydberg levels in the *absence* of light shifts and then determine to what extent the light shifts modify them. The light shifts themselves are composed of near-resonance and ponderomotive contributions. The ponderomotive contribution, which includes effects related to the breakdown of the dipole approximation [88], is a function of n, but for a given n, is the same for all the sublevels. The near-resonance contribution both shifts and couples the sublevels. Rather remarkably, we find that coupling of hyperfine – magnetic field eigenkets is almost negligible for the range of our experimental parameters, although there was no *a priori* reason to believe that this should be the case when the lattice field polarization is orthogonal to the magnetic field. As a result, the only effect of the optical potential is to provide a differential shift for the Rydberg sublevels. We are able to assess the role played by these differential light shifts and to determine what effect, if any, they have on the atomic motion. In this way we determine the hyperfine constant A from the measured frequency intervals for n ranging from 30 to 65. Previously, A values were measured for low

values of n using direct optical spectroscopy [89, 90]. In these experiments, residual Doppler broadening resulted in a spectral resolution to about 100 kHz, limiting the method to $n \leq 27$. Millimeter-wave spectroscopy has been used for high-n states of atomic Cs, with kHz-level resolution achieved using ultra-cold atoms [91]. In this work we achieve a resolution as low as several kHz.

5.2 Experiment

The experimental setup and level diagram for one of our excitation schemes are shown in Fig. 5.1. For the most part, the experimental setup is identical to the one used in our previous work Ref. [64]. The major difference is that the polarization of the field Ω_1 in the current experiment has both y and z components whereas it was z-polarized in the previous experiment. An ultra-cold sample of Rb atoms is loaded into a one-dimensional optical lattice formed by counter-propagating optical fields polarized along the y-axis. The measurements are made using a magnetic field $B = 5$ Gauss for which the electronic Zeeman splitting is much greater than the hyperfine separations of the ns levels being studied, the so-called hyperfine Paschen-Back regime. In this case the $ns_{1/2}$ Rydberg level splits into two manifolds, characterized by $m_J = \pm 1/2$, separated in frequency by ≈ 14 MHz, with each manifold consisting of four m_I-components. The ~ 1 MHz two-photon excitation bandwidth $\delta\nu$ is much smaller than the frequency separation between the two manifolds. The lattice wavelength $\lambda \simeq 1012 - 1027$ nm is tuned to near-resonance with the $|6p_{3/2}\rangle \leftrightarrow |ns_{1/2}\rangle$ atomic transition, the specific value chosen to match the optical potentials for the ground state and the $m_F = m_J + m_I = 0$ component of the Rydberg Zeeman manifold.

The ensemble is driven resonantly to the Rydberg state $|ns_{1/2}\rangle$ using counter-propagating, $T_e = 1$ μs-long, pulses of a 420 nm field Ω_1 and a (nominally) 1012 nm field Ω_2. The polarization of Ω_1, controlled by half-wave plate oriented at an angle $\theta_i/2$ with respect to z-axis, is a linear combination of the y- and z-polarizations, while Ω_2 is purely z-polarized.

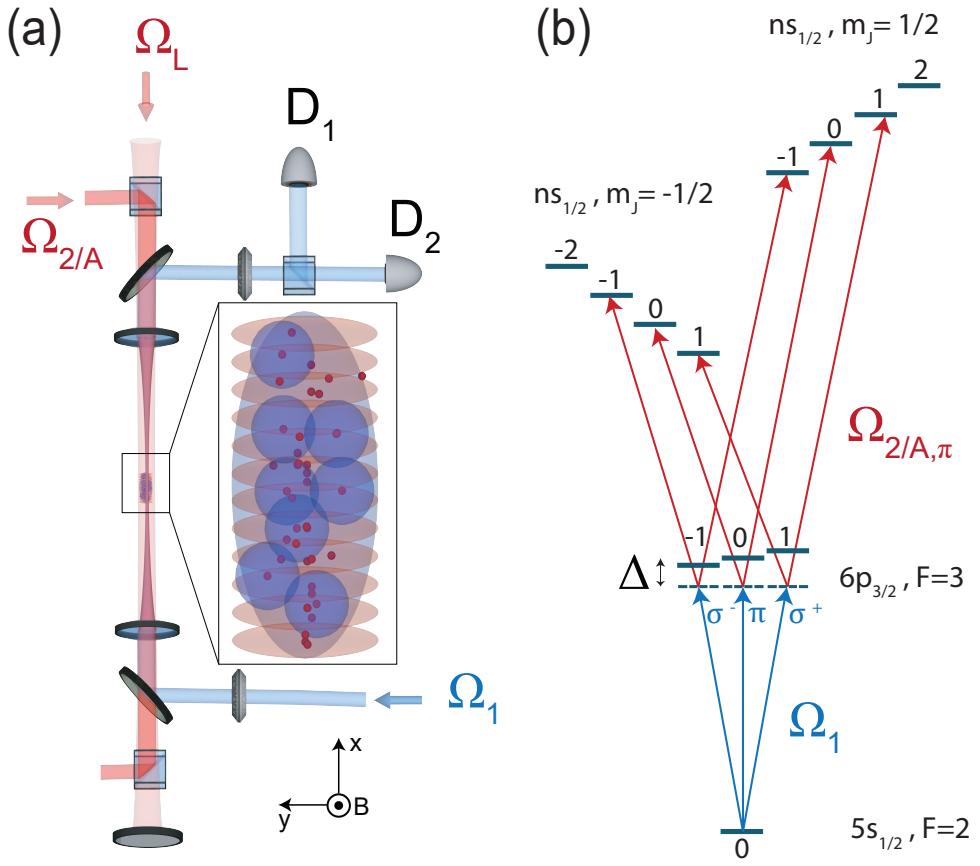

Figure 5.1: (a) Experimental setup. An ultra-cold sample of ^{87}Rb gas is trapped in a "magic" one-dimensional optical lattice formed by a retro-reflected lattice beam Ω_L that is directed along the x axis and polarized in the y direction. Two excitation beams, Ω_1 (420 nm) and Ω_2 (varying between 1013 nm and 1026 nm) counter-propagate along the x axis and are focused at the position of the atomic sample cloud with ($\frac{1}{e^2}$) waists of 17 and 15 μm, respectively. After a time delay T_s following the excitation pulse, a retrieval field Ω_A generates a phase-matched output signal. The polarization of field Ω_2 and the retrieval field Ω_A is fixed in the z-direction, whereas the polarization of field Ω_1 has both y and z components that are adjusted to optimize the modulation depth of the output signal. The output signal has both y- and z- components which are mixed with a half-wave plate, split by a polarizing beam splitter, and measured by single-photon detectors $D_{1(2)}$. (b) Atomic level diagram showing the initial ($|5s_{1/2}, F = 2, m = 0\rangle$) state, intermediate ($|6p_{3/2}\rangle$), and Rydberg $|ns_{1/2}\rangle$ sublevels. The final state manifold consists of two, spectrally resolved Zeeman sub-manifolds, each containing four levels. Even in the presence of light shifts, $m_F = m_J + m_I$ remains a good quantum number. For this excitation scheme, the $m_F = 0, \pm 1$ levels in each electronic Zeeman manifold are populated.

In this way three m_I-components in a given electronic Zeeman manifold of $|ns\rangle$ are excited. After a storage period T_s, the atoms are coherently driven by a (z-polarized) 10 μs-long retrieval field Ω_A whose frequency is resonant with the $|ns\rangle \leftrightarrow |6p_{3/2}\rangle$ transition . The ensuing cooperative emission on the $|6p_{3/2}\rangle \leftrightarrow |5s_{1/2}\rangle$ transition is directed through a half-wave plate and polarizing beam splitter. Each of the output polarization modes is collected into a single-mode fiber and directed onto a single-photon detector.

5.3 Theory

In this section, we examine three sources of energy shifts for the nuclear sublevels of Rydberg atoms confined to an optical lattice: the hyperfine interactions, magnetic fields, and light shifts. This will be done in two parts: the eigenfrequencies when considering just the hyperfine interactions and magnetic fields will be stated. This gives a simplified version of the frequency splitting we measure for the hyperfine constant. Second, I will state the full theoretical model. For a detailed derivation of the model see reference [86].

The contribution to the total system due to the hyperfine interaction contribution, denoted by H_{hf} in the $|nFm_F\rangle$ basis in frequency units is

$$\frac{\langle nF'm'_F| H_{hf} |nFm_F\rangle}{h} = \nu_{hfs} \begin{cases} \frac{3}{8}\delta_{F,2} \\ -\frac{5}{8}\delta_{F,1} \end{cases} \delta_{F,F'}\delta_{m_F,m'_F}, \tag{5.1}$$

where $\delta_{a,b}$ is a Kronecker delta. The magnetic field interaction contribution is,

$$H_B = -\frac{\beta_0 B}{\hbar}\left(g_s S_z + g_I \frac{m_e}{m_p} I_z\right). \tag{5.2}$$

When one diagonalizes $H_{hf} + H_B$ the eigenfrequencies are equal to

$$
\begin{aligned}
\nu_{n8} &= \frac{3\nu_{hfs}}{8} + \nu_B && m_F{=}\ 2 \\
\nu_{n7,n1} &= \frac{-\nu_{hfs} \pm 4\sqrt{\nu_{hfs}^2 + 2\nu_{hfs}\nu_B + 4\nu_B^2}}{8} && m_F{=}\ 1 \\
\nu_{n6,n2} &= \frac{-\nu_{hfs} \pm 4\sqrt{\nu_{hfs}^2 + 4\nu_B^2}}{8} && m_F{=}\ 0 \\
\nu_{n5,n3} &= \frac{-\nu_{hfs} \pm 4\sqrt{\nu_{hfs}^2 - 2\nu_{hfs}\nu_B + 4\nu_B^2}}{8} && m_F{=}\ -1 \\
\nu_{n4} &= \frac{3\nu_{hfs}}{8} - \nu_B && m_F{=}\ -2
\end{aligned}
\tag{5.3}
$$

where i labels the frequency ν_{ni} of each level, one being the lowest frequency and eight being the highest. The Pashen-Back region is in the limit that $\nu_B \gg \nu_{hfs}$. This is approximately satisfied in our experiment with $\nu_B \approx 7$ MHz and $\nu_{hfs} < 2$ MHz at $n = 30$ and $\nu_{hfs} < 0.8$ MHz at $n \geqslant 40$. An example of the frequency shift for the different nuclear sublevels as a function of the magnetic field can be seen in Figure 5.2 for principal quantum number $n = 50$. At $n < 50$, ν_{hf} is larger, however, because our experiment is run at ≈ 5 Gauss we are always in the Pashen-Back region. In the Pashen-Back region, the splitting between two adjacent nuclear sublevels, within a manifold, is $\approx \nu_{hf}/4$ for all magnetic fields, in the absence of light fields. So the frequency splittings, in our setup, will mainly come from two factors: hyperfine interaction and light shifts due to the lattice. The lattice introduces optical potentials that cause shifts between different levels in a manifold. This will be included in the full theory in the next section. However, as will be explained later in the chapter, the effect of the trap will be measured and we used this to determine ν_{hf} at zero trap depth.

5.3.1 Final equation

The final equation found in reference [86] for fitting the signal from the atoms is,

$$
\eta_V(T_s) = S_V(T_s)/S_V(T_s = 1\mu s), \tag{5.4}
$$

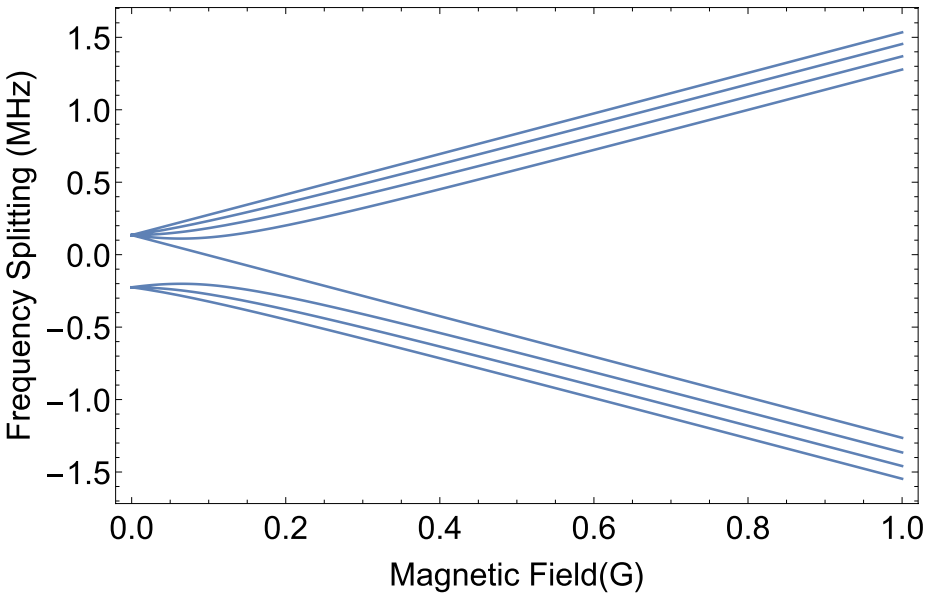

Figure 5.2: Hyperfine splitting of nuclear sublevels of both electronic sublevels as a function of the magnetic field for $n = 50$. At high magnetic fields, the atom is in the so-called Paschen-Back regime when all of the splittings between the nuclear sublevels are approximately constant and equal. For this experiment, the magnetic field is $B = 5$ Gauss, well into the Paschen-Back regime.

the normalization factor in the denominator corresponds to the signal retrieved after 1 μs storage time. This equation was used to fit all of the data in the next sections and measure the hyperfine splittings as well as the differential nuclear-spin-dependent light shifts. The function S_V is defined by,

$$S_V(T_s) = \left| \int_{-\infty}^{\infty} dX \int_0^{\infty} \rho d\rho \Lambda(\rho, X) \mathcal{N}(\rho, X) C_V(\rho, X, T_s) \right|^2 \times e^{-\Gamma_{ns} T_s}, \tag{5.5}$$

$\Lambda(\rho, X)$ characterizes the excitation and retrieval pulses spatially dependent Rabi frequencies and $\mathcal{N}(\rho, X)$ is the atomic density distribution. $e^{-\Gamma_{ns} T_s/2}$, accounts for the dissipative mechanism in Chapter 4. $C_V(\rho, X, T_s)$ are the contributions from motional states in the ground state lattice potential and is described by,

$$C_V(\rho, X, T_s) = \sum_{m_F=-1}^{2} \sum_{q,q'}^{q_{\max}} e^{-i\omega_{nsm_F} T_s} Q^{(V)}_{pJnsm_F}$$
$$\times e^{-2\pi i \tilde{D}^{(j)}_{nsm_F}(\rho,X)T_s} M_{gq;nsm_Fq'}(-k)$$
$$\times M_{nsm_Fq';gq}(k)\, e^{i\left(\omega_q^{(g)} - \omega_{q'}^{(nsm_F)}\right)T_s} \rho_{1q,1q}(0), \tag{5.6}$$

where $\rho_{1q,1q}(0)$ is the density matrix elements for the initial distribution of motional energy level states. ω_{nsm_F} accounts for differential light shifts, as well as the magnetic and hyperfine interactions. The function $Q^{(V)}_{pJnsm_F}$ describes the excitation and retrieval dynamics. $\tilde{D}^{(j)}_{nsm_F}(\rho, X)$ is the difference in non-lattice potentials between Rydberg and ground state levels. $M_{nsm_Fq';gq}(k)$ are the matrix elements for coupling of motional states between the ground and Rydberg levels. The frequencies $\omega_q^{(g)}$ and $\omega_{q'}^{(nsm_F)}$ are the frequencies of the ground and nsm_F lattice potentials. The sums over q, q', q'' are restricted to the bound states.

5.4 Excitation and retrieval polarization

To optimize the retrieved quantum beat signal such that we have the most accurate measurement of the frequency splitting, the polarization of the excitation beam and the retrieved photons must be carefully chosen. To this end, a simplified model can be used, where the atoms are excited from the ground level to three equally separated nuclear-sublevels in the Rydberg state $m = -1, 0, 1$. The polarization of the excitation beams controls which of the three nuclear-sublevels are populated. For our experiment, the magnetic field is along the z-axis and the excitation beams are propagating along the x-axis as can be seen in Figure 5.1. Polarization components along the y-axis will drive σ^+ and σ^- transitions. Polarization along the z-axis will drive π transitions. Therefore, the angle of excitation, along with the *Clebsch-Gordan* coefficients, controls the proportion excited to each of the nuclear-sublevels.

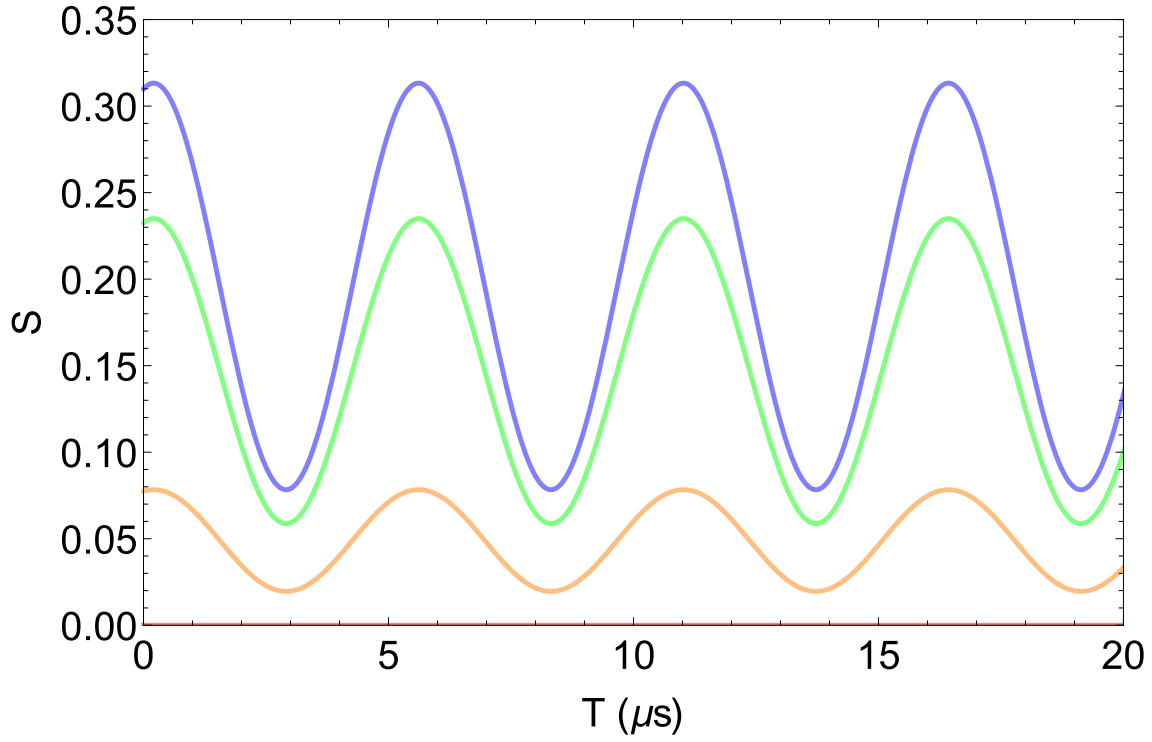

Figure 5.3: Retrieved signal S as a function of storage time T for $\theta_1 = 0°, 30°, 60°, 90°$ in red, orange,green, and blue, respectively. The principal quantum number for this frequency of quantum beat is $n = 51$ and an retrieved polarization angle of $\theta_2 = 0°$.

The effect of the excitation polarization is shown in Fig 5.3. The angle for this polarization should be chosen such that the oscillation visibility is greatest.

The emitted photon polarization is dependent on the final distribution of the excitation probability among the three nuclear sublevels. In Figure 5.1 (b) the three nuclear sublevels we populate are labeled $m = -1, 0, 1$. Upon retrieval, the population in sublevels $m = 1$ and $m = -1$ will emit a field polarized along the y-direction and the population in $m = 0$ will emit a field polarized along the z-direction. A half-wave plate and polarizing beam splitter can select the emission from which nuclear sublevels are directed to a photon detector. Since the energy splitting between levels $m = 1$ and $m = -1$ is twice as large as between levels $m = \pm 1$ and $m = 0$ the beat frequency is twice as high between the outer two energy levels (1 and -1). Therefore, it is useful to measure the retrieved signal or the emission with polarization along the y-axis because a higher frequency can be measured more accurately in

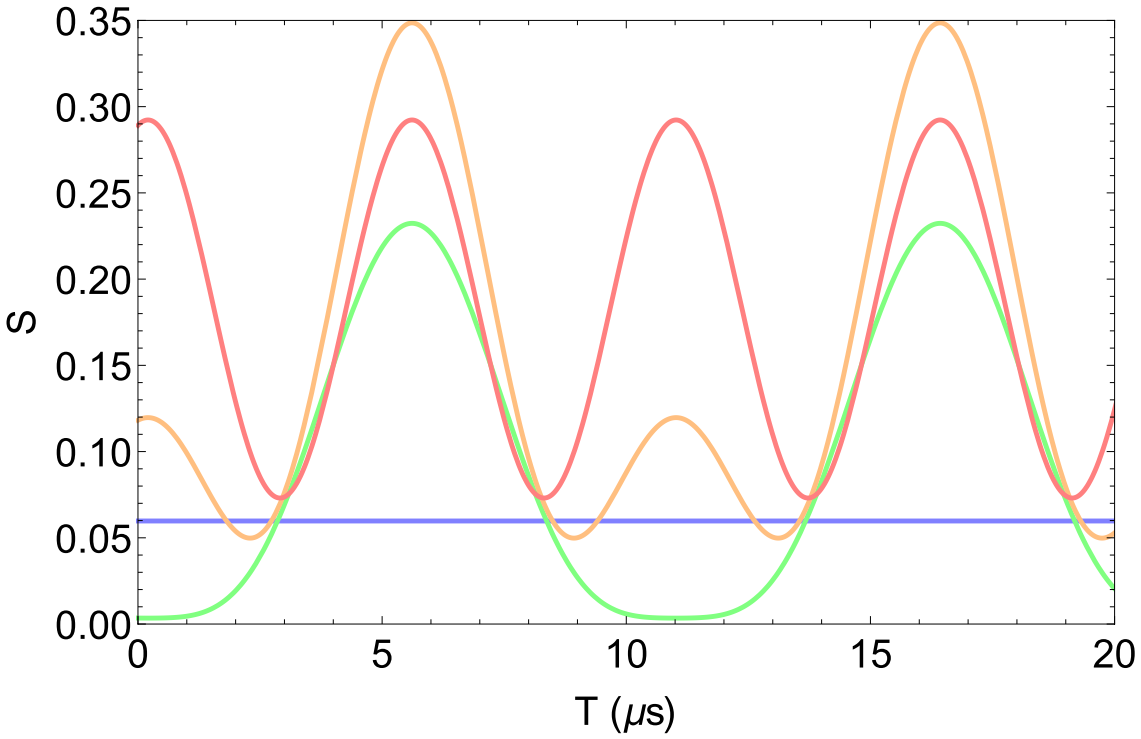

Figure 5.4: Retrieved signal S as a function of storage time T for $\theta_2 = 0°, 30°, 60°, 90°$ in red, orange,green, and blue, respectively. The principal quantum number for this frequency of quantum beat is $n = 51$ and an retrieved polarization angle of $\theta_1 = 0°$.

the same coherence time. The dependence of the output signal on the polarization selected to go to the photon detectors can be seen in Fig 5.4. The total output signal is described by the equation

$$S = |C_1 \sin(\theta_2)\cos(\theta_1) + C_2 \sin(\theta_1)\cos(\theta_2)(e^{-i\omega T} + e^{i\omega T})|^2, \tag{5.7}$$

where θ_1 is the angle of the excitation polarization, θ_2 is the angle of the polarization which is directed to the detector, T is the storage time, ω is the frequency of the nuclear sublevel splitting, and C_1 and C_2 are determined by the *Clebsch-Gordan* coefficients for the given excitation scheme.

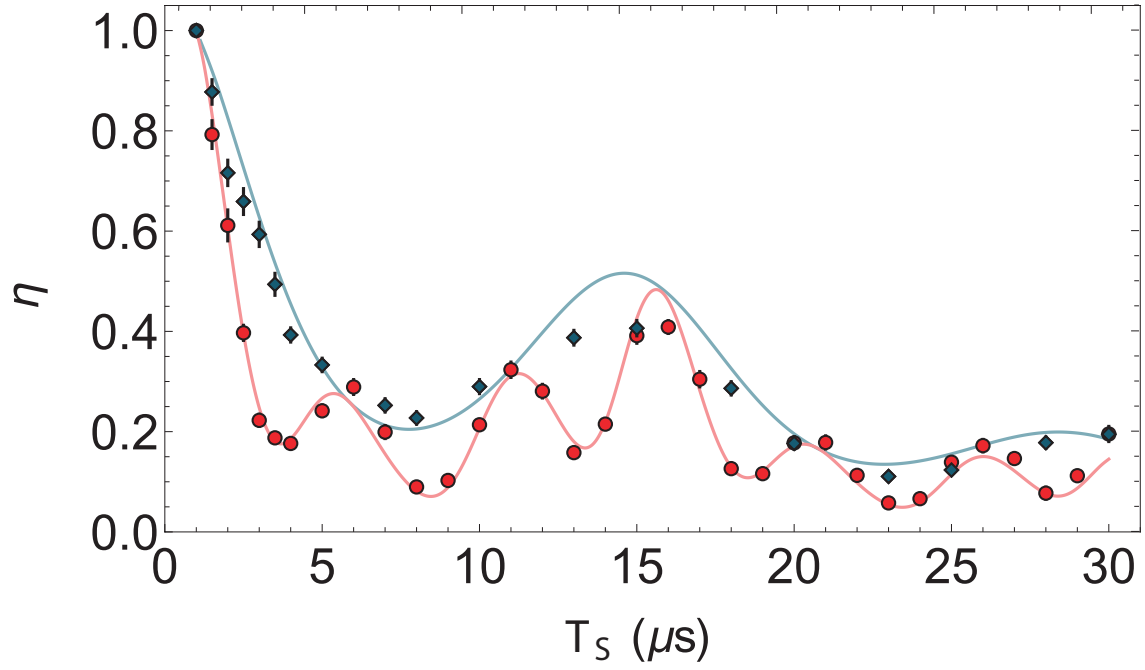

Figure 5.5: Normalized signal $\eta \equiv F(T_s)/F(T_s = 1\ \mu s)$ as a function of storage time for principal quantum number $n = 40$ with fitted trap depth $U_0/k_B = 31\ \mu K$ and temperature $T = 10\ \mu K$ for a single excited state (blue) and a triplet of states (red) using (θ_i, θ_d)=$(0, 24)$ and $(32, 24)$ respectively. Solid curves are based on our theoretical model.

5.5 Analysis of retrieved signal

Let us first consider the data for $n = 40$. As a function of delay time T_s between the excitation and readout pulses, the overall signal decays, primarily as a result of blackbody-induced transitions and spontaneous decay. In addition to the overall decay, the signal exhibits an oscillatory behavior. If the trap potentials are purely harmonic characterized by frequency ω and if the ground and Rydberg potentials are matched, for a ground state thermal distribution,

$$\rho_{1q,1q}(0) = \left(1 - e^{-\beta}\right) e^{-q\beta}; \qquad \beta = \frac{\hbar\omega}{k_B T}, \tag{5.8}$$

the quantity C_V in Eq. (5.6) can be written in the form [93]

$$|C_V(T_{21})| \approx e^{-2\zeta^2[1-\cos(\omega T_s)]/\beta} \times \left|1 + Q_1 e^{-i\omega_{10}T_s} + Q_{-1} e^{-i\omega_{-10}T_s}\right|, \tag{5.9}$$

where

$$\zeta = k_{12}\sqrt{\frac{\hbar}{2M\omega}} \tag{5.10}$$

is the Lamb-Dicke parameter for the excitation field (k_{12} is the effective propagation constant for the two-photon excitation field and M is the atomic mass) and ω_{m0} ($m = -1, 1$) is the frequency difference between the Zeeman Rydberg sublevel having total magnetic quantum number m from the level having $m = 0$. For $n = 40$, the quantity ω_{m0} results primarily from the hyperfine and Zeeman interactions. For $n = 40$ the light shifts for the Rydberg sublevels can be neglected as they have an insignificant effect on the signal. The frequency ω is determined by the depth of the trap potential U_0.

To fit our data we need to know the value of the trap depth U_0 and the temperature T. We obtain values for these quantities by fitting our data with the half-wave plate angle controlling the polarization of the first excitation field to $\theta_i = 0$. In this case, both the fields that constitute the two-photon excitation scheme are z-polarized, and $Q_{\pm 1} = 0$ in Eq. (5.9). The retrieved signal in this case, displayed as blue diamonds in Fig. 5.5 exhibits the oscillatory behavior predicted by the exponential term in Eq. (5.9), which can be attributed to the center-of-mass motion of the atom within the optical lattice trap potential. In fitting the data to theory, however, we allow for trap anharmonicity [see Eq. (5.6)] and extract values for U_0 and T from the frequency and visibility of the oscillations, respectively. A theoretical curve using the best-fit value of $U_0/k_B = 31\ \mu K$ and $T = 10\ \mu K$ is displayed in the figure as a solid blue curve. If the potential were purely harmonic, the signal would rephase at integral multiples of the trap frequency; however owing to the trap anharmonicity, the oscillations are no longer purely periodic. Trap anharmonicity also adds slightly to the decay of the signal.

Having obtained values of U_0 and T, we switch the half-wave plate angle to an angle $\theta_i \neq 0$. In that case the signal oscillates at the beat frequency between the different Rydberg sublevels. Fitting the signal to the full theoretical expression given in Eq. (5.6) using the best-fit values of U_0 and T found previously allows us to extract the hyperfine splitting

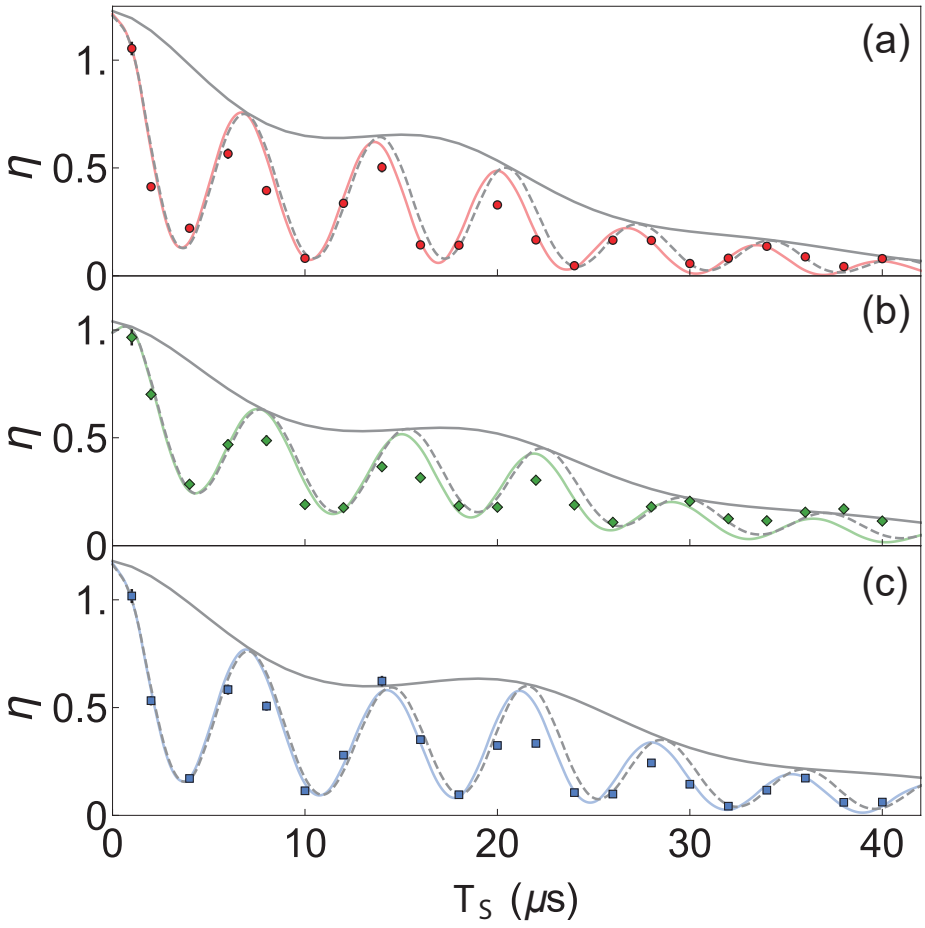

Figure 5.6: Normalized signal η utilizing the alternative excitation scheme via the intermediate $|5p_{1/2}\rangle$ state and $(\theta_i, \theta_d) = (32°, 24°)$ for the $m_J = -1/2$ electronic Zeeman component and principal quantum number $n = 60$. Experimental data with best-fit values of temperature of $4\ \mu K$ and trap depths of $U_o/k_B = 22, 18$ and $14\ \mu K$ are shown as red circles, green diamonds, and blue squares, respectively, along with color-coded curves that represent the predictions of a theoretical model that take into account the state-dependence of the optical potentials. The dashed gray curves correspond to a theory in which this state dependence is neglected and a single optical potential is used (that of the $m_F = 0$ sublevel). The solid gray theory curves correspond to an excitation scheme in which field Ω_1 is z-polarized.

ν_{hfs}, treated as a free parameter. The quantities $Q^{(V)}_{nsm_F}$ appearing in Eq. (5.6) are also treated as adjustable parameters in the fitting procedure to account for the uncertainties in the bandwidths, detunings and strengths of the excitation and retrieval pulses. A representative output signal in one of the detectors is shown in Fig. 5.5 with experimental data points displayed as red circles and theory as the solid red curve. We find agreement between the experimental data and the best-fit models obtained via Markov Chain Monte Carlo fitting. The input and output polarization angles $\theta_i = 32^\circ$ and $\theta_i = 24^\circ$ were empirically chosen to maximize the visibility of the Rydberg Zeeman beat frequency oscillations.

We have also used an alternative excitation scheme with a smaller value of k_{12} that leads to a diminished amplitude of the oscillations attributed to motion in the traps (see the dashed gray curves in Figure 5.6). In this scheme atoms are optically pumped into the $\left|5s_{1/2}, F = 2, m_F = 2\right\rangle$ ground state and using the $5p_{1/2}$ level as the intermediate state for two-photon excitation with fields Ω_1 and Ω_1 having wavelengths of 795 nm and 475 nm. The signal in this case is shown in Fig. 5.6 for $T = 4\ \mu K$ and trap depths $U_0/k_B = 22$, 18, and $14\ \mu K$.

For $n = 40$, the light shifts do not significantly contribute to the separation between the three m_F Rydberg sublevels that are excited. Moreover, the *differential* optical potentials for the three states are sufficiently small to result in approximately the same motional states for the three levels. This is no longer the case for higher values of n. For example, the theoretical curves shown in Fig. 5.6 for $n = 60$, exhibit differences between the models assuming a single state independent potential (that associated with the $m_F = m_J + m_I = 0$ level) and the true state-dependent potentials. In addition, for higher values of n, effects of spontaneous decay from the $\left|6p_{3/2}\right\rangle$ state, which is coupled to the Rydberg levels by the trap fields adds to the signal decay rate. Moreover, the dephasing associated with the breakdown of the dipole approximation in calculating the contributions of the ponderomotive potential to the light shifts also increases the decay of the signal [88]. Experimental data for $n = 60$ shown in Fig. 5.6 do not allow us to distinguish definitively between the state-independent

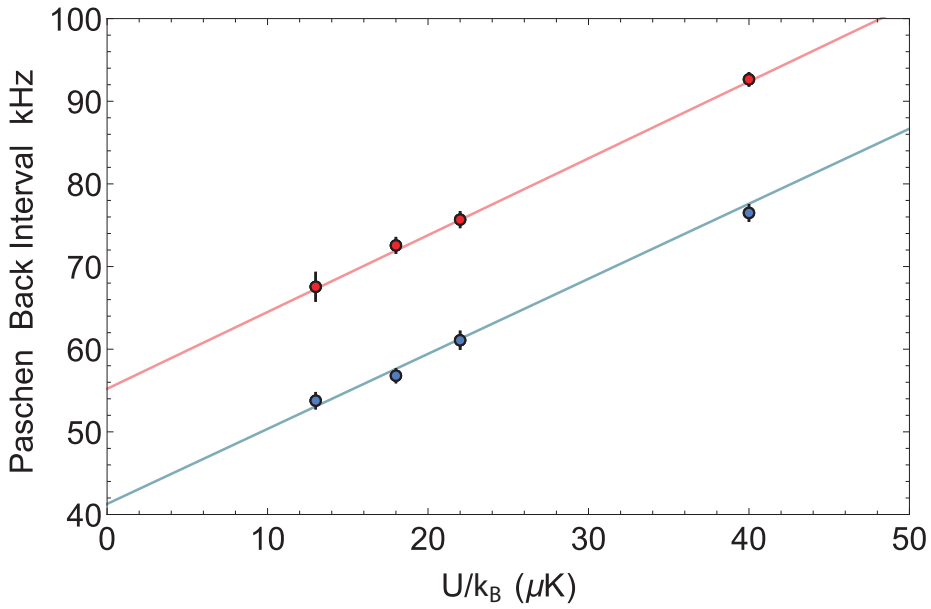

Figure 5.7: Average frequency separation between adjacent nuclear-spin states within the same m_J manifold for the $n = 60$ Rydberg level as a function of trap depth for the upper ($m_J = \frac{1}{2}$, blue circles) and lower ($m_J = -\frac{1}{2}$, red circles) electronic Zeeman manifold.

and state-dependent potential models.

The measured frequency intervals as a function of trap depths are displayed in Fig. 5.7 for the two electronic Zeeman components of the $|60s_{1/2}\rangle$ level, together with linear fits based on Eq. (5.3) from this Chapter and Eq. (A26) in reference [86]. The two intervals differ by the nuclear Zeeman interaction. The intervals in the absence of the trapping potential are determined by the intercepts of the fits with the ordinate. Using Eq. (5.3) the value of the hyperfine splitting $\nu_{hfs} = 193 \pm 5$ kHz for the $n = 60$ Rydberg state is determined.

For other values of n, fits similar to those in Fig. 5.5 are made for a single value of the trap depth. Each value of ν_{hfs} constitutes a weighted average of values obtained over up to three runs using data recorded by the two detectors. The mean value ν_{hfs} is computed as a weighted average of $\nu_{hfs}^{(i)}$, with the weights being their inverse variances extracted from the individual fits.

The two main sources of uncertainty for ν_{hfs} are 1) the statistical which is evaluated as weighted sum of the individual values, and 2) the uncertainty in the determination of the trap

depth which translates into an error of the inferred differential light shifts for the hyperfine Paschen-Back states. The $\nu_{hfs} \sim n^{-3}$, while differential light shifts scale as $\sim n^3$. As a result, the statistical uncertainty is the dominant one for $n = 30$ and 40, whereas the error due to the uncertainty of the trap depth is the larger one for states of $n \geq 51$. The data are shown in Figure 5.8(a) along with a fit using $\nu_{hfs} = C(n - 3.13)^{-3}$ with C as an adjustable parameter. In Figure 5.8(b) we plot the scaled hyperfine constant $A_{ns} \equiv \nu_{hfs}(n - 3.13)^3$. The weighted average $\overline{A}_{ns} = 35.71 \pm 0.18$ GHz is plotted as a dashed line together with a corresponding 95% confidence region. Also shown are the results of prior measurements of A_{ns} [95, 89, 90, 96, 97].

5.6 Conclusions

In summary, we have analyzed nuclear-spin manifolds associated with the ns Rydberg levels of ^{87}Rb atoms placed in magnetic and optical lattice fields. Using the eigenvalues and eigenkets for the Rydberg manifold, we have investigated the dynamics of phase-matched emission following illumination of an ensemble of cold atoms with excitation and readout laser pulses. In this way, Rydberg state-dependent light shifts and hyperfine splittings for principal quantum numbers between $n = 30$ and $n = 65$ have been determined. Our results have relevance to implementations of optically-trapped Rydberg qubits allowing for high-fidelity quantum gates.

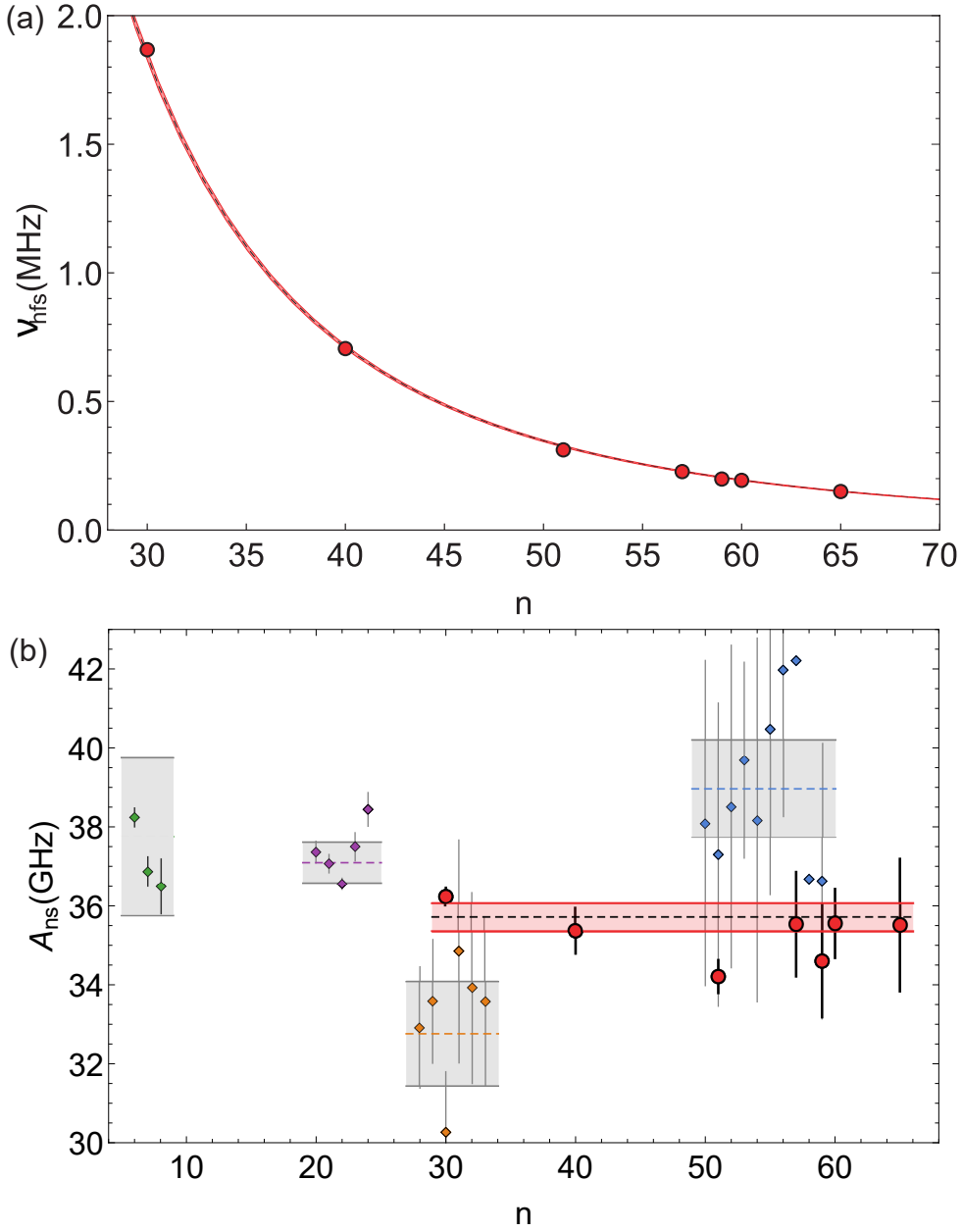

Figure 5.8: (a) Hyperfine frequency ν_{hfs} as a function of principal quantum number n. (b)The same data as the previous figure after removing the $(n - 3.13)^{-3}$ dependence. The red band represents a 95% confidence interval for our fitted value. Gray intervals are data from Ref. [95] (green), Ref. [89] (purple), Ref. [96] (orange), and Ref. [97] (blue).

Chapter 6

Conclusion

6.1 Summary and outlook

Neutral atoms excited to states with a high principal quantum number ($n > 10$) have strong and controllable state-dependent interactions making them a promising platform to study quantum information, quantum optics, and many-body phenomena. For example, collective effects in ensembles of Rydberg atoms can be used to achieve strong coupling to optical fields and efficient generation of non-classical states of light. These properties could be exploited for nodes in a future quantum network. Rydberg ensembles also exhibit several interesting many-body physics phenomena, such as Rydberg blockade [13]. This thesis, which has presented results on light-matter interaction in Rydberg atoms, studied two topics: interference effects between non-classical states of light and a coherent state, and investigations on long-lived coherence between ground and Rydberg levels.

We demonstrated the creation of non-classical states from a Rydberg ensemble. We then studied the second-order correlations with an incident coherent field and observed the presence of Hanbury Brown-Twiss (HBT) interference between the coherent field and the emission from a driven superatom. In our experimental setup, stimulated emission could be ignored so our observation of HBT interference contrasts with previous experiments that

have inferred a connection between HBT interference and stimulated emission. These results could lead to a range of future experiments. For example, if the probe pulse is replaced with another single-photon source, we will be able to observe the Hong-Ou-Mandel (HOM) effect [99]. HOM creates an entangled photonic state, $(|2\rangle|0\rangle + |0\rangle|2\rangle)$, an example of a NOON state [100]. A Rydberg ensemble is an excellent source of single-photons making it a good candidate for efficiently creating these entangled states of light. Another potential direction for future work stems from the fact that our experiment was performed in the weak coupling limit. This is where the cross-sectional area of the probe pulse (A) is much greater than the square of the wavelength ($A \gg \lambda^2$); in this regime stimulated emission can be ignored. By focusing the excitation beam near the diffraction limit, it may be possible to study stimulated emission outside of the weak coupling limit on the single excitation level.

We achieved ground-Rydberg coherence times in excess of 20 μs using a state-insensitive optical lattice. This coherence time is an order of magnitude improvement over experiments with unconfined ensembles. One path for future research is using long-lived ground-Rydberg coherence to improve collective qubits employing Rydberg ensembles. As stated in Divincenzo's third criteria for a universal quantum computer, coherence times must be much longer than gate operations [18]. Quantum coherence is also crucial for many other phenomena in quantum optics including photon bunching/antibunching [62], many-body Rabi oscillations [14], and entanglement of multiple qubits [60].

Using the long ground-Rydberg coherence time in a state insensitive optical lattice, we measured the differential nuclear-spin-dependent light shifts for principal quantum numbers n, ranging from $n = 30$ to $n = 65$. This experiment should be relevant for high-fidelity Rydberg qubits and gates. Also, outside of the world of quantum information, the ability to measure the beat frequency between two nuclear sublevels could be used to measure other frequency splittings, such as the remaining hyperfine splittings of Rb or Cs.

These experiments show the potential of Rydberg ensembles for practical applications in the field of quantum information as well as for improving our understanding of the

fundamental physical processes underpinning modern quantum optics.

Bibliography

[1] Max Planck, "On the distribution law of energy in the normal spectrum," *Annalen der Physik*, vol. 4, p. 553 ff (1901).

[2] H. Lyons, "The Atomic Clock," *Instruments*, 22, 133–135 (1949).

[3] J. Aasi, et. al., "Enhanced sensitivity of the LIGO gravitational wave detector by using squeezed states of light," *Nature Photonics* **7**, 790 (2013).

[4] J. Hofmann, M. Krug, N. Ortegel, L. Gérard, M. Weber, W. Rosenfeld, H. Weinfurter, "Heralded Entanglement Between Widely Separated," *Science*, 72-75, (2012).

[5] A. Ashkin, "Acceleration and Trapping of Particles by Radiation Pressure," *Phys. Rev. Lett.* 24 (4): 156–159 (1970).

[6] M. H. Anderson, J. R. Ensher, M. R. Matthews, C. E. Wieman, E. A. Cornell, "Observation of bose-einstein condensation in a dilute atomic vapor," *Science* 269, 198 (1995).

[7] R. P. Feynman, "Simulating Physics with Computers," *International Journal of Theoretical Physics*, VoL 21, 467-788 (1982).

[8] C. Monroe, D. M. Meekhof, B. E. King, W. M. Itano, D. J. Wineland, "Demonstration of a Fundamental Quantum Logic Gate," *Phys. Rev. Lett.*, VoL 75, 4714–4717 (1995).

[9] I. L. Chuang, N. Gershenfeld, and M. Kubinec, "Experimental Implementation of Fast Quantum Searching," *Phys. Rev. Lett.*, VoL 80, 3408–3411 (1998).

[10] B. P. Lanyon, J. D. Whitfield, G. G. Gillett, M. E. Goggin, M. P. Almeida, I. Kassal, J. D. Biamonte, M. Mohseni, B. J. Powell, M. Barbieri, A. Aspuru-Guzik A. G. White, "Towards quantum chemistry on a quantum computer," *Nature Chemistry*, **2**, 106–111 (2010).

[11] F. Arute, *et al.*, "Quantum supremacy using a programmable superconducting processor," *Nature*, **574**, 505–510 (2019).

[12] M. Saffman, T. G. Walker, and K. Mølmer, "Quantum information with Rydberg atoms," *Rev. Mod. Phys.* **82**, 2313 (2010).

[13] Y. O. Dudin and A. Kuzmich, "Strongly interacting Rydberg excitations of a cold atomic gas," *Science* **336**, 887-889 (2012).

[14] Y. O. Dudin, L. Li, F. Bariani, A. Kuzmich, "Observation of coherent many-body Rabi oscillations," *Nature Phys.* **8**, 790 (2012).

[15] C. H. Bennett, G. Brassard, C. Crépeau, R. Jozsa, A. Peres, and W. K. Wootters, "Teleporting an unknown quantum state via dual classical and Einstein-Podolsky-Rosen channels," *Phys. Rev. Lett.*, Vol. 70, pp.1895–1899 (1993).

[16] J. Pan, D. Bouwmeester, H. Weinfurter, A. Zeilinger, "Experimental Entanglement Swapping: Entangling Photons That Never Interacted," *Phys. Rev. Lett.*, Vol. 80, pp.3891–3894 (1998).

[17] C. Bennett, G. Brassard, "Quantum cryptography: Public key distribution and coin tossing." *Theor. Comput. Sci.* 560. 175-179. (1984).

[18] D. P DiVincenzo. "The Physical Implementation of Quantum Computation". arXiv: 0002077, (2000)

[19] L. Li, A. Kuzmich, "Quantum memory with strong and controllable Rydberg-level interactions." *Nat Commun* **7**, 13618 (2016) doi:10.1038/ncomms13618

[20] A. Radnaev, Y. Dudin, R. Zhao, H. Jen, S. Jenkins, A. Kuzmich, T. Kennedy, "A quantum memory with telecom-wavelength conversion" *Nature Phys* **6**, 894–899 (2010) doi:10.1038/nphys1773

[21] D. Barredo, S. De Léséleuc, V. Lienhard, T. Lahaye, A. Browaeys, "An atom-by-atom assembler of defect-free arbitrary two-dimensional atomic arrays", *Science* 1021-1023 (2016)

[22] M. Endres, et. al, "Atom-by-atom assembly of defect-free one-dimensional cold atom arrays," *Science*, 1024-1027 (2016)

[23] T. Graham, M. Kwon, B. Grinkemeyer, Z. Marra, X. Jiang, M. Lichtman, Y. Sun, M. Ebert, M. Saffman, "Rydberg mediated entanglement in a two-dimensional neutral atom qubit array," ArXiv ID 1908.06103v1 (2019).

[24] H. Levine, A. Keesling, G. Semeghini, A. Omran, T. Wang, S. Ebadi, H. Bernien, M. Greiner, V. Vuletić, H. Pichler, M. Lukin, "Parallel implementation of high-fidelity multi-qubit gates with neutral atoms," ArXiv ID 1908.06101v2 (2019).

[25] D. Jaksch, J. I. Cirac, P. Zoller, S. L. Rolston, R. Côté, and M. D. Lukin, "Fast Quantum Gates for Neutral Atoms," *Phys. Rev. Lett.*, Vol.85, 2208 (2000).

[26] M. D. Lukin, M. Fleischhauer, R. Cote, L. M. Duan, D. Jaksch, J. I. Cirac, and P. Zoller, "Dipole Blockade and Quantum Information Processing in Mesoscopic Atomic Ensembles," *Phys. Rev. Lett.*, Vol.87, 037901 (2001).

[27] T. A. Johnson, E. Urban, T. Henage, L. Isenhower, D. D. Yavuz, T. G. Walker, and M. Saffman, "Rabi Oscillations between Ground and Rydberg States with Dipole-Dipole Atomic Interactions", *Phys. Rev. Lett.*, Vol.100, 113003 (2008).

[28] R. H. Dicke, "Coherence in spontaneous radiation processes," *Phys. Rev.* **93**, 99 (1954).

[29] M. S. Safronova, C. J. Williams, and C. W. Clark, "Optimizing the fast Rydberg quantum gate," *Phys. Rev. A* **67**, 040303 (2003).

[30] M. Saffman and T. G. Walker, "Analysis of a quantum logic device based on dipole-dipole interactions of optically trapped Rydberg atoms," *Phys. Rev. A* **72**, 022347 (2005).

[31] R. Hanbury Brown, R. Q. Twiss, "A Test of a New Type of Stellar Interferometer on Sirius," *Nature* **178**, 1046-1048 (1956).

[32] P. R. Berman and V. S. Malinovsky, *Principles of Laser Spectroscopy and Quantum Optics* (Princeton University Press, Princeton 2011).

[33] SAES Getters S.p.A., Viale Italia 77, 20020 Lainate (Milan) - Italy, www.saesgetters.com

[34] IDEX Health & Science, LLC, Center of Excellence, 1180 John Street, Rochester, New York 14586, www.semrock.com

[35] 520 South Main St., Suite 2423, Akron, Ohio, 44311, United States, www.perkinelmer.com

[36] D. Thompson and R. Scholten. "Narrow linewidth tunable external cavitydiode laser using wide bandwidth filter." *Review of Scientific Instruments*, **83** (2012)

[37] EOSPACE Inc, 6222 185th AVE NE, Suite 100, Redmond, WA 98052, https://www.eospace.com

[38] Stable Laser Systems, 4946 63rd Street, Suite B, Boulder, CO 80301, http://www.stablelasers.com

[39] R. W. P. Drever, J. L. Hall, F. V. Kowalski, J. Hough, G. M. Ford, A. J. Munley, H. Ward, "Laser phase and frequency stabilization using an optical resonator." *Applied Physics B.* **31** 97–105, (1983)

[40] TOPTICA Photonics Inc., 5847 County Road 41, Farmington, NY 14425, U.S.A., https://www.toptica.com

[41] HighFinesse GmbH, Wöhrdstraße 4, 72072 Tübingen, Germany, https://www.highfinesse.com/en/

[42] Windfreak Technologies, LLC, New Port Richey, Florida 34652, USA,https://windfreaktech.com/

[43] FAST ComTec Communication Technology GmbH, Grünwalder Weg 28A, 82041 Oberhaching, Germany, www.fastcomtec.com

[44] Andor Technology Ltd., 7 Millennium Way, Springvale Business Park, Belfast BT12 7AL, UK, https://andor.oxinst.com

[45] M Squared, 1 Kelvin Campus, West of Scotland Science Park, Glasgow G20 0SP, UK, http://www.m2lasers.com

[46] J. Lampen, A. Duspayev, H. Nguyen, H. Tamura, P. R. Berman, and A. Kuzmich, "Hanbury Brown–Twiss Correlations for a Driven Superatom," *Phys. Rev. Lett.* **123**, 203603 (2019)

[47] A. Einstein, "The quantum theory of radiation," *Phys. Zs.* **18**, 121 (1917).

[48] A. Lamas-Linares, J. C. Howell, and D. Bouwmeester, "Stimulated emission of polarization-entangled photons," *Nature* **412**, 887–890 (2001).

[49] A. Lamas-Linares, C. Simon, J. C. Howell, and D. Bouwmeester, "Experimental quantum cloning of single photons," *Science* **296**, 712 (2002).

[50] F. W. Sun, B. H. Liu, Y. X Gong, Y. F. Huang, Z.-Y. Ou, and G. C. Guo, "Stimulated emission as a result of multiphoton interference," *Phys. Rev. Lett.* **99**, 043601 (2007).

[51] S. Dong, X. Yao, W. Zhang, S. Chen, W. Zhang, L. You, Z. Wang, and Y. F. Huang, "True single-photon stimulated four-wave mixing," *ACS Photonics* **4**, 746 (2017).

[52] Z. Y. Ou, L. J. Wang, and L. Mandel, "Photon amplification by parametric down-conversion," *J. Opt. Soc. Am. B* **7**, 211 (1990).

[53] Z. Y.-Ou, *Multi-Photon Quantum Interference*, (Springer-Verlag, 2007).

[54] P. R. Berman and A. Kuzmich, "Coincidence counts and stimulated emission resulting from weak pulsed field - atomic interactions," *Phys. Rev. A*, submitted (2019).

[55] M.-L. Shih and P. W. Milonni, "Stimulated emission, absorption, and interference," *Am. J. Phys.* **50**, 1016 (1982).

[56] T. F. Gallagher, *Rydberg atoms* (Cambridge University Press, Cambridge 1994).

[57] E. Urban *et al.* "Observation of Rydberg blockade between two atoms," *Nature Phys.* **5**, 110 (2009).

[58] A. Gaëtan *et al.* "Observation of collective excitation of two individual atoms in the Rydberg blockade regime," *Nature Phys.* **5**, 115 (2009).

[59] M. Ebert *et al.* "Atomic Fock state preparation using Rydberg blockade," *Phys. Rev. Lett.* **112**, 043602 (2014).

[60] D. Barredo *et al.* "Demonstration of a strong Rydberg blockade in three-atom systems with anisotropic interactions," *Phys. Rev. Lett.* **112**, 183002 (2014).

[61] J. Zeiher *et al.* Microscopic characterization of scalable coherent Rydberg superatoms, *Phys. Rev. X* **5**, 031015 (2015).

[62] D. Maxwell, *et al.* "Storage and control of optical photons using Rydberg polaritons," *Phys. Rev. Lett.* **110**, 103001 (2013).

[63] L. Li, Y. O. Dudin, and A. Kuzmich, "Entanglement between light and an optical atomic excitation," *Nature* **498**, 466 (2013).

[64] J. Lampen, H. Nguyen, L. Li, P. R. Berman, and A. Kuzmich, "Long-lived coherence between ground and Rydberg levels in a magic wavelength lattice," *Phys. Rev. A* **98**, 033411 (2018).

[65] M. D. Lukin *et al.*, "Dipole Blockade and Quantum Information Processing in Mesoscopic Atomic Ensembles," *Phys. Rev. Lett.* **87**, 037901 (2001).

[66] M. Saffman, and T. G. Walker, "Creating single-atom and single-photon sources from entangled atomic ensembles," *Phys. Rev. A* **66**, 065403 (2002).

[67] P Komar *et al.*, "Quantum Network of Atom Clocks: A Possible Implementation with Neutral Atoms," *Phys. Rev. Lett.* **117**, 060506 (2016).

[68] B. Zhao, M. Müller, K. Hammerer, and P. Zoller, "Efficient quantum repeater based on deterministic Rydberg gates," *Phys. Rev. A* **81**, 052329 (2010).

[69] E. Brion, F. Carlier, V. M. Akulin, and K. Mølmer, "Quantum repeater with Rydberg-blocked atomic ensembles in fiber-coupled cavities," *Phys. Rev. A* **85**, 042324 (2012).

[70] Y. Han, *et al.*, "Quantum repeaters based on Rydberg-blockade-coupled atomic ensembles," *Phys. Rev. A* **81**, 052311 (2010).

[71] T. Peyronel *et al.*, "Quantum nonlinear optics with single photons enabled by strongly interacting atoms," *Nature* **488**, 57 (2012).

[72] O. Firstenberg, *et al.*, "Attractive Photons in a Quantum Nonlinear Medium," *Nature* **502**, 71-75 (2013).

[73] S. Baur, D. Tiarks, G. Rempe, S. Durr, "Single-Photon Switch Based on Rydberg Blockade," *Phys. Rev. Lett.* **112**, 073901 (2014).

[74] D. Tiarks,*et al.*, "Single-Photon Transistor Using a Förster Resonance," *Phys. Rev. Lett.* **113**, 053602 (2014).

[75] H. Gorniaczyk *et al.*, "Single-Photon Transistor Mediated by Interstate Rydberg Interactions," *Phys. Rev. Lett.* **113**, 053601 (2014).

[76] Y. Y. Jau *et al.*, "Entangling atomic spins with a Rydberg-dressed spin-flip blockade," *Nature Phys.* **12**, 71 (2016).

[77] J. Zeiher *et al.*, "Many-body interferometry of a Rydberg-dressed spin lattice," *Nature Phys.* **12**, 1095 (2016).

[78] H. Bernien *et al.*, "Probing many-body dynamics on a 51-atom quantum simulator," *Nature* **551**, 579 (2017).

[79] E. A. Goldschmidt *et al.*, "Magic wavelengths for the 5s-18s transition in rubidium," *Phys. Rev. A* **91**, 032518 (2015).

[80] T. Topcu, A. Derevianko, "Intensity landscape and the possibility of magic trapping of alkali-metal Rydberg atoms in infrared optical lattices," *Phys. Rev. A* **88**, 043407 (2013).

[81] N. Šibalič *et al.*, "ARC: An open-source library for calculating properties of alkali Rydberg atoms," *Comput. Phys. Comm.* **220**, 319 (2017).

[82] See, for example, S. Wu, P. S. Striehl, M. G. Prentiss, "A Weyl function approach to matter-wave coherence and Talbot-Lau effects," arXiv:0710.5479v2 [physics.atom-ph] (2007); R. H. Leonard and C. A. Sackett, "Effect of trap anharmonicity on a free-oscillation atom interferometer," *Phys. Rev.A* **86**, 043613 (2012).

[83] R. Zhao *et al.*, "Long-lived quantum memory," *Nat. Phys.* **5**, 100 (2009).

[84] S. D. Jenkins, T. Zhang, T. A. B. Kennedy, "Motional dephasing of atomic clock spin waves in an optical lattice," *J. Phys. B* **45**, 124005 (2012)

[85] T. Topcu, A. Derevianko, "Dynamic polarizability of Rydberg atoms: Applicability of the near-free-electron approximation," gauge invariance, and the Dirac sea, *Phys. Rev. A* **88**, 042510 (2013).

[86] H. Nguyen, J. Lampen, P. R. Berman, and A. Kuzmich, "Differential nuclear-spin-dependent light shifts and state mixing of Rydberg atoms," *Phys. Rev. A* **100**, 033412 (2019).

[87] A. Zhang, F. Robicheaux, M. Saffman, "Magic-wavelength optical traps for Rydberg atoms," *Phys. Rev. A* **84**, 043408 (2011).

[88] T. Topcu, A. Derevianko, "Intensity landscape and the possibility of magic trapping of alkali Rydberg atoms in infrared optical lattices," *Phys. Rev. A* **89**, 023411 (2014).

[89] A. Tauschinsky, R. Newell, H. B. van Linden, H. van den Heuvell, and R. J. C. Spreeuw, "Measurement of ^{87}Rb Rydberg-state hyperfine splitting in a room-temperature vapor cell," *Phys. Rev. A* **87**, 042522 (2013).

[90] J. B. Naber, A. Tauschinsky, H. B. van Linden, H. van den Heuvell, and R. J. C. Spreeuw, "Electromagnetically induced transparency with Rydberg atoms across the Breit-Rabi regime," *Scipost. Phys.* **2**, 015 (2017).

[91] H. Sassmannshausen, F. Merkt, and J. Deiglmayr, "High-resolution spectroscopy of Rydberg states in an ultracold cesium gas." *Phys. Rev. A* **87**, 032519 (2013).

[92] D. A. Steck, 2 (2010), http://steck.us/alkalidata

[93] P. R. Berman, H. Nguyen, and A. Kuzmich, "Theory of coherent optical transients with quantized atomic motion," *Phys. Rev. A* **99**, 013427 (2019)

[94] B. Dubetsky, and P. R. Berman, "$\lambda/4$, $\lambda/8$, and higher order atom gratings via Raman transitions," *Laser Physics*, Vol. 12, No. 8, (2002)

[95] A. Corney, *Atomic and Laser Spectroscopy*, Oxford University Press, Oxford, (1977).

[96] W. Li, I. Mourachko, M. W. Noel, and T. F. Gallagher, "Millimeter-wave spectroscopy of cold Rb Rydberg atoms in a magneto-optical trap: Quantum defects of the ns, np, and nd series," *Phys. Rev. A* **67**, 052502 (2003).

[97] D. Meschede, "Centimeter-wave spectroscopy of highly excited rubidium atoms," *J. Opt. Soc. Am. B* **4**, 413 (1987).

[98] See, for example, T. R. Carver, "Mathieu's Functions and Electrons in a Periodic Lattice," Amer. J. Phys. **39**, 1225 (1971); K. Ochs, "A comprehensive analytical solution of the nonlinear pendulum", *Eur. J. Phys.* **32**, 479 (2011).

[99] C. K. Hong, Z. Y. Ou, L. Mandel, "Measurement of subpicosecond time intervals between two photons by interference." *Phys. Rev. Lett.*, **59** (18): 2044–2046, (1987).

[100] J. Pan, Z. Chen, C. Lu, H. Weinfurter, A. Zeilinger, M. Żukowski, "Multiphoton entanglement and interferometry," *Rev. Mod. Phys.*, **84**, 777 (2012)